A STUDY OF ELLIPTICAL VIBRATION CUTTING IN ULTRA PRECISION MACHINING

ZHANG XINQUAN

(B. Eng., Harbin Institute of Technology)

A THESIS SUBMITTED

FOR THE DEGREE OF DOCTOR OF PHILOSOPHY

DEPARTMENT OF MECHANICAL ENGINEERING

NATIONAL UNIVERSITY OF SINGAPORE

2012

Acknowledgement

Firstly, I would like to express my deepest and earnest appreciation to my supervisor, **Associate Professor A. Senthil Kumar**, for his continuous strong support, untiring efforts, excellent supervision and patient guidance. He does not only provide me plenty of knowledge regarding my research, but also share with me his wisdom, insight and life attitude in the past few years. It is really my honor to achieve the guidance from him during my PhD career.

Also, I would like to show my sincere gratitude to my co-supervisor, **Professor Mustafizur Rahman** for his uninterrupted guidance, unwavering support and encouragement throughout my study. He has constantly provided me with valuable assistance and advice to improve both my academic research and daily life.

Special thanks to Dr. Liu Kui and Dr. Nath Chandra from Singapore Institute of Manufacturing Technology for his continuous financial and scholastic support for my research project. I would like to express my deep appreciation to my fiancée, my family, and my friends for their unselfish love, encouragement, and sacrifices throughout my life.

Last but not least, thanks to the staffs of AML: Mr. Nelson Yeo Eng Huat, Mr. Neo Ken Soon, Mr. Tan Choon Huat, Mr. Lim Soon Cheong and Mr. Wong Chian Loong for their time and support in operating the machines and instruments for my experiments. Also thanks to my labmates and friends: Dr. Yu Deping, Dr. Arif, Dr. Asma and Dr. Wang Jingjing for their academic help and inspiration.

Table of Contents

Summary

In the field of precision manufacturing industry, vibration-assisted machining (VAM) has already been demonstrated as a well-known cost-effective method for machining various materials with superior cutting performance compared with conventional cutting (CC) method. As a novel 2D VAM method, elliptical vibration cutting (EVC) has received a lot of attention for its better machining performance especially in machining brittle and hard materials. However, compared to the conventional vibration cutting (CVC) method, very few in-depth experimental and analytical studies have been conducted on transient cutting force, surface generation and tool wear mechanism for the more advanced EVC method.

This study has been carried out in three phases. In the first phase, as cutting force is considered as the most important indicator of machining state and quality, in order to investigate the transient cutting force, a novel method is proposed to realize the low-frequency EVC motion by G-code programming and axis motion control of an ultraprecision machine tool. Based on this method, the transient cutting force in the EVC process is experimentally investigated under different cutting and vibration parameters. Then, an analytical force model is developed for in-depth understanding of the transient cutting mechanics and for accurate prediction of the transient cutting force. In this model, transient thickness of cut and transient shear angle are considered and calculated, and each EVC cycle is divided into three consecutive zones (i.e. CC-like kinetic-friction zone, static-friction zone and reverse kinetic-friction zone) based on the variation of friction modes. Experimental verification is also carried out to justify the validity of the developed cutting force model.

In the second phase, surface generation along nominal cutting direction in EVC is experimentally investigated by conducting a series of grooving tests using a single crystal diamond tool. Then, in order to better understand the surface generation process, a more comprehensive calculation method is developed for determining the theoretical roughness considering the edge radius. The comparison between experimental and predicted roughness shows that the proposed model could predict much more accurate surface roughness than the prevailing model, in which the tool edge radius is not considered.

In the third phase, commercial PCD tools are used to machine hardened stainless steel with the ultrasonic EVC method, and the effects of conventional machining parameters on different output parameters (including cutting force, tool wear, chip formation, and surface roughness) are experimentally investigated. It is found that wear of diamond tools is significantly reduced by applying VAM, and nominal cutting speed has the strongest influence on the tool wear and the surface roughness. Then, an in-depth study is conducted by modeling the cutting energy consumption based on the obtained transient cutting force and measuring the workpiece temperature to find out the reason for the phenomenon. Both the theoretical and experimental results show that the reduced diamond tool wear in VAM of steel is not caused by the reduced heat generation and tool/workpiece temperature which is claimed by previous researchers. Finally, based on investigation and understandings of graphitization mechanism of diamond, two main reasons are suggested to be responsible for the significantly reduced wear rate of diamond tools in VAM of steel: i) contamination of the tool/workpiece interface, and ii) generation of iron oxide.

List of Tables

List of Figures

Abbreviations

AFM	Atomic force microscope
BUE	Built-up edge
CC	Conventional cutting
CNC	Computer numerical control
CVC	Conventional vibration cutting
DOC	Depth of cut
EDS	Energy-dispersive X-ray spectroscopy
EVC	Elliptical vibration cutting
FEM	Finite element method
ID	Inner diameter
MD	Molecular dynamics
OD	Outer diameter
PCD	Polycrystalline diamond
PZT	Piezoelectric Transducer
SCD	Single crystal diamond
SEM	Scanning electron microscope
TOC	Thickness of cut
VAM	Vibration-assisted machining

Nomenclature

Symbol	Unit	Description
a	µm	Tangential amplitude
b	µm	Thrust amplitude
x	m	x-axis coordinate
y	m	y-axis coordinate
t	s	Time
ϕ	deg	Phase shift
ω	rad/s	Angular frequency
v_c	m/min	Nominal cutting speed
R_s	--	Speed ratio
f	Hz	Vibration frequency
γ	deg	Tool rake angle
θ	deg	Transient tool velocity angle
a_p	µm	Nominal uncut chip thickness
t_A	s	Time instant when the tool edge passes point A
t_B	s	Time instant when the tool edge passes point B
t_C	s	Time instant when the tool edge passes point C
t_D	s	Time instant when the tool edge passes point D
t_E	s	Time instant when the tool edge passes point E
t_F	s	Time instant when the tool edge passes point F

t_G	s	Time instant when the tool edge passes point G
t_H	s	Time instant when the tool edge passes point H
t_P	s	Time instant when the tool edge passes point P
$\vec{v}_t$	--	Transient tool velocity vector
$\vec{v}_{ct}$	--	Transient chip velocity vector relative to the tool
$\vec{v}_s$	--	Transient shear velocity vector
TOC_t	µm	Transient thickness of cut
$(TOC_t)_m$	µm	Maximum transient thickness of cut
τ	N/m^2	Shear stress
δ	deg	Constant angle between shear plane and resultant force
R	N	Resultant force
R_{max}	N	Maximum resultant force
t_0	µm	Uncut chip thickness in CC
t_c	µm	Measured chip thickness in CC
w	µm	Width of cut
β_k	deg	Kinetic-friction angle
β_s	deg	Static-friction angle
F_p	N	Principal force along nominal cutting direction
F_t	N	Thrust force perpendicular to nominal cutting direction
F_s	N	Shear force along the shear direction
F_f	N	Friction force along the tool rake face
F_n	N	Normal force perpendicular to the tool rake face
F_{ns}	N	Normal force perpendicular to the shear direction

φ_c	deg	Constant shear angle
φ_{kc}	deg	Shear angle in CC-like kinetic-friction zone
φ_{kr}	deg	Shear angle in reverse kinetic-friction zone
φ_t	deg	Transient shear angle in EVC
φ_s	deg	Transient shear angle in static-friction zone
λ	deg	Tool clearance angle
r_e	μm	Tool edge radius
x_e	m	*x*-axis coordinate of transient surface generation point
y_e	m	*y*-axis coordinate of transient surface generation point
R_{the}	μm	Theoretical roughness considering tool edge radius
R_{th}	μm	Theoretical roughness without considering edge radius
R_{ex}	μm	Experimental roughness
t_{Ae}	s	Time instant when the tool edge passes point A_e
t_{Ce}	s	Time instant when the tool edge passes point C_e
L_c	m	Cutting length
f_r	mm/rev	Feed rate
n_r	rpm	Rotational speed
r	mm	radial distance of tool position from workpiece center
D	mm	Diameter at OD
d	mm	Diameter at ID
$(v_c)_{max}$	m/min	Maximum nominal cutting speed at OD
$(v_c)_{min}$	m/min	Minimum nominal cutting speed at ID

r_n	mm	Tool nose radius
R_{th}^f	μm	Theoretical roughness caused by feed marks in turning
W_{CC}	J	Cutting energy consumption in CC
W_{CVC}	J	Cutting energy consumption in CVC
W_{EVC}	J	Cutting energy consumption in EVC
ΔT_{CC}	^{o}C	Temperature rise in CC
ΔT_{CVC}	^{o}C	Temperature rise in CVC
ΔT_{EVC}	^{o}C	Temperature rise in EVC

Chapter 1: Introduction

This chapter starts with an introduction of the vibration-assisted machining (VAM) method and its wide application. The next section presents a brief review of the elliptical vibration cutting (EVC) method, and the following section provides the motivation, scope and main objectives of this study. Finally, an organizational outline of the whole thesis is presented.

1.1 Vibration-assisted machining (VAM)

The VAM method was first introduced in 1960s and has been progressively applied in the manufacturing industry (Kumabe et al., 1989; Skelton, 1969). Meanwhile, a lot of experimental work for the VAM method has shown that better cutting performance can be achieved in machining various materials compared to the conventional cutting (CC) method. Such superior cutting performance includes smaller cutting force (Zhou et al., 2003), better surface quality (Moriwaki and Shamoto, 1991), longer tool life (Zhou et al., 2006) and suppression of chatter vibration (Xiao et al., 2002), etc. It has also been demonstrated that, by employing the VAM method, diamond tools can be applied to directly machine steel sustainably, which is not realistic by using the CC method due to the chemical affinity between iron and carbon atoms (Casstevens, 1983; Moriwaki and Shamoto, 1991; Paul et al., 1996; Shamoto et al., 1999a). Moreover, the VAM method can save both manufacturing time and cost and in turn improve the productivity compared to other nonconventional machining methods such as electron discharge machining, laser

technology, ELID grinding, electrochemical machining and chemical-mechanical polishing.

Based on the number of vibration modes, two main types of VAM method can be identified: 1D VAM (also named as CVC, i.e. conventional vibration cutting), and 2D VAM (also named as EVC). Nowadays, CVC has been widely studied and is being used in a broad range of machining roles, such as turning , drilling, grinding and milling (Brehl and Dow, 2008). Compared to the CVC method, the EVC method still belongs to the cutting edge technology, which is attracting more and more attention recently because of its even better machining performances.

1.2 Elliptical vibration cutting (EVC)

The EVC (i.e. 2D VAM) method was first introduced in 1993 (Shamoto and Moriwaki, 1993). During machining with the EVC method, the workpiece is fed against the vibrating tool along the nominal cutting direction, and some piezoelectric transducers (PZT) are arranged in a metal block to drive the tool tip to vibrate elliptically in the EVC process. The pulling action applied by the cutting tool can assist to pull chips away from the workpiece and lead to a reversed friction during each cutting cycle (Shamoto and Moriwaki, 1994), and the contacting time between the tool flank face and the workpiece is significantly reduced. Through constant development in almost two decades, this novel method has been proved to be a promising method in terms of almost all cutting performances compared to the CC and CVC methods in cutting various materials, especially difficult-to-cut materials, such as hardened steel (Shamoto and Moriwaki, 1999), glass (Shamoto et al., 1999a), sintered tungsten carbide (Nath et al., 2009a; Suzuki et al., 2004), tungsten alloy (Suzuki et al., 2007a), etc.

Compared to the CVC method, studies on the novel and more advanced EVC method are still relatively superficial, and very few experimental and analytical studies on transient cutting force, surface generation and tool wear mechanism in the EVC process have been conducted.

1.3 Main objectives of this study

This study aims to fulfill the following main objectives:

- To better understand the material removal mechanism in the EVC process, and to accurately predict the transient cutting force, which is tightly correlated to other important output machining aspects such as tool life and surface finish quality.
- To understand the unique surface generation process, and to accurately predict the surface roughness along the nominal cutting direction in the EVC process.
- To investigate the tool wear conditions and find out the inherent reasons for the tool wear suppression in VAM of steel using diamond tools.

In order to achieve the above targets, the following steps have been taken in this study:

- Developing a novel method to generate a low-frequency EVC method to make it feasible to measure the transient cutting force.
- Experimentally investigating the variation of transient cutting force in EVC under different cutting and vibration conditions.
- Developing and verifying an analytical force model considering three important factors: i) the transient thickness of cut (TOC), ii) the transient shear angle, and iii) the transition characteristic of friction reversal.

- Developing and verifying a surface generation calculation method along the nominal cutting direction considering tool edge radius.
- To study the feasibility of polycrystalline diamond (PCD) tools to obtain mirror quality surface on hardened steel for die and mold applications with the ultrasonic EVC method.
- Based on in-depth theoretical and experimental investigation, analyzing and comparing the cutting energy consumptions and workpiece temperatures in CC and VAM, and proposing reasonable reasons for the reduced diamond tool wear in VAM of steel.

1.4 Organization of this dissertation

This dissertation is composed of eight chapters. Chapter 2 first introduces the main principles of CVC and EVC, the benefits of the EVC method and the existing relevant analytical studies. Chapter 3 presents the experimental investigation to study the effects of various machining and vibration parameters on the transient cutting force, in order to understand the fundamental material removal mechanism in the EVC process. In Chapter 4, an analytical force model for the orthogonal EVC process is developed. Then, the predicted force values calculated based on the proposed model are compared with the experimental cutting force values at different cutting and vibration conditions, and relevant issues observed from the results are discussed.

In Chapter 5, an experimental study comprising a series of grooving tests with a single crystal diamond (SCD) tool using the EVC method is firstly presented. Then, an analytical model for the surface generation along the nominal cutting direction is developed. Chapter 6 justifies the feasibility of applying PCD tools, instead of SCD tools, under the EVC method to obtain mirror quality surface on hardened steel for die

and mold applications in near future. Face turning experiments are conducted on hardened steel workpiece under different conventional machining parameters.

In Chapter 7, firstly, cutting energy consumption for VAM is quantitatively modeled and calculated by investigating the transient cutting force and the corresponding tool motion position. Then, the workpiece temperatures are measured in CC and VAM of steel by using a thermocouple, and the obtained results are analyzed and compared. Finally, based on the theoretical and experimental investigation and previous researchers' relevant studies, two main reasons, instead of the reduced temperature claimed by previous researchers, are proposed and discussed to explain the reason for the reduced wear rate of diamond tools in VAM of steel. Chapter 8 concludes the thesis with a summary of main contributions, and future recommendations are also made in this research area.

Chapter 2: Literature review

In this chapter, the main principles of VAM (including CVC and EVC) are first introduced in Section 2.1. Then, Section 2.2 covers the main structure and the development history of the EVC systems. Section 2.3 discusses the benefits of the EVC method in terms of cutting force, surface finish, tool life, and form accuracy. Then, Section 2.4 reviews the analytical studies conducted by previous researchers regarding the EVC process. Finally, concluding remarks are presented in Section 2.5 that leads to the reported study.

2.1 Principle of VAM

2.1.1 Principle of CVC

As mentioned in Section 1.1, the two main types of vibration-assisted machining are CVC (i.e. 1D VAM) and EVC (i.e. 2D VAM). The CVC method started showing up in the late 1950s for assisting traditional metal-cutting (Isaev and Anokhin, 1961; Kumbabe, 1979; Skelton, 1969).

Figure 2.1 shows a schematic view of the CVC process, where the tool vibrates harmonically along the x-axis in a frequency, f, and the workpiece is fed against the tool with a nominal cutting speed of v_c. The points G and H represent the theoretical cutting-start and cutting-end points, respectively, and a_p is the uncut chip thickness. The tool position relative to the workpiece can be given in the following equation:

$$x(t) = a\cos(\omega t) - v_c t \tag{2.1}$$

where a is the vibration amplitude along the x-axis, t is the time, and ω is the angular frequency calculated from f:

$$\omega = 2\pi f \tag{2.2}$$

Therefore, the upfeed increment per cycle can be calculated as v_c/f, which is equal to the distance travelled by the tool in each cutting cycle. The transient tool velocity relative to the workpiece can also be found as the time-derivative of the tool position:

$$x'(t) = -\omega a\sin(\omega t) - v_c \tag{2.3}$$

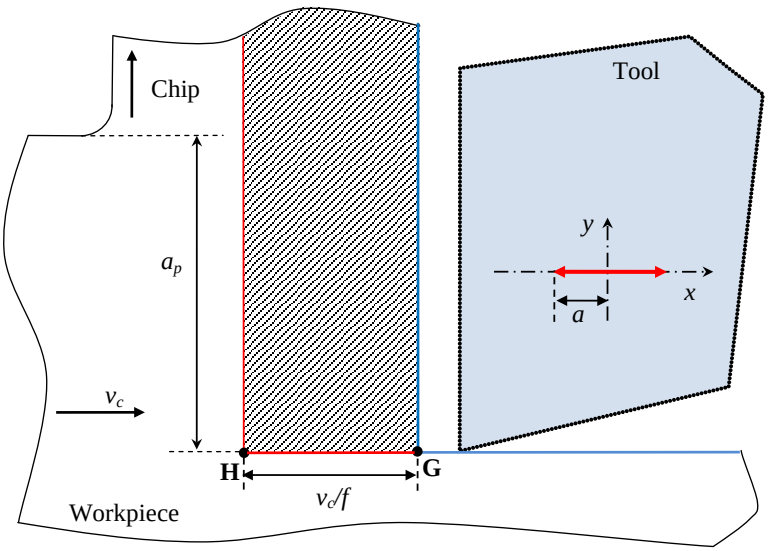

Figure 2.1. Schematic illustration of the CVC process.

The maximum tool vibration speed $(v_t)_{max}$ can be derived as follows:

$$(v_t)_{max} = \omega a \tag{2.4}$$

In fact, $(v_t)_{max}$ also acts as a critical nominal cutting speed, above which the tool rake face never separates from the uncut work material. Speed ratio is considered as one of the most essential parameters in both CVC and EVC methods (Brehl and Dow,

2008; Nath et al., 2011), which is defined as the ratio of the nominal cutting speed to the maximum vibration speed:

$$R_s = v_c / (v_t)_{\max} \tag{2.5}$$

In the CVC process, intermittent cutting occurs when $R_s < 1$:

$$v_c < \omega a \tag{2.6}$$

The intermittent contact between the tool and the chip, indicated in Figure 2.1, can be defined by two time variables: t_G when the tool starts contacting the uncut material and t_H when the tool disengages with it. The values of these two variables can be calculated from the following equations:

$$t_H = \frac{\sin^{-1}(-v_c / \omega a)}{\omega} \tag{2.7}$$

$$a\cos(\omega t_G) - a\cos(\omega t_H) + v_c(t_H - t_G - 1/f) = 0 \tag{2.8}$$

2.1.2 Principle of EVC

EVC adds vertical harmonic motion to the horizontal motion of CVC, and an elliptical vibration locus is generated by the 2D vibration of tool tip during machining process. Figure 2.2(a) and (b) show the 2D and 3D views of the orthogonal EVC process. The orthogonal EVC is defined as a type of EVC process where the vibration modes, the cutting forces and the nominal cutting velocity are all perpendicular to the tool edge (Shamoto et al., 2008). In Figure 2.2, *w* represents the width of cut, a_p represents the nominal uncut chip thickness, and the workpiece is fed along the nominal cutting direction (*x*- axis) against the cutting tool.

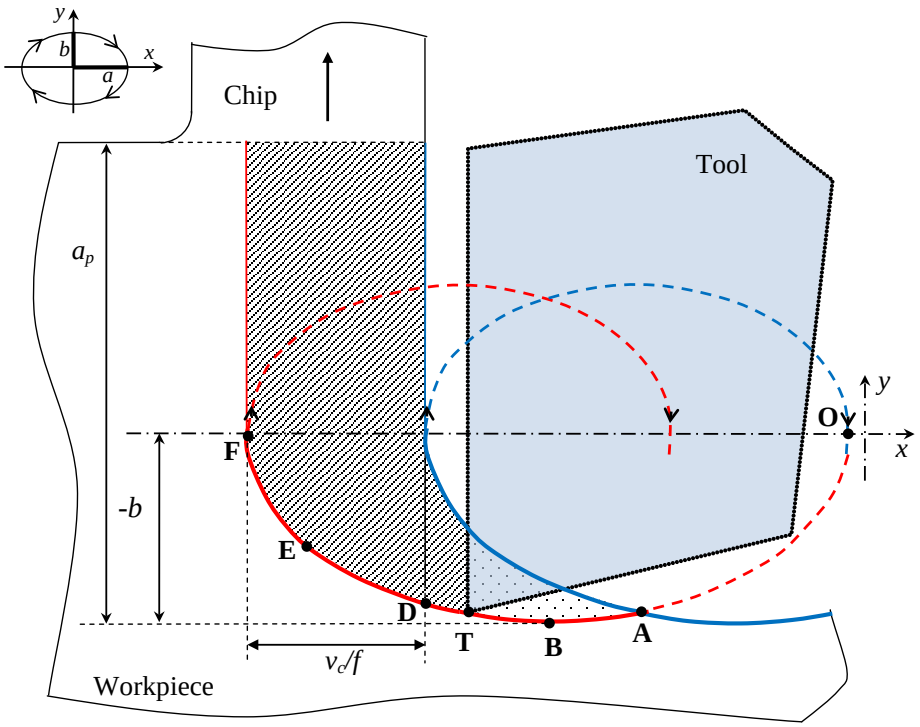

(a)

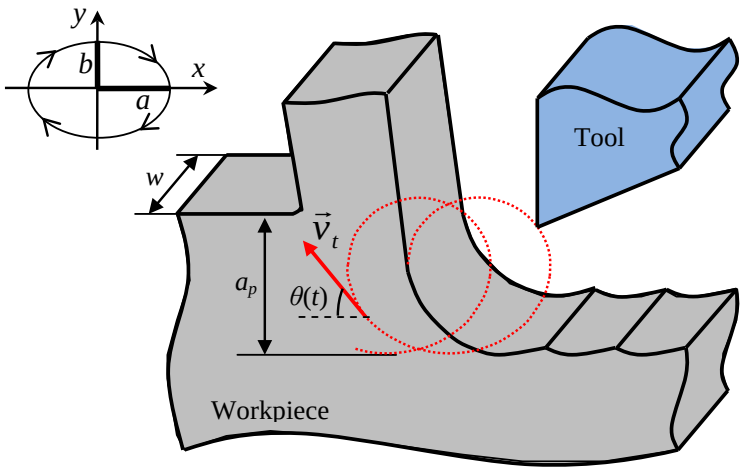

(b)

Figure 2.2. Schematic illustration of the EVC process: (a) 2D view, (b) 3D view.

During each cutting cycle, the tool edge starts cutting at point A on the machined surface left by the previous cycle, reaches bottom point B, passes point D and friction-

reversal point E, and finally ends this cutting cycle at point F. The point D corresponds to the location where the maximum transient thickness of cut (symbolized as $(TOC_t)_m$) is calculated. At point E, the friction between the tool rake face and the chip becomes zero, and thereafter the friction starts reversing in direction. The point T represents the transient contacting point of the tool edge on the workpiece material. The moments when the tool edge passes the points A, B, T, D and F are symbolized as t_A, t_B, t, t_D and t_F, respectively. Relative the workpiece, the transient tool position and velocity in EVC can be given by the following equation sets (Shamoto and Moriwaki, 1994):

$$\begin{cases} x(t) = a\cos(\omega t) - v_c t \\ y(t) = b\cos(\omega t + \phi) \end{cases} \tag{2.9}$$

$$\begin{cases} x'(t) = -\omega a \sin(\omega t) - v_c \\ y'(t) = -\omega b \sin(\omega t + \phi) \end{cases} \tag{2.10}$$

where a and b are the tangential and thrust directional vibration amplitudes, ϕ is the phase shift between the two vibration modes.

If the value of b is set to zero, then Equations (2.9) and (2.10) can be simplified into Equations (2.1) and (2.3), and EVC becomes CVC. Hence, it can be said that CVC is a special form of EVC with no vibration along the thrust direction. For the EVC method, the definitions of maximum vibration speed, and speed ratio are identical to those for the CVC method, as expressed in Equations (2.4) and (2.5). The transient tool velocity angle $\theta(t)$ is defined as the angle of the transient tool velocity vector $\vec{v}_t$ relative to the negative x- axis (see Figure 2.2):

$$\tan\theta(t) = \frac{y'(t)}{-x'(t)}$$

$$\Rightarrow \theta(t) = \tan^{-1}\frac{-b\sin(\omega t + \phi)}{a\sin(\omega t) + v_c} \tag{2.11}$$

It can be seen from Figure 2.2 that the tool approaches the work material with negative velocity angle from point A until it reaches point B, where the tool velocity direction is parallel to the *x*- axis.

In the EVC process, the cutting process becomes intermittent when the minimum relative speed in the direction normal to the rake face is negative (Shamoto et al., 2008):

$$v_c\cos\gamma - \omega\sqrt{(a\cos\gamma - b\sin\gamma\cos\phi)^2 + (b\sin\gamma\sin\phi)^2} < 0$$

$$\Rightarrow v_c < \frac{\omega\sqrt{(a\cos\gamma - b\sin\gamma\cos\phi)^2 + (b\sin\gamma\sin\phi)^2}}{\cos\gamma} \tag{2.12}$$

where γ is the tool rake angle. Under the condition of intermittent cutting, the value of t_F can be obtained as the time when the transient tool velocity is parallel to the tool rake face:

$$\theta(t) + (-\gamma) = 90^o$$

$$\Rightarrow \frac{a\omega\sin(\omega t_F) + v_c}{b\omega\sin(\omega t_F + \phi)} = \tan\gamma \tag{2.13}$$

After separating from the chip at point F, the tool rake face comes back to the same plane at $t_D + 1/f$. Thus, the value of t_D can be obtained by solving the following equation:

$$\frac{x(t_D + 1/f) - x(t_F)}{y(t_D + 1/f) - y(t_F)} = \tan\gamma \tag{2.14}$$

If the rake angle of the cutting tool is zero (i.e. $\gamma = 0$), which is the common case in most EVC tests, Equations (2.12), (2.13) and (2.14) can be simplified into the forms which are similar to Equations (2.6) (2.7) and (2.8).

Figure 2.3 illustrates the theoretical surface generation profile in the EVC process, during which the cusps left on the finished surface perfectly reflect the vibration marks generated by the elliptical vibration locus. The point C represents the cross-over point, and the time when the tool edge passes this point is symbolized as t_C.

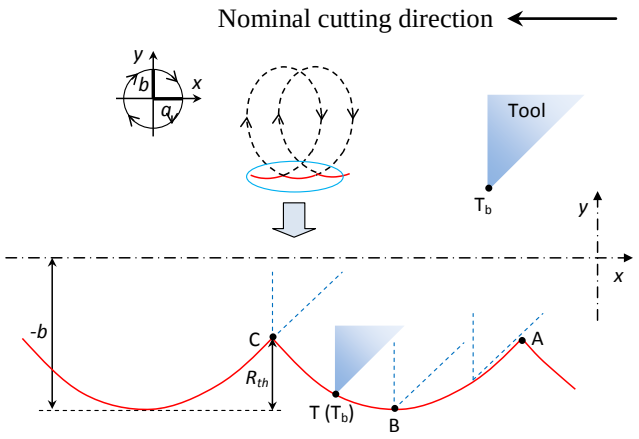

Figure 2.3. Ideal surface generation process in EVC.

According to the geometrical relationship in the EVC process, the values of t_A and t_C can be determined by solving the following equation set (Shamoto and Moriwaki, 1994):

$$\begin{cases} x(t_A) - x(t_C) = 2\pi v_c / \omega \\ y(t_A) - y(t_C) = 0 \end{cases}$$

$$\Rightarrow \begin{cases} a\cos(\omega t_A) - a\cos(\omega t_C) + v_c(t_C - t_A) = 2\pi v_c / \omega \\ b\cos(\omega t_A + \phi) - b\cos(\omega t_C + \phi) = 0 \end{cases} \quad (2.15)$$

The value of t_B can be obtained by solving the following equation:

$$y(t_B) = -b$$

$$\Rightarrow b\cos(\omega t_B + \phi) + b = 0 \quad (2.16)$$

Then, given the vibration parameters (a, b, ω and ϕ) and the nominal cutting speed v_c, the theoretical roughness R_{th} (see Figure 2.3) along the nominal cutting direction without considering the tool edge dimension can be calculated as follows:

$$\begin{aligned} R_{th} &= y(t_A) - y(t_B) \\ &= b\cos(\omega t_A + \phi) + b \end{aligned} \quad (2.17)$$

2.2 EVC systems

Based on the vibration dimension and the mechanical structure, the EVC systems can be classified into two categories (Brehl and Dow, 2008): i) resonant EVC system – the tool supporting structure is made to vibrate at its resonant frequency in two dimensions, and ii) non-resonant EVC system – a mechanical linkage is used to convert the linear expansion and contraction of piezoelectric actuator stacks into an elliptical tool path. In the following part of this section, the resonant and non-resonant EVC systems are reviewed.

2.2.1 Resonant EVC systems

Resonant EVC systems are the most common type of EVC systems, in which piezoelectric actuators are used to create reciprocating harmonic motion of high-frequency (20 kHz or above) elliptical tool motion with low amplitudes (<10 μm). A

cutting tool is attached at the end of the vibrating horn, which is fabricated in a delicate structure to realize desired vibration parameters. Some researchers create the resonant EVC systems by slightly modifying the structure of resonant CVC systems, e.g. changing the mounting position of the cutting tool (Brinksmeier and Glabe, 1999), or mounting the tool on a specially shaped beam, instead of the original horn (Li and Zhang, 2006). However, due to the simplicity and roughness of their design, those EVC systems have limited advantages in terms of cutting performance compared to CVC systems.

In the last decade, Shamoto et al. developed a series of resonant EVC systems (Shamoto et al., 1999a; Suzuki et al., 2007a; Suzuki et al., 2004). Figure 2.4 shows two generations of the ultrasonic resonant EVC systems and their vibration modes. In their first generation of EVC systems, piezoelectric actuators are attached on the side faces of the beam and are activated in opposed pairs to induce bending along the horizontal and vertical directions on the intersecting face (see Figure 2.4(a)). In the second generation, piezoelectric actuators are mounted inside the beam, and vibration along both the longitudinal and the bending directions are generated (see Figure 2.4(b)).

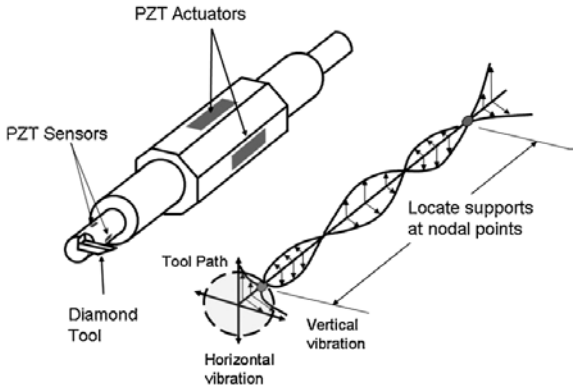

(a)

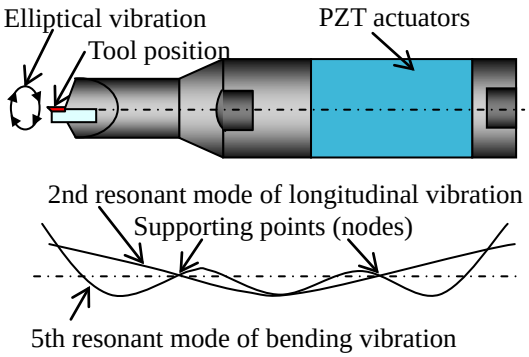

(b)

Figure 2.4. Two generations of ultrasonic resonant EVC systems and their vibration modes: (a) 20 kHz (Shamoto et al., 2002), (b) 40 kHz (Suzuki et al., 2007a).

Later on, by combining the two types of ultrasonic EVC systems, Shamoto et al. developed a new generation of 3D ultrasonic resonant EVC system. Figure 2.5 shows the developed 3D EVC system and its vibration modes simulated by FEM software. In order to reduce the cross talks between the longitudinal mode and the two bending modes, a cross-talk remover was developed based on the conventional cross-talk for the 2D EVC system (Shamoto et al., 2002).

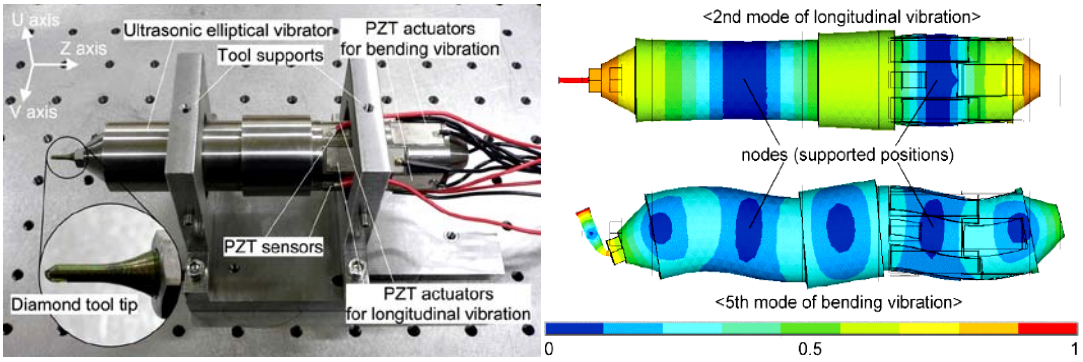

Figure 2.5. 3D ultrasonic resonant EVC system and its vibration modes (Suzuki et al., 2007b).

2.2.2 Non-resonant EVC systems

Compared to resonant EVC systems, non-resonant EVC systems usually have a relatively simpler design and a shorter development cycle, and their vibration parameters (amplitudes, frequency and phase shift) can be adjusted in a larger range. However, they also have a lower vibration frequency and a lower mechanical stiffness. In non-resonant EVC systems, sinusoidal voltage signals are applied to piezoelectric actuators, and the linear motion of the piezo stacks is converted into elliptical tool motion by a mechanical linkage. Shamoto et al. developed the earliest non-resonant EVC system, which has a maximum vibration frequency of 6 Hz (Shamoto and Moriwaki, 1994). Then, Ahn et al. (1999) developed another non-resonant EVC system based on a similar design. Figure 2.6 shows the schematic structure of the system, where piezoelectric actuators are placed at right angles to each other and aligned along the upfeed and vertical directions, and the flexure has an internal cross-shaped cut-out to limit crosstalk between the two motion directions. Later on, in 2001, a new operating design of non-resonant EVC system was developed at North Carolina State University (Brehl and Dow, 2008). Figure 2.7 shows a schematic view of its

operation concept. Advantages of this system are its abilities to operate over a large range of frequencies (200~4000 Hz), tool sizes and varying orientations.

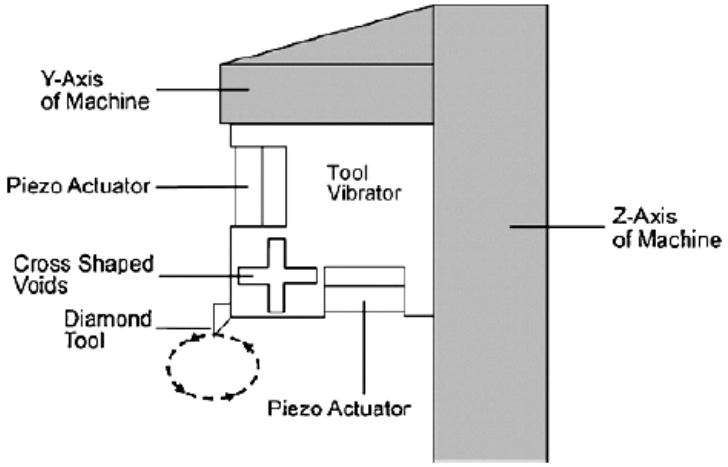

Figure 2.6. Non-resonant EVC system developed at Pusan University (Ahn et al., 1999).

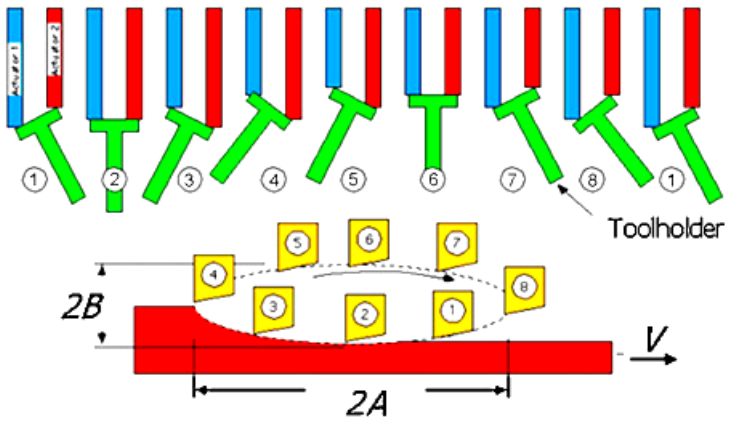

Figure 2.7. Non-resonant EVC system developed at North Carolina State University (Brehl and Dow, 2008).

2.3 Benefits of the EVC method

2.3.1 Smaller cutting force values

Since the CVC method is introduced, researchers have demonstrated that the cutting force values in CVC are smaller than those measured during the CC process for a large range of operation conditions (Astashev and Babitsky, 1998; Babitsky et al., 2004a; Brehl and Dow, 2008; Nath and Rahman, 2008; Weber et al., 1984; Zhou et al., 2003; Zhou et al., 2002). For the EVC method, experimental data shows that it can provide smaller cutting force than the CVC method for the same tool geometry and cutting conditions (Ma et al., 2004; Moriwaki and Shamoto, 1995; Nath et al., 2009c; Shamoto et al., 1999b; Shamoto and Moriwaki, 1994, 1999). The force reduction has been found for a large range of operating parameters and tool-workpiece combinations in both low-frequency and ultrasonic EVC processes.

For low-frequency EVC, it was first observed experimentally in 1994 (Shamoto and Moriwaki, 1994) that the transient cutting forces for machining oxygen free copper are significantly reduced by applying EVC as compared with the CC and CVC methods, as shown in Figure 2.8. From the experimental results, it can be found that long periods of negative cutting forces exist in the EVC cycles. Such negative forces are considered to be caused by the reversed friction force on the tool rake face. Moreover, as the frequency is increased with the other operating parameters unvaried, the peak cutting force decreases accordingly (see Figure 2.8(c) and (d)).

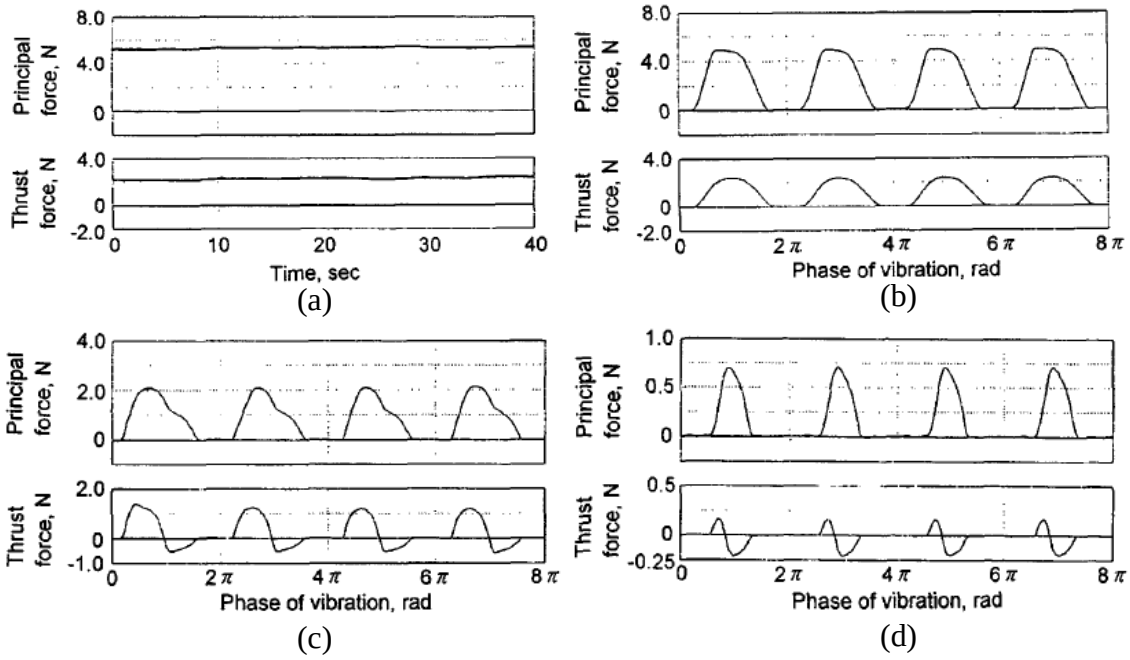

Figure 2.8. Principal and thrust components of the measured cutting force for: (a) CC, (b) CVC , (c) EVC (0.4 Hz), (d) EVC (6 Hz) (Shamoto and Moriwaki, 1994).

Later, after the ultrasonic EVC device was developed by researchers in 1995 (Moriwaki and Shamoto, 1995), similar results for the average cutting force values were also demonstrated experimentally (Ma et al., 2004; Moriwaki and Shamoto, 1995; Shamoto and Moriwaki, 1999; Suzuki et al., 2004). Typical results showing the comparison between CC, ultrasonic CVC and EVC methods are plotted in Figure 2.9(a) and (b). Figure 2.9(a) compares the average cutting forces (principal, thrust and feed) between the ultrasonic CVC and ultrasonic EVC methods as a function of cutting distance for hardened die steel (Shamoto and Moriwaki, 1999). Figure 2.9(b) compares the average thrust forces between all the three cutting methods for machining aluminum workpiece using carbide tools (Ma et al., 2004). It can also be noted from Figure 2.9 that, unlike the low-frequency EVC method, only average

cutting force can be measured by the force dynamometer for the ultrasonic EVC process. It is because the cutting forces need to be transmitted to the piezoelectric force sensor through intermediate elements, including VAM system itself. Such intermediate elements work as a mass-spring-damper system with a relative low natural frequency. Hence, the whole force measurement system acts as a low-pass filter and can only measure the average cutting forces, instead of the high-frequency transient cutting force.

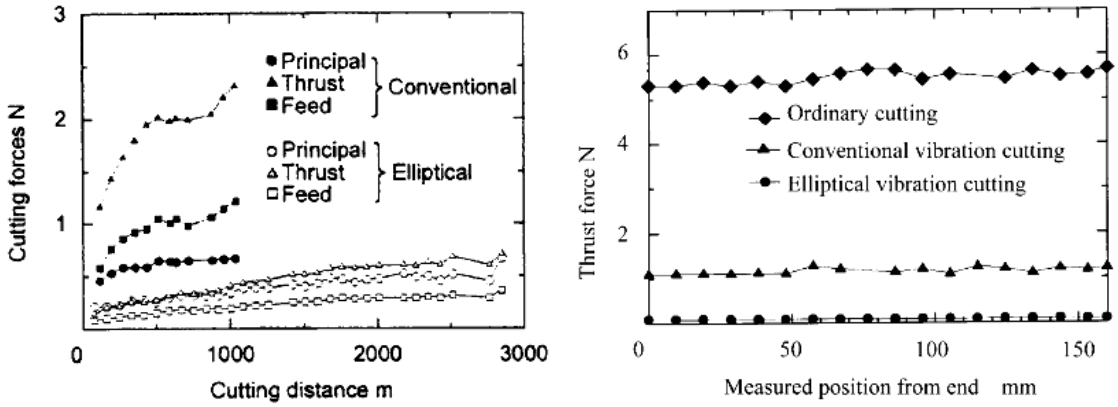

Figure 2.9. Comparison of average cutting forces for: (a) ultrasonic CVC and ultrasonic EVC methods (Shamoto and Moriwaki, 1999), (b) CC ("ordinary cutting"), ultrasonic CVC and ultrasonic EVC methods (Ma et al., 2004).

2.3.2 Improved surface finish

For the CVC method, it has been known that the surface finish is better than that obtained in the CC process for similar cutting conditions (Moriwaki et al., 1991, 1992; Nath et al., 2007, 2008). For the EVC method, the surface finish can be further improved compared with that achieved with the CVC and CC methods, especially in machining difficult-to-cut materials, such as hardened steel and brittle ceramics

(Shamoto et al., 1999a; Shamoto and Moriwaki, 1999; Suzuki et al., 2007a; Suzuki et al., 2004; Suzuki et al., 2003).

In 1999, Shamoto et al. applied ultrasonic EVC in turning of the hardened steel using diamond tools and compared the surface roughness with that obtained with the ultrasonic CVC method. The results plotted in Figure 2.10 show that EVC can provide better and more sustainable surface quality than CVC. Optical quality surfaces with maximum roughness of less than 0.05 μm can be achieved up to a cutting distance of 2250 m with the EVC method, while the roughness obtained by the CVC method increases rapidly at a cutting distance of about 300 m.

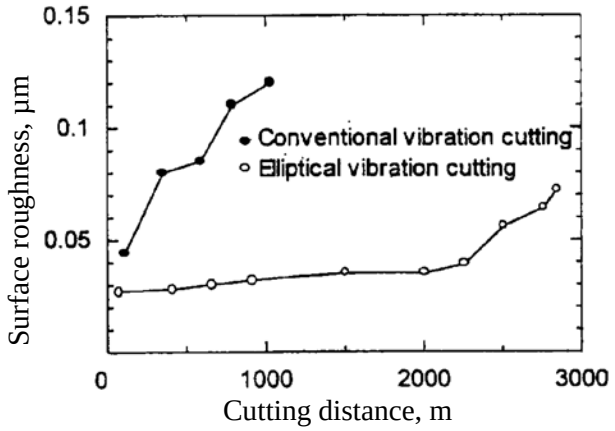

Figure 2.10. Comparison of surface roughness against cutting distance for CVC and EVC (Shamoto et al., 1999a).

In 2005, Suzuki et al. have also applied the EVC method to machine brittle materials, such as sintered tungsten carbide, zirconia ceramics, calcium fluoride and glass. Figure 2.11 shows captured photographs for the finished surfaces of the four brittle materials with the CC and EVC methods. It can be seen that all the comparison results have shown that EVC performs significantly better in achieving better surface quality than CC does. Researchers attribute such superior surface quality to the

capability of EVC in increasing the critical depth of cut (DOC), which is an essential parameter in machining brittle materials. Below the critical DOC, ductile-mode machining can be achieved, and hence the smooth surface quality can be obtained, and vice versa.

CC EVC

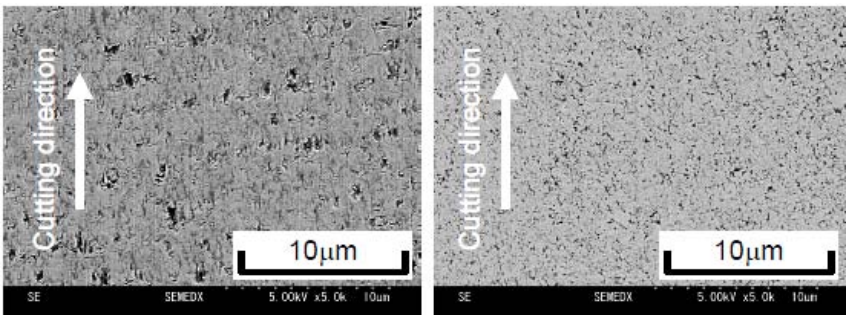

(a)

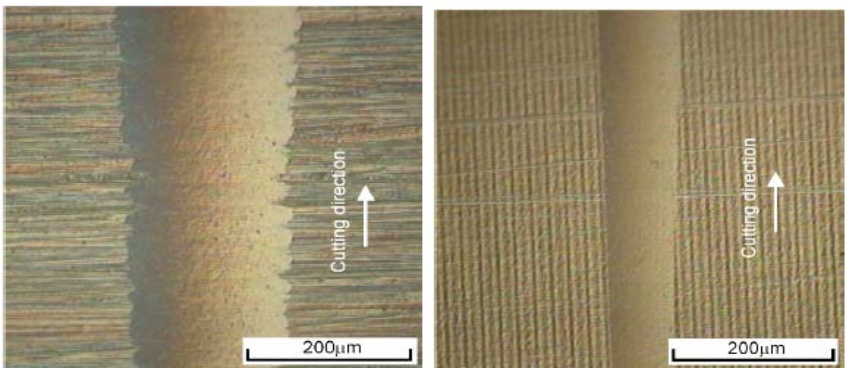

(b)

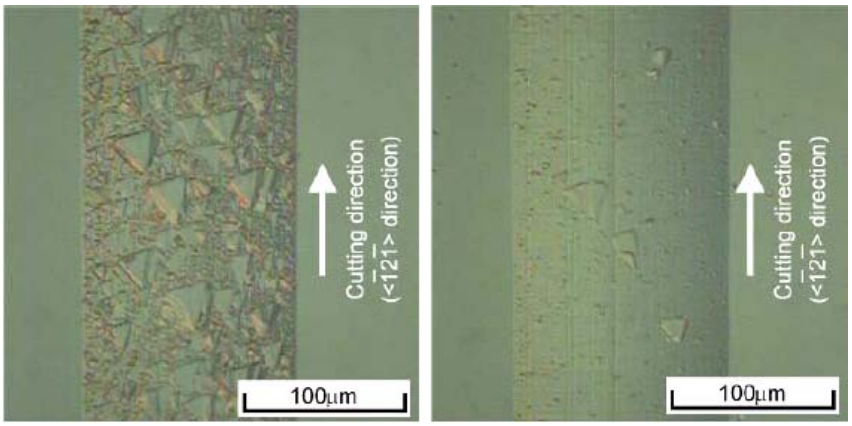

(c)

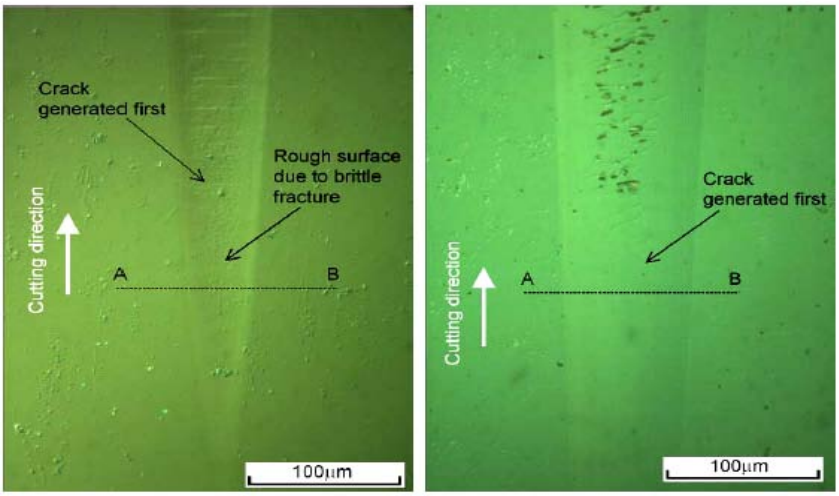

(d)

Figure 2.11. Comparison of the surfaces finished by two cutting methods (CC and EVC) for different brittle materials: (a) sintered tungsten carbide, (b) zirconia ceramics, (c) calcium fluoride, and (d) glass (Suzuki et al., 2004).

2.3.3 Extended tool life

It has already been known that, when cutting ferrous materials with the CC method, chemical wear rather than nonchemical abrasive wear dominates the wear of the cutting tools made of diamond due to the iron-catalyzed graphitization of diamond (Casstevens, 1983; Evans and Bryan, 1991; Ikawa and Tanaka, 1971; Komanduri and Shaw, 1976; Paul et al., 1996; Shimada et al., 2004; Thornton and Wilks, 1978, 1979).

Although it is known that CVC can significantly improve the tool life compared to CC (Nath et al., 2007; Zhou et al., 2003; Zhou et al., 2002), the EVC method can further extend the tool life, especially when machining difficult-to-cut materials, including hardened steel and brittle materials (Nath et al., 2009a, c; Shamoto and Moriwaki, 1999; Suzuki et al., 2007a). By applying the EVC method, Shamoto et al. can extend the tool life of diamond when machining steel by more than seven times compared to the CVC method (see Figure 2.10). Figure 2.12 shows the cutting edges

after machining hardened steel using the CVC and EVC methods. It can be seen that the tool used in CVC is chipped, while the one used in EVC is just slightly worn without chipping.

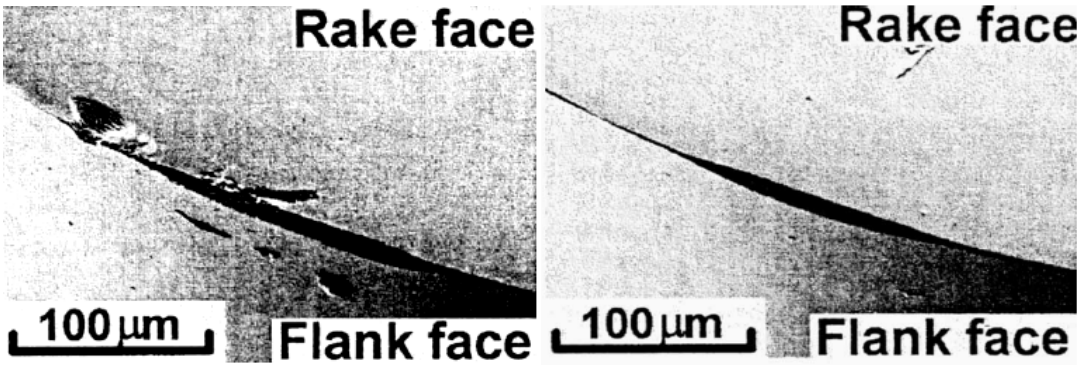

(a) (b)

Figure 2.12. SEM photographs of cutting edges of worn diamond tools: (a) after CVC of steel for 1000m, and (b) after EVC of steel for 2800m (Shamoto and Moriwaki, 1999).

Not only in machining hardened steel with diamond tools, but in machining brittle materials, the EVC method also performs well in extending the tool life. Figure 2.13 shows the comparison results of cutting performance in CC and EVC of sintered tungsten carbide. It can be seen that the flank wear width for CC is larger than that for EVC. Figure 2.14 shows SEM images of the cutting edges used in planing of tungsten alloys with the CC and EVC methods. Considerable rake and flank wear and adhesion of machined material can be observed for the tool used in CC, while there is no tool wear or adhesion for EVC.

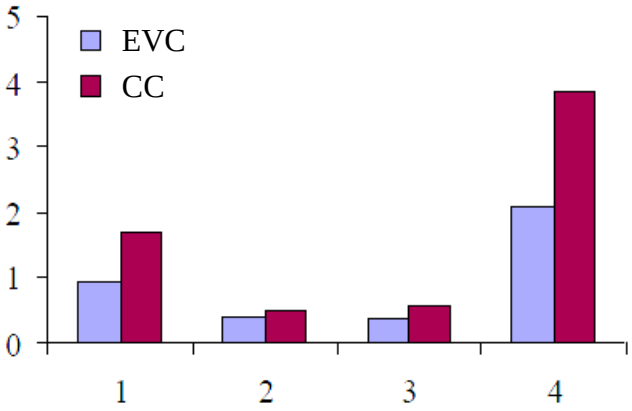

1) Cutting force (N), 2) Flank wear width (μm) x10,
3) R_a (μm) x10, and 4) R_z (μm) x10.

Figure 2.13. Comparison of cutting performance between the CC and EVC methods (Nath et al., 2009c).

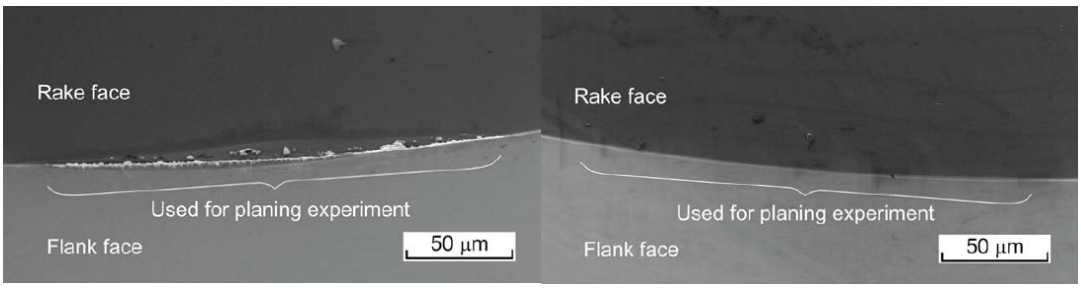

(a) (b)

Figure 2.14. Cutting edges of diamond tools used for planing tungsten alloys with: (a) after CC of 1.08 m, and (b) after EVC of 1.35 m (Suzuki et al., 2007a).

2.3.4 Improved form accuracy and burr suppression

Ma et al. investigated the form accuracy in CC, CVC and EVC and compared the experimental results, as shown in Figure 2.15 (Ma et al., 2004). It can be observed that the shape error is reduced by 79% from 28 μm to 6 μm using the CVC method, while the EVC method can improve the form accuracy by about 98% compared to the

CC method. Furthermore, Ma et al. have also experimentally and theoretically proved that regenerative chatter occurring in ordinary cutting process can be suppressed effectively by adding elliptical vibration on the cutting tool (Ma et al., 2011). The authors attribute this fact to the separating characteristic and the characteristic of reversed frictional direction between the tool rake face and the chip.

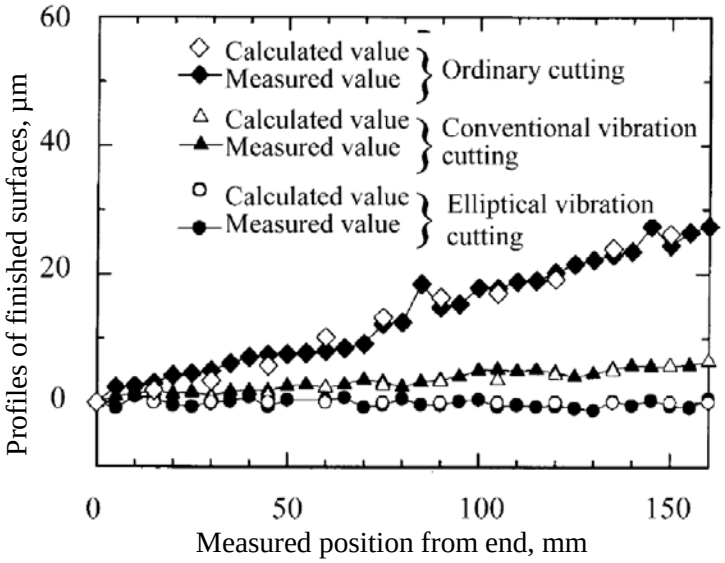

Figure 2.15. Influence of the three cutting methods (CC, CVC and EVC) on the shape error (Ma et al., 2004).

In 2005, Ma et al. have also investigated the suppression of burrs in EVC of aluminum (52S). Figure 2.16 shows heights of the feed-direction burrs measured in the CC, CVC and EVC processes. Compared to CC and CVC, the height of burrs in EVC can be reduced significantly. Such fact is considered to be caused by the reduced average pushing stress and the reduced average bending stress of deformation zone on the workpiece edge in burr formation.

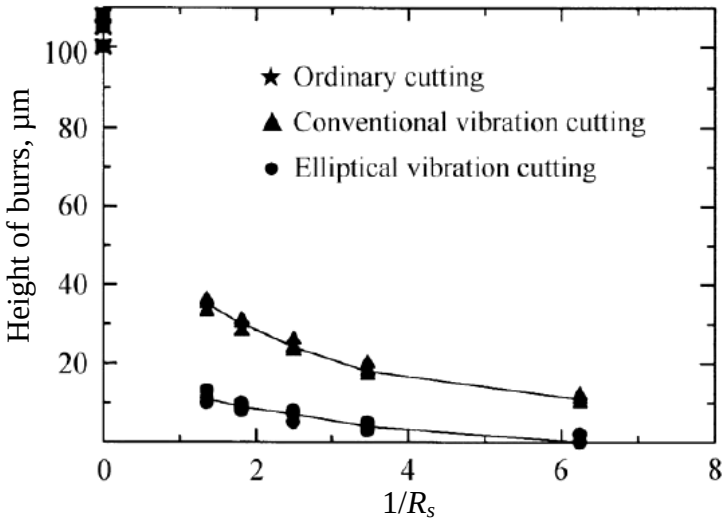

Figure 2.16. Height of burrs for the CC, CVC and EVC methods (Ma et al., 2005).

2.4 Analytical studies of EVC

2.4.1 Force models

In order to investigate the reason for the smaller cutting forces obtained by the EVC method, Shamoto et al. developed the first generation of force model in 1999 (Shamoto et al., 1999b), in which an average friction angle $\overline{\beta}$ defined in the EVC process is calculated based on the kinetic-friction angle β. Then the average shear plane angle ϕ can be obtained by applying the famous maximum shear stress principle (Lee and Shaffer, 1951). However, the transient cutting force in EVC was not predicted by the authors in their study.

Later on, in 2008, Shamoto et al. developed a 3D analytical EVC force model, in which they attributed the thrust force reversal to the friction force reversal on the tool rake face (Shamoto et al., 2008). Moreover, they explained that, during each EVC cycle, the friction force reverses at the position where the speed component of transient tool velocity along the tool rake face exceeds the real chip velocity (point E

in Figure 2.2(a)). The resulted relative velocity between the chip and the tool will change in direction once the transient tool velocity angle exceeds the average shear angle position. Before that position, the friction on the tool rake face is restraining the chip motion, while, after that position, the friction will assist the chip to move upward from the workpiece. Such friction reversal characteristic leads to a significant increment of the average shear angle, which in turn leads to considerable reduction of the cutting force. Figure 2.17(a) shows a sketch of the EVC force model illustrating the average shear angle which can be calculated based on the maximum shear stress principle (Lee and Shaffer, 1951) or the minimum energy principle (Merchant, 1945b). Based on their developed force model, Shamoto et al. compared the simulated results and the experimental data obtained with the EVC method, as plotted in Figure 2.17(b). However, it can be observed that the simulated force roughly agrees with the experimental data, and considerable mismatch still exists between the simulated and experimental results.

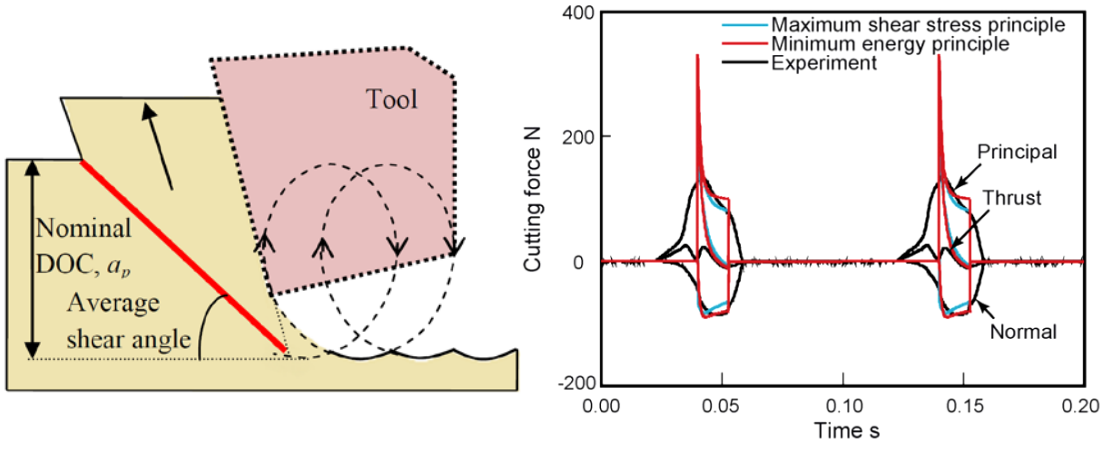

(a) (b)

Figure 2.17. (a) Redrawn sketch of the EVC force model, (b) Simulated and experimental transient cutting forces (Shamoto et al., 2008).

2.4.2 Surface generation and critical speed ratio

Shamoto et al., based on their proposed purely geometrical model for EVC process (Shamoto and Moriwaki, 1994), developed a calculation method for the height of the generated cusps, and also investigated the effects of vibration frequency on the surface generation. The theoretical surface generation profile without considering the tool edge radius is shown in Figure 2.3, where the cusps left on the finished surface perfectly reflect the vibration marks generated by the elliptical vibration locus.

For ductile machining of hard and brittle materials, the DOC should be selected carefully to make its value lower than the critical DOC, which is extremely low (1 μm or less) for common brittle materials such as sintered tungsten carbide, glass and ceramics (Liu et al., 2004; Liu and Li, 2001). In order to maintain the ductile-mode machining in EVC of brittle materials, Nath et al. obtained a critical speed ratio of 0.12837 based on an analytical investigation of the geometrical EVC process (Nath, 2008). Figure 2.18 shows the Nomraski photographs of machined surfaces of sintered tungsten carbide at different speed ratios, which are smaller or larger than the critical speed ratio. It can be seen that, below the critical value of 0.12837, ductile-mode machining of the brittle materials can be obtained, which is considered by Nath et al. to be caused by a reduced maximum thickness of cut under such condition.

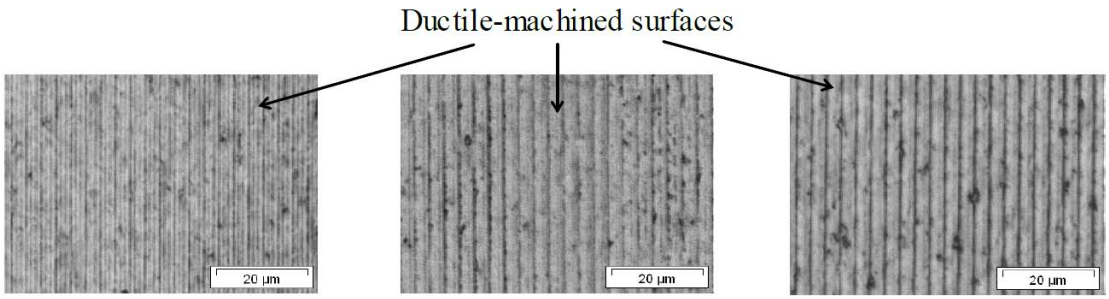

(a)

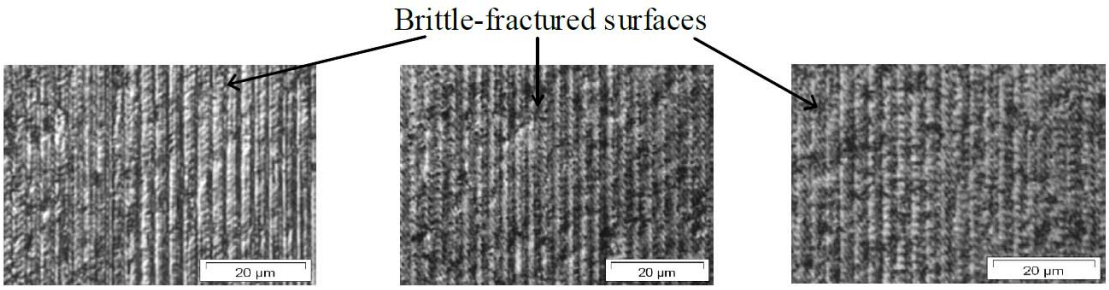

(b)

Figure 2.18. Photographs of the machined surfaces of sintered tungsten carbide for different values of speed ratios: (a) 0.075 (R_s < 0.12837), (b) 0.131 (R_s > 0.12837) (Nath et al., 2011).

2.4.3 FEM and MD analysis

For the CVC process, Babitsky et al. conducted a series of finite element method (FEM) studies on its cutting mechanics and studied the chip deformation and stress distribution in detail (Ahmed et al., 2006, 2007a, b; Babitsky et al., 2004b; Mitrofanov et al., 2005a; Mitrofanov et al., 2004, 2005b). For the EVC process, very few FEM studies have been conducted on its unique cutting mechanism. Amini et al. simulated the EVC process using FEM software and compared the results with those of CC and CVC in their study (Amini et al., 2010). Deformation and stress distribution of the workpiece material and the cutting mechanics are analyzed and discussed for the three cutting methods. Figure 2.19 shows the chip formation and

stress distribution in the EVC process for one cutting cycle. Their simulation results indicate that the initial contacting part in EVC (point A to point D in Figure 2.2(a)) is not formed into a chip but pushed into the workpiece. Such process leads to an extremely high equivalent Von Mises stress at this stage, as shown in Figure 2.19(c). Amini et al. have also compared simulated cutting force values with the experimental ones obtained by Shamoto et al. (1994), and they are found in a good agreement with each other.

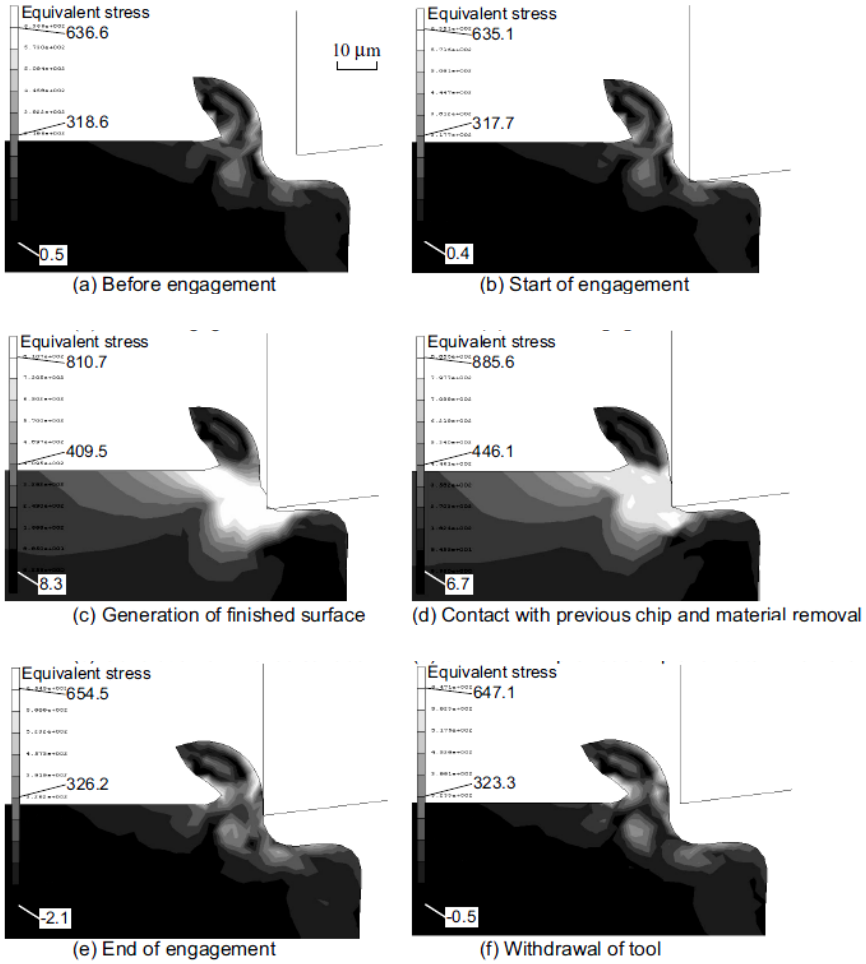

Figure 2.19. Chip formation and stress distribution simulated in one vibration cycle in EVC (Amini et al., 2010).

Liang et al. studied the nano-metric behavior of EVC of single crystal silicon with SCD tools by employing molecular dynamics (MD) analysis (2006). The cutting force and stress distribution in the EVC process have been analyzed. Unfortunately, no experimental studies have been conducted in their study, and the given vibration parameters (amplitudes and frequency) in the simulation are either too small or too large.

2.5 Concluding remarks

As mentioned above, although extensive experimental research has been conducted on the average cutting force in EVC, very few studies have been found on the transient cutting force, which is strongly correlated with the inherent cutting mechanism of the EVC process. Researchers studied the transient cutting force in EVC at different frequencies, and proposed a simple analytical force model for the transient cutting force. However, besides the frequency, the effects of other cutting and vibration conditions on the transient cutting force have not been studied yet. Moreover, the predicted cutting force based on the existing proposed model does not match well with the experimental one, which might be caused by the overlook of some transient characteristics, such as transient thickness of cut, transient shear angle, and the reversal of friction direction.

Shamoto et al. developed a calculation method for the height of the generated vibration cusps along the nominal cutting direction, which will eventually increase the roughness of machined surface and are considered detrimental for achieving high-quality mirror surface. Such drawback of the EVC method may become an important reason which can limit its wider application. However, until now, very little research has been conducted to study the effects of machining parameters on the surface

generation. Moreover, in the proposed calculation model, a critical assumption is that the tool edge is assumed to be perfectly sharp, which may not be reasonable for the situation when the edge radius of non-SCD tools is comparable to the vibration amplitudes.

Although researchers have used SCD tools to machine hardened steel with the EVC method, and observed significantly longer tool life compared to the CC and CVC methods, the application feasibility of inexpensive PCD tools, instead of SCD tools, under the EVC method to obtain mirror quality surface on hardened steel for die and mold applications has not been justified yet. Moreover, the reason claimed by most previous researchers for the reduced diamond tool wear in VAM of steel was found to be ambiguous and not reasonable, and its correctness has not been confirmed experimentally and theoretically.

Chapter 3: Experimental investigation of transient cutting force in EVC

Cutting force is considered as the most important indicator of machining state and quality. Analysis of the cutting force plays an important role in the determination of characteristics of machining performances like tool wear, surface quality, cutting energy, and machining accuracy. As mentioned in Chapter 2, in order to investigate the fundamental cutting mechanics of the EVC process, researchers (Shamoto and Moriwaki, 1994) have studied the transient cutting force at different vibration frequencies, and found that higher vibration frequency can reduce the transient cutting force. However, besides the vibration frequency, the effects of other cutting and vibration conditions (including tangential amplitude, thrust amplitude and speed ratio) on the transient cutting force have not been studied yet.

Speed ratio is considered as one of the most essential parameters in the EVC method (Nath et al., 2011; Shamoto et al., 2008). It was found that the speed ratio has significant effects on cutting performances (e.g. time-averaged cutting force, tool wear and surface roughness). Tangential and thrust amplitudes are two key parameters in vibration-assisted machining technology (Brehl and Dow, 2008). Tangential amplitude is used to discriminate the CVC method from the CC method, and thrust amplitude is used to discriminate the EVC method and the CVC method. For the EVC method, both the tangential and thrust amplitudes are larger than zero, and the tool tip vibrates in two dimension, whereas in the CVC method, the thrust amplitude is equal

to zero, and the tool tip vibrates in only one dimension, while for the CC method, both the tangential and thrust amplitudes are equal to zero, and the tool tip does not vibrate. Unfortunately, the above three essential parameters' effects (speed ratio, tangential and thrust amplitudes) on the transient cutting force in the EVC process have not been studied yet. Therefore, an intensive experimental investigation to study their effects is necessary to enhance the understanding of fundamental material removal mechanism in the EVC process and to explain and predict the cutting performance under various cutting and vibration conditions.

In this chapter, the characteristics of the EVC process are investigated analytically by studying the transient thickness of cut (TOC_t) and the friction reversal process in each EVC cycle. Then, a series of low-frequency orthogonal EVC tests are conducted to study the effects of three essential parameters on the transient cutting force. By analyzing the values of TOC_t and the friction reversal time for each EVC test, results of the transient cutting force at different conditions are interpreted analytically.

3.1 Characteristics of the EVC process

3.1.1 Transient thickness of cut

It is understood the variation of transient TOC (TOC_t) is a key characteristic in the EVC process (Nath et al., 2011). Figure 3.1(a) and (b) show the 2D view of the EVC process before and after the tool edge passes the maximum TOC_t (symbolized as $(TOC_t)_m$) point D, respectively. The value of TOC_t gets continuously varied and is always smaller than the nominal depth of cut a_p due to the overlapping cutting cycles. During each EVC cycle, the tool edge starts cutting from point A on the machined

surface left by the previous cycle, reaches the bottom point B, passes the $(TOC_t)_m$ point D and the friction reversal point E (Shamoto et al., 2008), and finally ends this EVC cycle at the cutting-end point F, as shown in Figure 3.1. The point T represents the instant position of the tool edge, and the point P represents the contact location of the tool rake face on the surface machined by the previous cutting cycle.

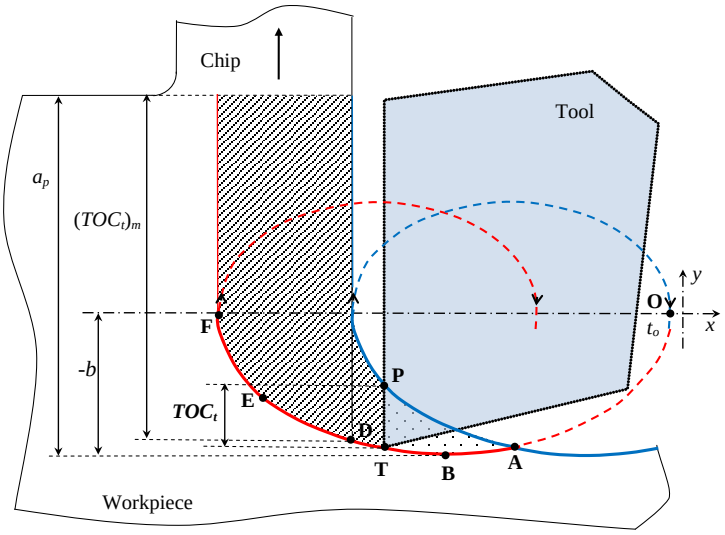

(a)

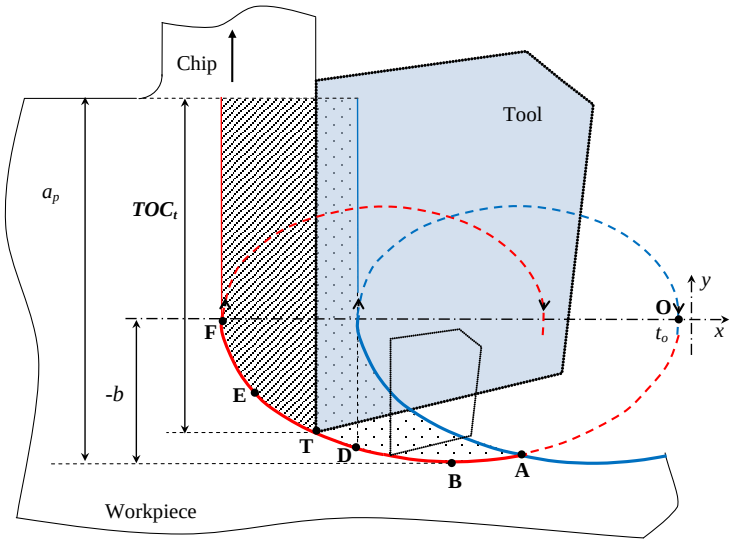

(b)

Figure 3.1. 2D view of the EVC process at different time instants: (a) before the tool edge passes the $(TOC_t)_m$ point, (b) after the tool edge passes the $(TOC_t)_m$ point.

On the one hand, before the instant when the tool edge passes the $(TOC_t)_m$ point D, TOC_t has to be calculated as the height of TP (see Figure 3.1(a)). On the other hand, after that critical instant, TOC_t is calculated along the *y*- axis from the position of the tool edge to the workpiece free surface (see Figure 3.1(b)).

The instant it passes the point P in the previous cutting cycle is designated as t_P. From the geometrical relationships shown in Figure 3.1(a) and (b), TOC_t at different instants in a cutting cycle can be calculated using the following equation:

$$TOC_t = \begin{cases} 0, & t < t_A, t \geq t_F \\ y(t_P) - y(t), & t_A \leq t < t_D \\ a_p - (y(t) + b), & t_D \leq t < t_F \end{cases} \tag{3.1}$$

The values of the time instants t_A, t_D and t_F can be solved according to Equations (2.13), (2.14) and (2.15) in Chapter 2, and the value of t_P can be calculated by applying the Newton-Raphson method on the following equation with a given value of t ($t_A < t < t_D$):

$$\frac{x(t) - x(t_P)}{y(t) - y(t_P)} = \tan\gamma, \quad 0 < (t - t_P) < \frac{2\pi}{\omega} \tag{3.2}$$

For the CC method, the TOC of work material, which is also known as the uncut chip thickness, is constant throughout the cutting process. According to the conventional metal cutting theory (Oxley, 1989), the resultant force can be calculated as follows:

$$R = \frac{\tau w t_0}{\sin\varphi_c \cos\delta} \tag{3.3}$$

where τ is the shear stress, t_0 is the fixed uncut chip thickness in CC process, and φ_c is the constant shear angle, δ is the assumed constant angle between the shear plane

and the resultant force, as shown in Figure 3.2. It can be seen that the value of R is in direct proportion to t_0:

$$R \propto t_0 \tag{3.4}$$

Although the EVC process is different from the CC process in the material removal process, the fundamental cutting mechanism should be the same, and hence the thin shear plane theory will still be applicable to the EVC process. Therefore, keeping the other parameters (e.g. shear angle, shear stress, etc) unvaried, the transient resultant cutting force $R(t)$ applied on the cutting tool should be in direct proportion to the value of TOC_t in the EVC process:

$$R(t) \propto TOC_t \tag{3.5}$$

3.1.2 Friction reversal process in the EVC process

For the CC method, a schematic illustration of the CC process is shown in Figure 3.2, where the symbols, R, F_{ns}, F_n, F_p and F_t represent the resultant force, the normal force perpendicular to the shear direction, the normal force perpendicular to the rake face, the principal force along the nominal cutting direction, and the thrust force perpendicular to the nominal cutting direction, respectively. β_k represents the kinetic-friction angle between the tool rake face and the work material. $\vec{v}_s$, $\vec{v}_t$ and $\vec{v}_{ct}$ represent the transient shear velocity, the transient tool velocity relative to the workpiece, and the transient chip velocity relative to the tool. It can be seen from Figure 3.2 that the tool velocity $\vec{v}_t$ always stays invariant in direction, the shear velocity $\vec{v}_s$ and the chip velocity $\vec{v}_{ct}$ also remain constant in direction. Due to the sliding movement of the chip on the tool rake face throughout the CC process, kinetic friction is induced and tends to push the chip material down toward the workpiece.

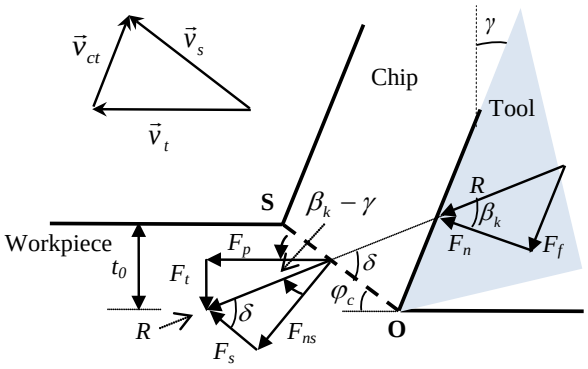

Figure 3.2. Schematic illustration of the CC process.

By analyzing the recorded data of the transient cutting force in the EVC process, researchers have proven the existence of friction force with reversed direction (Shamoto and Moriwaki, 1994). Such friction reversal process is considered to be another essential characteristic of the EVC method, besides the variation of TOC_t. Later on, researchers (Shamoto et al., 2008) proposed that there exists a critical friction reversal point E (see Figure 3.1), at which the friction on the tool rake face is about to reverse in direction, meaning that the friction force is zero at this critical point.

Before the tool edge passes the point E (i.e. $t < t_E$, t_E represents the time when the tool edge passes point E), the tool is pushing the chip downward to the workpiece, which is similar to the CC process (see Figure 3.2). After the tool edge has passed this critical friction reversal point E in the EVC process (i.e. $t > t_E$), the tool will pull the chip upward from the workpiece. Figure 3.3 shows the force and velocity relationships at an instant where the friction is reversed in direction.

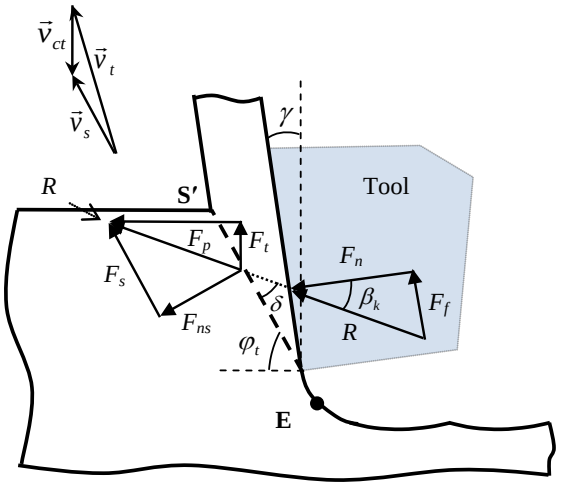

Figure 3.3. Force and velocity relationships after the tool passes the friction reversal point in the EVC process.

In order to clearly analyze the transient friction angle and the transient shear angle, a schematic illustration of the transient friction angle and the induced transient shear angle in an EVC cycle is drawn in Figure 3.4(a) and (b). The negative value of the kinetic-friction angle $-\beta_k$ is used to represent the reversed friction in direction, and the kinetic-friction angle is assumed to be constant throughout the cutting process. The points E_1 and E_2 in Figure 3.4 represent two friction reversal points, and t_{E1} and t_{E2} represent the corresponding friction time instants ($t_{E1} < t_{E2}$). Once the friction force is reversed in direction, the pulling motion away from the workpiece after the point E will lead to an increased transient shear angle, as shown in Figure 3.4(b). φ_{kc} and φ_{kr} are used to represent the transient shear angles before and after the tool edge passes the friction reversal point ($\varphi_{kc} < \varphi_{kr}$), and the value of φ_{kc} and φ_{kr} are assumed to be constant in the EVC process.

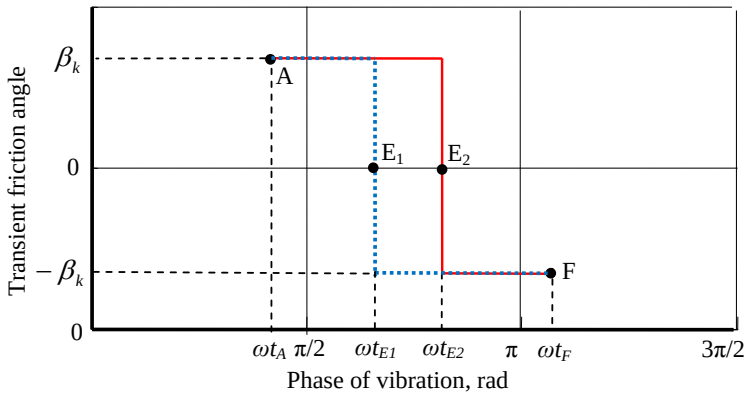

(a)

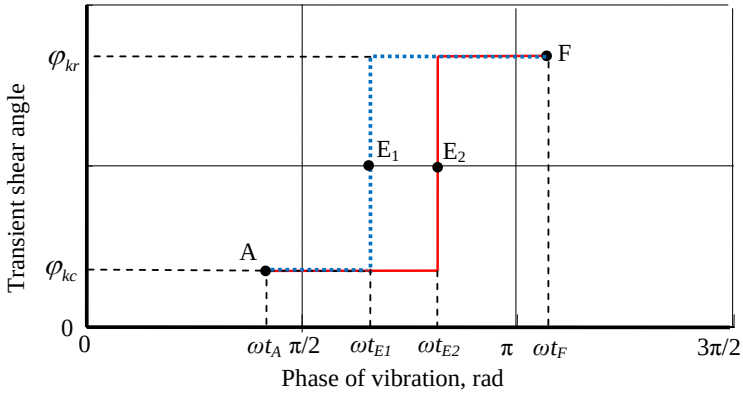

(b)

Figure 3.4. Schematic illustration of (a) transient kinetic-friction angle, and (b) transient shear angle in an EVC cycle.

Therefore, according to Figure 3.4, it can be predicted that, the smaller the value of t_E, the earlier the friction starts reversing, the earlier transient shear angle starts increasing, and hence the larger portion ($t_E \sim t_F$) of the increased shear angle φ_{kr}. Considering the inverse proportion relationship between the resultant force and the shear angle (see Equation (3.3)), it is reasonable to derive the following relationship between the friction reversal time and the transient resultant force:

$$t_E \downarrow \longrightarrow R(t) \downarrow \tag{3.6}$$

3.2 Experimental details

As mentioned in Chapter 2, it is known that researchers usually apply high-frequency vibration (at ultrasonic level of about 20 kHz or more) to enhance the productivity and cutting performances in practical metal cutting with the EVC method (Nath et al., 2009a; Shamoto and Moriwaki, 1999). However, it is impossible to measure the transient force values with ultrasonic frequency using the state-of-the-art measurement technology, due to the low natural frequency (about 5 kHz or less) of common dynamometers. It is because the measurement system may act as a low pass filter (Brehl and Dow, 2008), which is only able to measure the filtered time-averaged cutting force, but not the original transient force. Therefore, in order to study the transient cutting force in the EVC process, it is necessary to employ a low-frequency EVC method, instead of the ultrasonic EVC method.

The low-frequency elliptical vibration motion of the cutting tool relative to the workpiece is generated by a combined movement of the X- and Y- axes of a CNC ultraprecision machine tool (*Toshiba ULG-100H*[3]). The machine tool has a 10 nm linear resolution along the X-, Y- and Z- axes, which makes it reasonable to accurately drive the low-frequency EVC motion. In order to generate the elliptical vibration motion of tool tip, first, some ideal elliptical vibration loci are created by employing Equation (2.9) with preset cutting and vibration conditions. Then, the elliptical loci are fitted by sampling 360 points for each cutting cycle (i.e. every 2π phase), and G-codes are generated based on coordinates of the derived points. Figure 3.5 shows the schematic procedures for generating the low-frequency EVC motion.

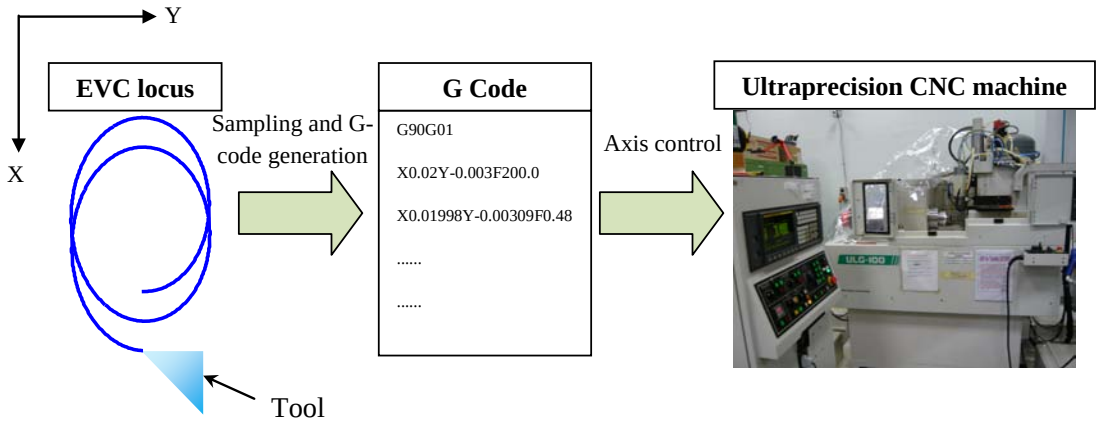

Figure 3.5. Illustration of the procedures for generating the low-frequency EVC motion.

In this study, a series of orthogonal EVC tests are conducted on 6061 aluminum alloy workpiece. Figure 3.6 shows a schematic illustration of the experimental setup for the cutting tests. The force signals are measured by a 3-component mini-dynamometer with 1 mN resolution mounted on the tool post and recorded with a real-time digitized recorder. In order to avoid the effect of tool edge geometry in this orthogonal EVC test, a flat-nose SCD tool is used, with 0^o rake angle and 7^o flank angle. Figure 3.7 shows a microscope photograph of the flat nose diamond tool, which has a 760 μm nose width. Its tool edge radius is measured to be about 0.15 μm by applying an indentation method proposed by previous researchers (Li et al., 2003).

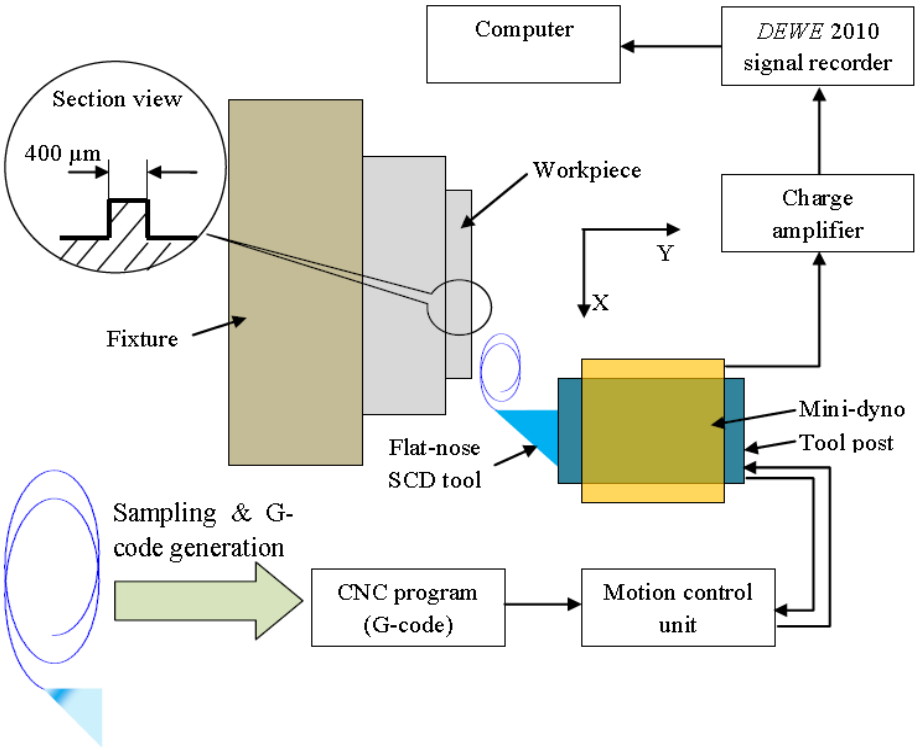

Figure 3.6. Illustration of the experimental set-up for the low-frequency EVC tests.

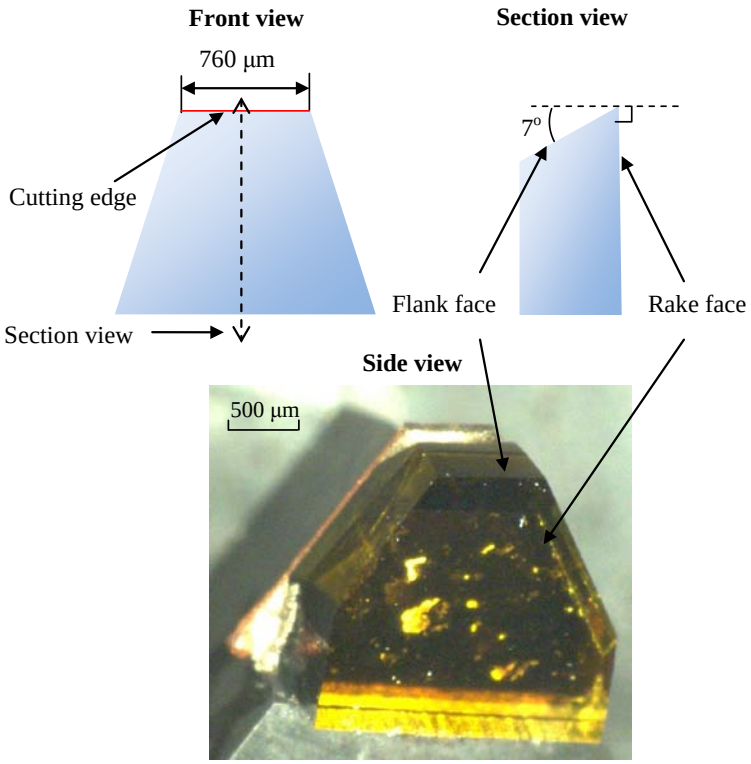

Figure 3.7. Microscope photograph (X50) of the flat nose diamond tool.

Table 3.1 shows the cutting and vibration conditions for the orthogonal EVC tests. The speed ratio in this table is changed by varying the value of v_c. Four different speed ratios, five principal amplitudes and five thrust amplitudes were selected to study their effects on the transient cutting force, while keeping the other cutting and vibration conditions unvaried. Figure 3.8 shows the experimental set-up for the cutting tests.

Table 3.1. Cutting and vibration conditions of the orthogonal EVC tests.

Tool	Flat nose diamond tool				
Workpiece	6061 aluminum alloy				
Width of cut, w [μm]	400				
Nominal uncut chip thickness, a_p [μm]	15				
Lubrication condition	Dry cutting				
Vibration frequency, f [Hz]	0.25				
Phase shift, ϕ [deg]	90				
Speed ratio, R_s (Nominal cutting speed, v_c [mm/min])	0.025 (0.047)	0.05 (0.094)	0.075 (0.141)	0.1 (0.188)	
Tangential amplitude, a [μm]	8	11	14	17	20
Thrust amplitude, b [μm]	2	5	8	11	14

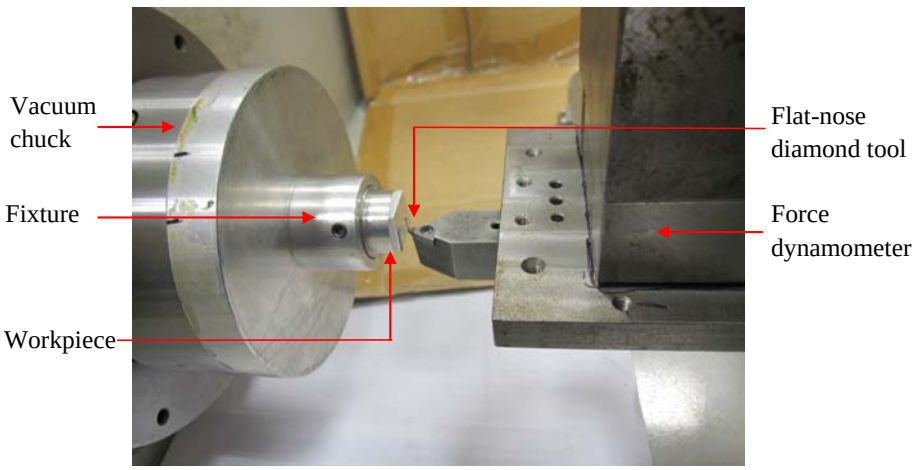

Figure 3.8. Experimental set-up for the orthogonal EVC tests.

3.3 Results and analysis

In this section, results of the transient cutting force at different speed ratios, tangential and thrust amplitudes are presented, and then the results are carefully analyzed and explained by comparing the values of TOC_t and friction reversal time for the specific cutting and vibration conditions.

3.3.1 Effect of speed ratio

Figure 3.9(a) shows the recorded experimental values of the transient force components (the principal and thrust force) in an EVC cycle at two speed ratios (0.025 and 0.1) with 20 μm tangential amplitude and 5 μm thrust amplitude. Figure 3.9(b) shows the values of the maximum resultant force R_{max} against different speed ratios.

From Figure 3.9(a), it can be seen that the transient principal force starts increasing from zero, reaches the maximum value at some point, then decreases slightly, and finally drops to zero after the disengagement of tool and chip. The transient thrust force starts from zero and increases gradually, which is similar to the trend of transient principal force in the beginning portion. However, after reaching its maximum positive value, it starts decreasing and becomes negative. Then, as time goes on, the thrust force remains negative in the following portion of the EVC cycle until the tool is fully disengaged with the formed chip. It means that the thrust force is reversed in direction, and such reversal process is considered to be caused by the reversed direction of friction between the tool rake face and the formed chip, indicating that the tool is pulling the chip upward from the workpiece. From Figure 3.9(b) It can be observed that the value of R_{max} increases gradually with the increment

of R_s. The value of R_{max} is increased by more than 45% when the speed ratio is increased from 0.025 to 0.1.

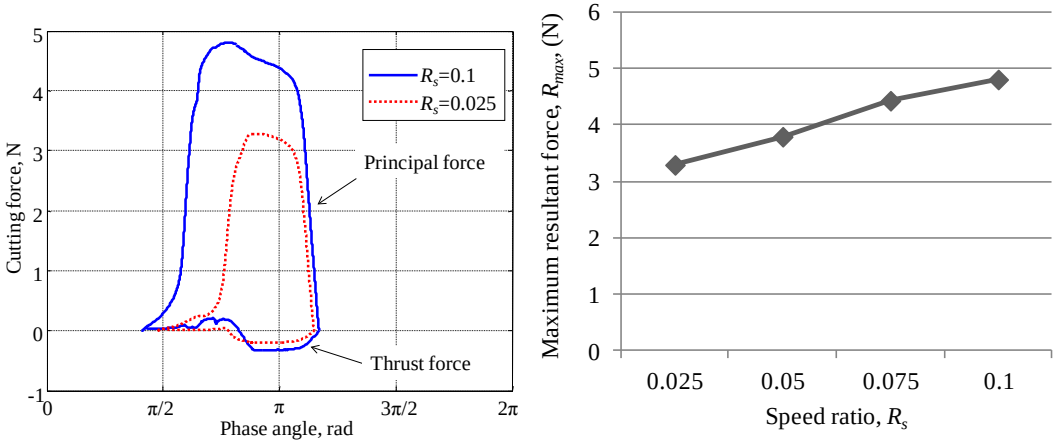

(a) (b)

Figure 3.9. The effect of speed ratio on (a) the transient cutting force components, (b) the maximum resultant cutting force.

In order to find the inherent reasons for the effects of speed ratio on transient cutting force, the values of TOC_t and $(TOC_t)_m$ against different speed ratios are calculated using Equation (3.1), as presented in Figure 3.10(a) and (b). The cutting and vibration conditions of Figure 3.10 are same with those of Figure 3.9. It can be observed that both the values of TOC_t and $(TOC_t)_m$ increase with the increment of the speed ratio, similar to the phenomenon shown in Figure 3.9. Considering the direct proportion relationship between TOC_t and the transient cutting force (see Equation (3.5)), the variation of TOC_t can be treated as a major reason for the variation tendency found in Figure 3.9.

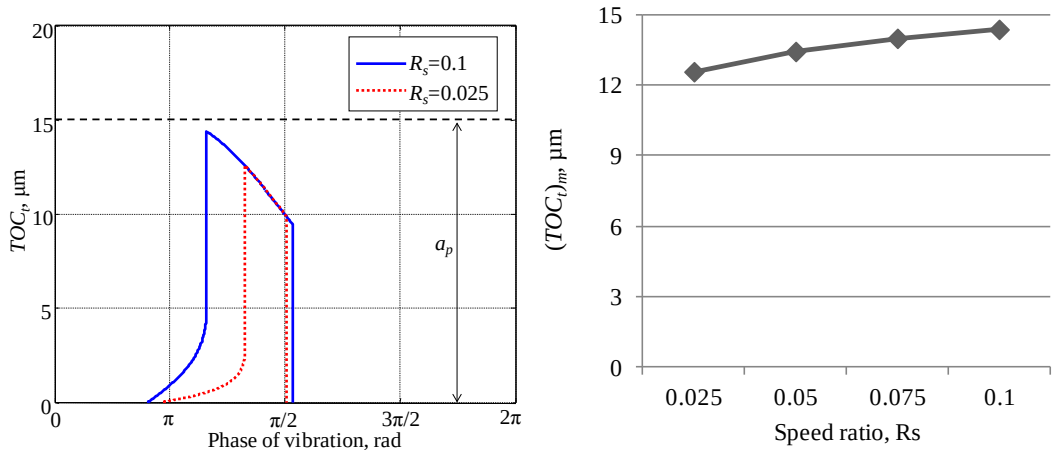

(a) (b)

Figure 3.10. The effect of speed ratio on the values of (a) TOC_t, (b) $(TOC_t)_m$.

As the tool rake angle is zero in the cutting tests, it can be derived that the transient friction force should be equal to the transient thrust force. Hence, the friction reversal time t_E can be calculated as the time when the thrust force is about to become negative. Figure 3.11 shows the values of t_E at different speed ratios. It can be seen that the value of t_E increases slightly with the increment of R_s, but the effect of speed ratio on the value of t_E is not significant. Hence, considering the direct proportion relationship between the transient cutting force and t_E (see Equation (3.6)), it can be concluded that the variation of friction reversal time may contribute as a minor reason for the variation tendency observed in Figure 3.9.

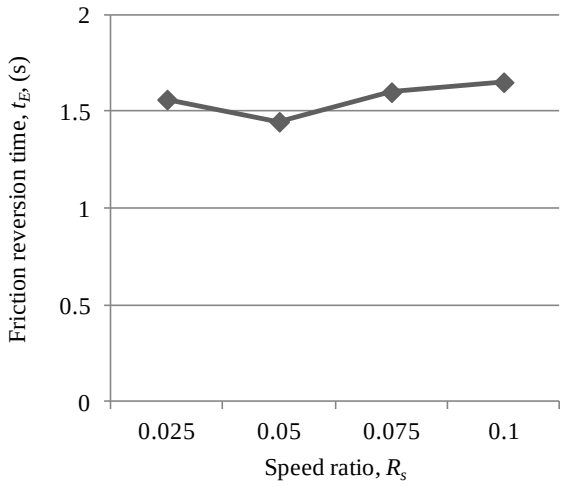

Figure 3.11. The effect of speed ratio on the value of friction reversal time.

3.3.2 Effect of tangential amplitude

In order to investigate the effect of tangential amplitude, the speed ratio is kept constant at 0.1 by changing the value of v_c accordingly, and the thrust amplitude is kept constant at 5 μm. Figure 3.12(a) and (b) show the effect of different tangential amplitudes on the transient cutting force and R_{max}. It can be seen from Figure 3.12 that the value of transient cutting force increases gradually with the increment of tangential amplitude, and the value of R_{max} is increased by 35% when the tangential amplitude is increased from 8 to 20.

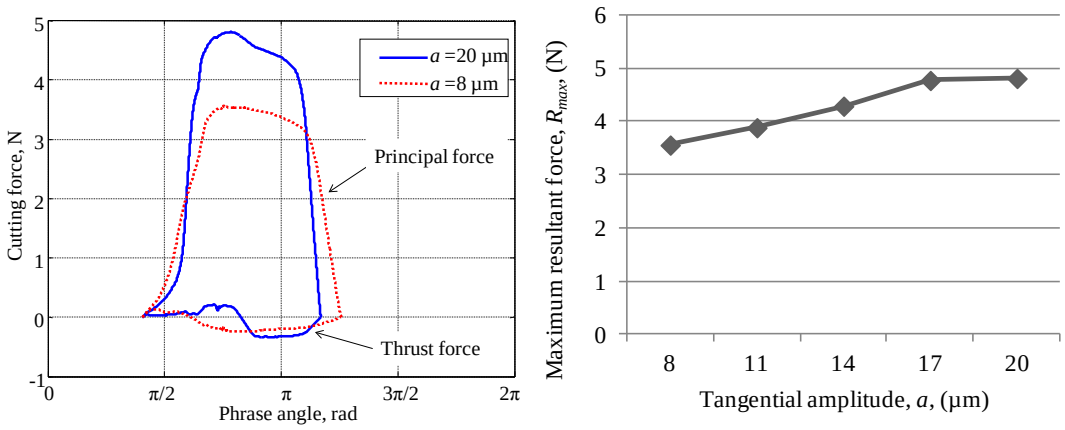

(a) (b)

Figure 3.12. The effect of tangential amplitude on (a) the transient cutting force components, (b) the maximum resultant cutting force.

Figure 3.13(a) and (b) show the value of TOC_t and $(TOC_t)_m$ at different tangential amplitudes. It can be observed from Figure 3.13(a) that the value of TOC_t is identical at different tangential amplitudes. Accordingly, the value of $(TOC_t)_m$ does not change against the tangential amplitude. Hence, it can be concluded that the variation of TOC_t is not a reason for the variation tendency found in Figure 3.12. Figure 3.13(c) shows that the value of t_E increases gradually with the increment of tangential amplitude. Considering the direct proportion relationship between t_E and the transient cutting force described in the above section, it is reasonable to derive that the increment of transient cutting force with the increment of tangential amplitude is caused by the increment of the friction reversal time. The larger value of t_E will postpone the occurrence of friction reversal, and hence reduce the portion of increased transient shear angle in the EVC process.

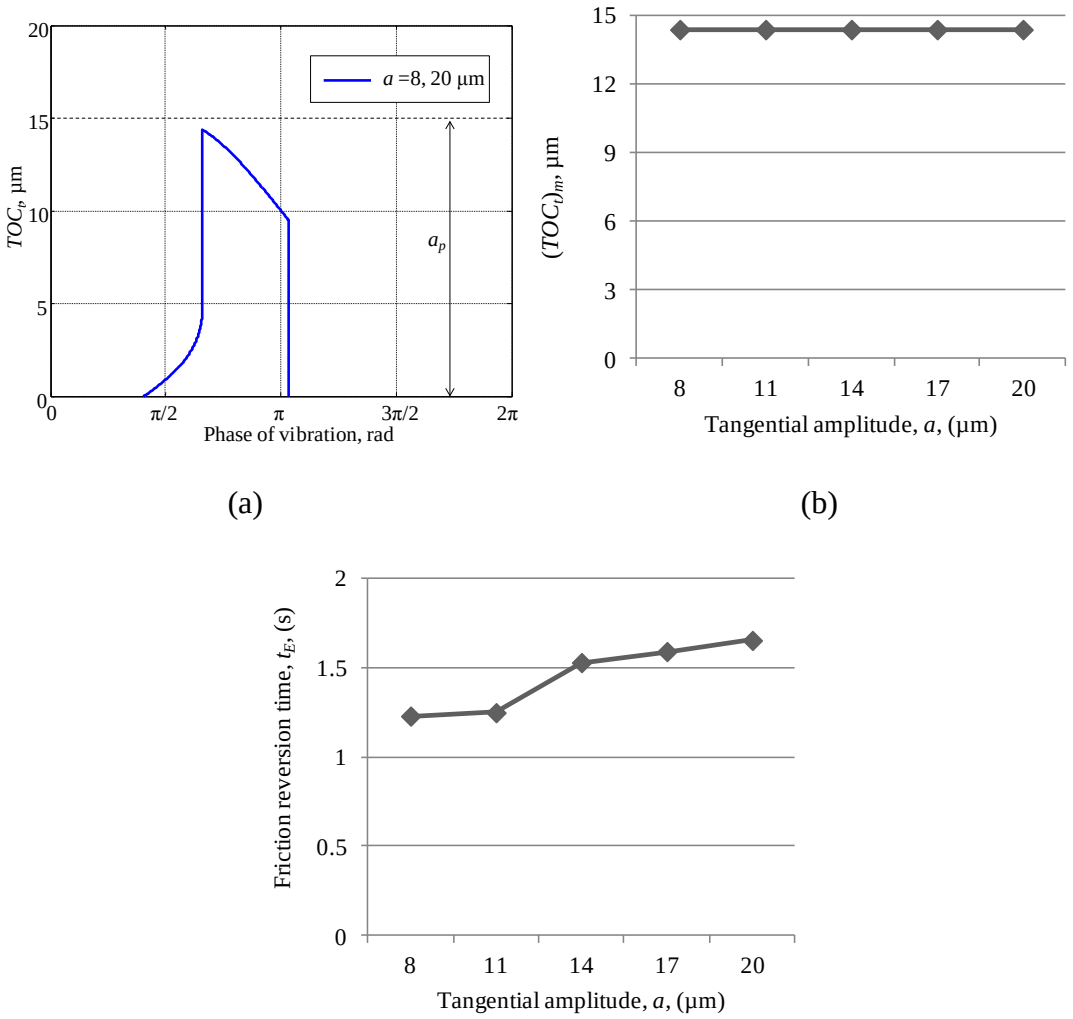

Figure 3.13. The effect of tangential amplitude on the values of (a) TOC_t, (b) $(TOC_t)_m$, (c) friction reversal time.

3.3.3 Effect of thrust amplitude

Figure 3.14(a) and (b) show the effect of different thrust amplitudes on the transient cutting force and R_{max} with 20 µm tangential amplitude and 0.1 speed ratio. Unlike the case for the tangential amplitude, it can be observed that the value of R_{max} decreases with the increment of thrust amplitude, and the value of R_{max} is decreased by about 40% when the thrust amplitude is increased from 2 to 14.

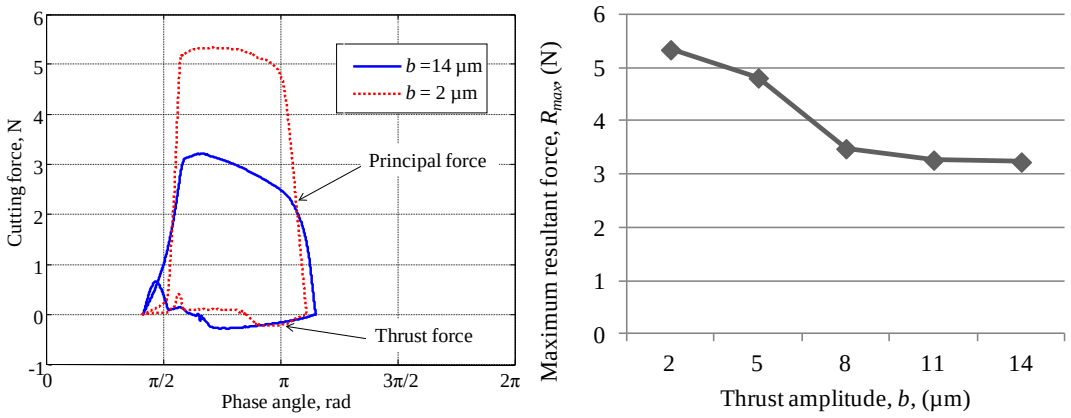

(a) (b)

Figure 3.14. The effect of thrust amplitude on (a) the transient cutting force components, (b) the maximum resultant cutting force.

Figure 3.15(a) and (b) show the values of TOC_t, $(TOC_t)_m$ and t_E at different thrust amplitudes. It can be seen that TOC_t and $(TOC_t)_m$ gradually decreases with the increment of thrust amplitude. Figure 3.15(c) shows that the value of t_E also decreases with the increment of thrust amplitude. Considering the direct proportion relationship between the transient cutting force and the values of both TOC_t and t_E, it can be concluded that the decrement of TOC_t and t_E contribute as two major reasons for the variation tendency of transient cutting force.

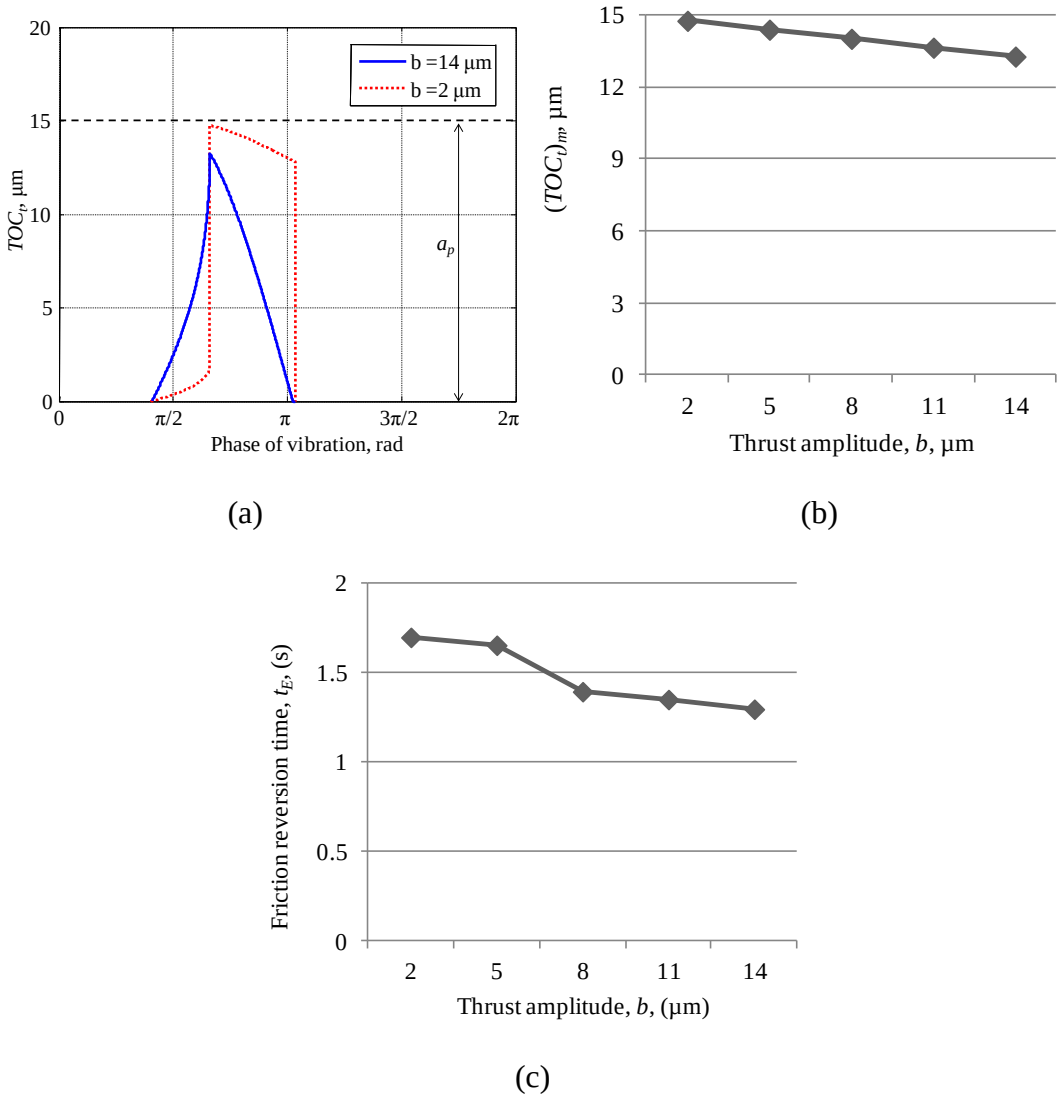

Figure 3.15. The effects of thrust amplitude in the EVC process on the values of (a) TOC_t, (b) $(TOC_t)_m$, (c) friction reversal time.

3.4 Concluding remarks

In this chapter, the effects of three essential cutting and vibration parameters (speed ratio, tangential and thrust amplitudes) on the transient cutting force in EVC are experimentally investigated by conducting a series of low-frequency EVC tests. A calculation method for the value of transient thickness of cut is proposed based on the

geometrical relationship in the EVC process. By analyzing the transient TOC and friction reversal time, the experimental results are analytically explained. Based on the results and analysis, the following conclusions can be drawn:

- The transient cutting force increases with the increment of speed ratio, and such variation tendency is considered to be caused mainly by the increment of transient TOC due to the variation of the elliptical vibration loci.

- The transient force increases with the increment of tangential amplitude. Such phenomenon is considered to be caused by the increment of friction reversal time; and the transient TOC for different tangential amplitudes is identical when the speed ratio and the thrust amplitude are kept constant.

- Larger thrust amplitude leads to smaller transient cutting force, which is considered to be caused by both the smaller transient TOC and the smaller friction reversal time.

Chapter 4: Modeling of transient cutting force for the EVC method

Very few studies have been done to investigate the basic cutting mechanics and predict the cutting performance in the EVC process (Brehl and Dow, 2008). In the previously developed analytical models (Shamoto et al., 2008), Shamoto et al. proposed a calculation method for determining transient cutting force values in the EVC process. However, two important inherent characteristics (the transient TOC and the transient shear angle) were not considered in their model. Although the characteristic of friction reversal in the EVC process was analyzed in their study, the transition characteristic of such reversal process was overlooked. Because of these, their models may not express the actual cutting mechanics of the EVC process and thus can not accurately predict the cutting force values.

In this chapter, an analytical force model for the orthogonal EVC process is developed to fully understand the material removal mechanism and accurately predict the transient cutting force values. Three important factors were investigated and considered in this model, including i) transient TOC, ii) transient shear angle, and iii) transition characteristic of friction reversal. In order to validate the proposed force model, an orthogonal CC test with the same tool/workpiece combination is conducted to calibrate the values of shear stress and tool-chip kinetic-friction angle for the model validation. Finally, the predicted force values calculated based on the proposed model

are compared with the experimental cutting force values at different cutting conditions, and some relevant issues observed from the results are discussed.

4.1 Development of the force model

4.1.1 Transient thickness of cut

For the CC method, the TOC of work material, which is also known as the uncut chip thickness a_p, is constant throughout the cutting process (see Figure 3.2). According to the conventional metal cutting theory (Oxley, 1989), the resultant force should be in direct proportion with t_0 (see Equation (3.3)). Although EVC is different from CC in the material removal process, the fundamental cutting mechanism should be identical, and hence the transient resultant cutting force $R(t)$ in the EVC process applied on the cutting tool should also be in direct proportion to the value of TOC_t.

As presented in Chapter 3, the transient TOC in EVC continuously varies in each cutting cycle (see Figure 3.1) and its value is determined by various machining and vibration parameters in the EVC process (see Equation (3.1)). For example, the value of $(TOC_t)_m$ increases with the increment of speed ratio R_s, stays constant with the variation of tangential amplitude a, and decreases with the increment of thrust amplitude b.

4.1.2 Transient shear angle and transition characteristic of friction reversal

According to the famous thin shear plane theory (Merchant, 1945a, b; Oxley, 1989), the velocity relationship in metal cutting process can be expressed as follows:

$$\vec{v}_s = \vec{v}_t + \vec{v}_{ct} \tag{4.1}$$

For the CC method, the tool velocity $\vec{v}_t$ always stays invariant in direction, the shear velocity $\vec{v}_s$ and the chip velocity $\vec{v}_{ct}$ also remain constant in direction, as shown in Figure 3.2. Due to the sliding movement of the chip on the tool rake face throughout the CC process, kinetic friction is induced and tends to push the chip material down toward the workpiece.

For the EVC method, each cutting cycle starts with the sliding movement of the chip or work material over the tool rake face, which is similar to that in the CC method. However, as $\vec{v}_t$ continuously varies in its direction clockwise, the direction of $\vec{v}_{ct}$ or the relative sliding movement will get reversed in direction sooner or later (see Figure 3.3). Due to such reverse-direction sliding movement, the friction direction will be reversed subsequently, and such reverse-direction friction can eventually pull up the formed chip material along the tool rake face.

As each EVC cycle starts with the sliding movement like the CC process and ends with the reverse-direction sliding movement, it can be stated that two kinetic-friction zones with the sliding movement exists in each cutting cycle. The first kinetic-friction zone (named as CC-like kinetic-friction zone) exists in the beginning portion of each cycle which starts at t_A, while the other kinetic-friction zone (named as reverse kinetic-friction zone) exists in the ending portion which closes at t_F. Due to the direction reversal of $\vec{v}_{ct}$ and the kinetic-friction force, these two kinetic-friction zones will have different shear velocities $\vec{v}_s$ and hence different shear plane angles.

Lee and Shaffer derived that in cutting process the shearing occurs along the maximum shear stress (MSS) direction, i.e., where the angle between the shear

velocity and the direction of resultant force is 45^o ($\delta = 45^o$) (Lee and Shaffer, 1951). Although their model is based on an assumption of rigid-perfectly plastic work material and neglects effects of built-up edge (BUE) and thick shear zone on the rake face, it still gives a comprehensive physical understanding of metal cutting mechanics. Hence, in the present study, in order to determine the shear plane angles and boundaries of the two kinetic-friction zones, Lee and Shaffer's slip-line solution is extended and applied.

Based on Lee and Shaffer's model, both the slip-line field and force relationships for CC-like kinetic-friction zone are plotted in Figure 4.1(a). A triangular plastic region OMN above the shear direction with the slip lines parallel or perpendicular to OM is assumed, and the resultant force R makes 45^o with the direction of the shear force F_s. The other symbols, F_{ns}, F_n, F_p and F_t represent the normal force perpendicular to the shear direction, the normal force perpendicular to the rake face, the principal force along the nominal cutting direction, and the thrust force perpendicular to the nominal cutting direction, respectively. β_k represents the kinetic-friction angle between the tool rake face and the work material, and its value is assumed to remain constant throughout the cutting process. According to the force relationships in CC process (Merchant, 1945a), β_k can be derived from the following equation:

$$\beta_k = \tan^{-1}(F_f / F_n) = \tan^{-1}[(F_t \cos\gamma + F_p \sin\gamma)/(F_p \cos\gamma - F_t \sin\gamma)] \qquad (4.2)$$

Although Lee and Shaffer's model was developed for the CC process, the same fundamental laws of plasticity and MSS principle can also be applied to obtain the slip-line filed for the reverse kinetic-friction zone as well. Figure 4.1(b) shows the derived slip-line filed and the force relationships for reverse kinetic-friction zone. Due

to the reverse-direction sliding movement mentioned earlier, the friction force F_f in reverse kinetic-friction zone is opposite in direction to that in the CC-like kinetic-friction zone, and accordingly the direction of the resultant force R in Figure 4.1(b) should be rotated clockwise by $2\beta_k$ relative to the one in Figure 4.1(a).

As the kinetic-friction angle β_k remains constant, the direction of R will stay invariant in each kinetic-friction zone, and hence the shear force F_s will also stay unchanged in each zone according to the MSS principle. Hence, the shear angles (symbolized as φ_{kc} and φ_{kr}) for CC-like and reverse kinetic-friction zones can be reasonably assumed to be remain constant in each zone. Then, based on the force relationships shown in Figure 4.1(a) and (b), the values of φ_{kc} and φ_{kr} can be determined by the tool rake angle γ and the kinetic-friction angle β_k as:

$$\varphi_{kc} = 45^o - (\beta_k - \gamma) \tag{4.3}$$

$$\varphi_{kr} = 45^o + (\beta_k + \gamma) \tag{4.4}$$

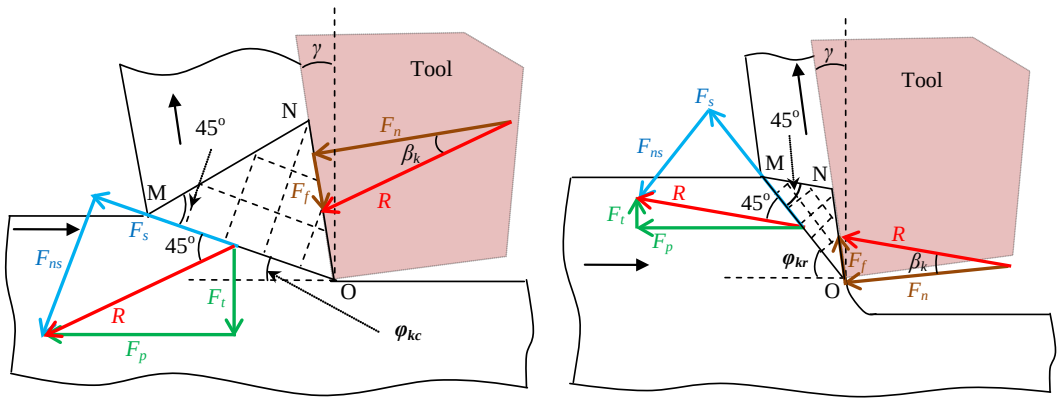

(a) (b)

Figure 4.1. Slip-line fields and force relationships for a single EVC cycle in: (a) CC-like kinetic-friction zone, (b) Reverse kinetic-friction zone.

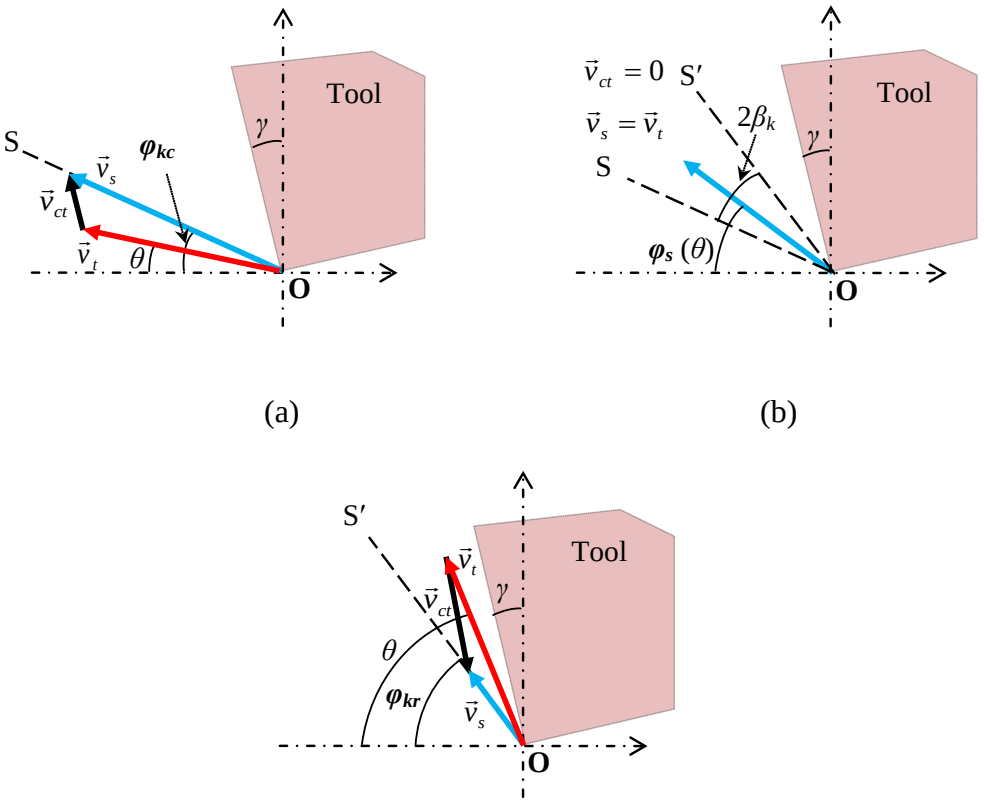

Figure 4.2. Velocity diagrams for a single EVC cycle in: (a) CC-like kinetic-friction zone, (b) Static-friction zone, (c) Reverse kinetic-friction zone.

Given the determined shear angles, the velocity diagrams based on Equation (4.1) for the two kinetic-friction zones can be plotted in Figure 4.2(a) and (c), where the two dashed lines OS and OSrepresent the two constant directions of $\vec{v}_s$. In Figure 4.2(a), $\vec{v}_{ct}$ will get close to zero when $\vec{v}_t$ is approaching $\vec{v}_s$ in direction. Since kinetic friction only exists when the sliding movement occurs (i.e., $\vec{v}_{ct}$ is not zero), in CC-like kinetic-friction zone, the direction of $\vec{v}_t$ should not rotate over OS. Otherwise, the relative sliding movement and the chip velocity $\vec{v}_{ct}$ may change in direction or in

nature, and such variation could lead to the occurrence of a reverse friction direction or another friction mode. Similar analysis can also be applied to reverse kinetic-friction zone, where $\vec{v}_t$ should not stay below OS' in order to allow the existence of the reverse-direction sliding movement, as shown in Figure 4.2(c). Thus, the two shear directions OS and OS' can be treated as the upper or lower boundaries of the two kinetic-friction zones, respectively.

In mechanics, friction behavior can be divided into two main regimes: gross sliding and pre-sliding, where kinetic friction and static friction dominate the process, respectively. It is known that the kinetic friction does not immediately reverse in direction from one gross sliding movement to the reverse-direction gross sliding movement, and pre-sliding regime should exist as a transition zone during the reversal process. In the EVC process, such transition zone (named as static-friction zone) acts as an intermediate zone connecting the two kinetic-friction zones. Figure 4.2(b) shows the velocity diagram for this transition zone, where its lower and the upper boundaries are assumed to be determined by the obtained two shear directions in the two kinetic-friction zones, OS and OS'. Once $\vec{v}_t$ passes over OS', the static friction will then get converted back to kinetic friction due to the nonzero $\vec{v}_{ct}$ and the induced gross sliding movement. Since no gross sliding movement occurs in this pre-sliding transition regime (i.e. $\vec{v}_{ct} = 0$), according to the velocity relationship described in Equation), the shear velocity $\vec{v}_s$ will be identical to $\vec{v}_t$ in both direction and magnitude. Based on such equivalence relation, it can be derived that the transient shear angle φ_s for this transition zone is equal to the transient tool velocity angle:

$$\vec{v}_s = \vec{v}_t, \quad \Rightarrow \varphi_s = \theta(t) \tag{4.5}$$

Overall, based on the above analysis, the transient shear plane angle (symbolized as φ_t) in the three consecutive zones can be described with specific zone boundaries as:

$$\varphi_t = \begin{cases} \varphi_{kc}, & \theta(t_A) \le \theta(t) < \varphi_{kc} \\ \varphi_s, & \varphi_{kc} \le \theta(t) \le \varphi_{kr} \\ \varphi_{kr}, & \varphi_{kr} < \theta(t) \le \theta(t_F) \end{cases} \tag{4.6}$$

Figure 4.3(a) and (b) show a schematic sketch for the three friction zones versus the tool velocity direction and the tool location in an EVC cycle. It can be seen that the three consecutive zones, namely CC-like kinetic-friction zone, static-friction zone and reverse kinetic-friction zone, follow a kinetic-static-kinetic friction transformation procedure in each cutting cycle. In Figure 4.3(a), the two dashed lines, OA and OF, represent the lower and upper boundaries of a complete cutting cycle, i.e., the cutting-start tool velocity direction and the cutting-end tool velocity direction.

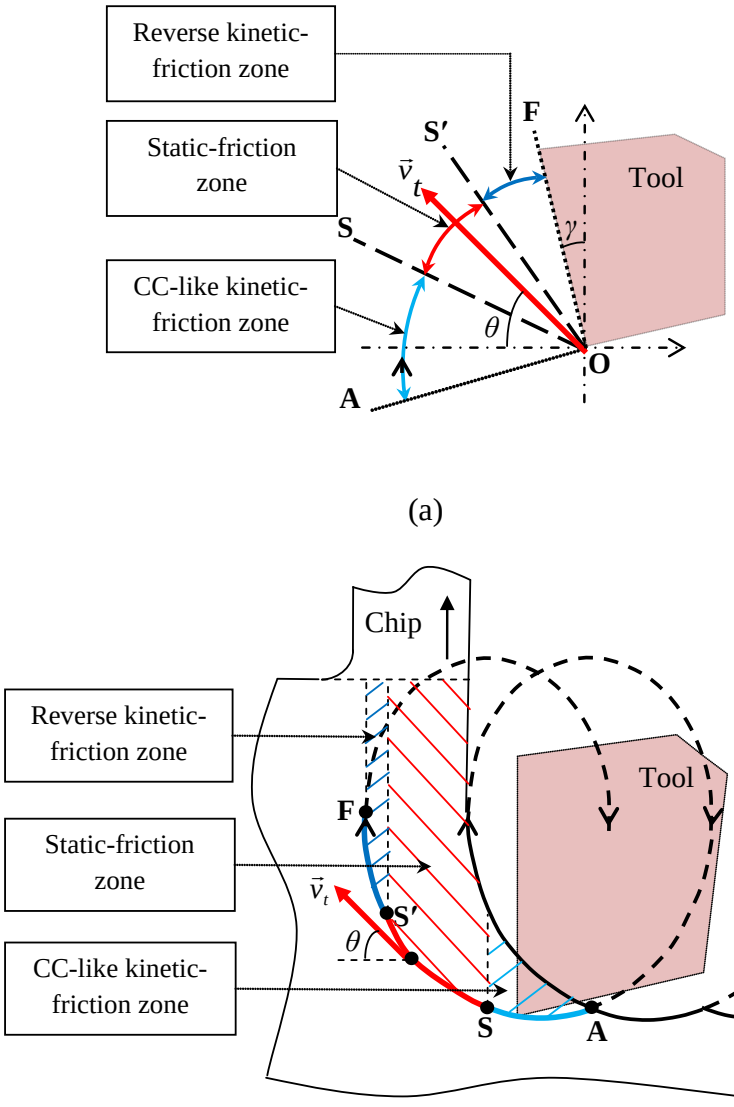

(a)

(b)

Figure 4.3. Schematic sketch of the three consecutive friction zones in an EVC cycle versus: (a) tool velocity direction, (b) tool location.

As an example, Figure 4.4 plots the simulated results of the transient shear angle (φ_t) versus the phase of vibration for an EVC cycle with two given kinetic-friction angles (β_k) using Equation (4.6). β_k is determined by various cutting conditions, such as material types of tool/workpiece combination and cooling condition (e.g. with or

without coolant). The two friction angles (15° and 30°) in this figure are identified from the friction coefficients of tungsten carbide *vs* tungsten carbide (0.25) and tungsten carbide *vs* steel (0.6). The points A, F, S and S' represent the cutting -start point, the cutting-end point, and the lower and upper limits of static-friction zone, respectively. From this figure, it can be remarked that static-friction zone plays a significant role in the whole cutting cycle. Moreover, it can also be followed that a smaller kinetic-friction angle can lead to comparatively i) a larger conventional shear angle (φ_{kc}) in the CC-like kinetic-friction zone, ii) a shorter phase length in the static-friction zone, and iii) a smaller shear angle (φ_{kr}) in the reverse kinetic-friction zone. Such characteristic of the cutting mechanics with the EVC method looks completely different from that with the CC method, where the latter is characterized by an invariant shear angle through the CC process.

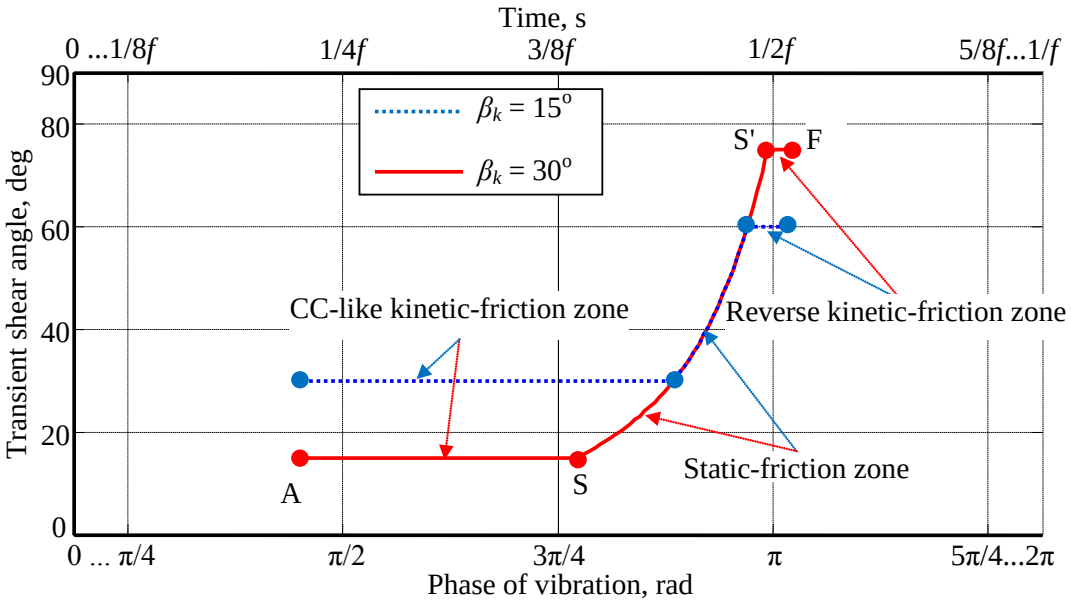

Figure 4.4. Example of transient shear angle for a cutting cycle in orthogonal EVC process at the conditions: 0° tool rake angle, 0.094 mm/min nominal cutting speed, vibration amplitude (a=20 µm, b=5 µm), 0.25 Hz frequency, 90° phase shift.

4.1.3 Transient cutting force components

It is understood that the output cutting force during mechanical cutting process highly depends on material load on the tool rake face. The higher the TOC, the higher the material load is. Due to the variation of TOC and the variation of shear angle in the EVC process, the cutting force gets continuously varied in each cutting cycle. In fact, according to the illustration of TOC_t in Figure 3.1, the transient force value may start from zero at the cutting-start point A, reaches the maximum at elsewhere in the loci and ends with zero again at the cutting-end point F. In order to derive such transient cutting force, the famous thin shear plane model (Merchant, 1945a) is applied and slightly modified here, and β_k and τ in the EVC process are assumed to be constant and equal to those found with the CC method.

It is known that, in the CC process, the shear force along the fixed shear plane is calculated as:

$$F_s = \frac{\tau w}{\sin \varphi_c} t_0 \tag{4.7}$$

where t_0 is the fixed uncut chip thickness, and φ_c is the constant shear angle. For the EVC process, if t_0 and φ_c in Equation (4.7) are replaced with TOC_t and φ_t, the transient shear force $F_s(t)$ can be obtained as:

$$F_s(t) = \frac{\tau w}{\sin \varphi_t} TOC_t \tag{4.8}$$

The value of $F_s(t)$ can be calculated with given values of TOC_t and φ_t, which are determined by Equations (3.1) and (4.6), respectively.

According to Lee and Shaffer's MSS principle (Lee and Shaffer, 1951), the angle between the shear direction and the resultant force direction is 45^o. Therefore, the transient resultant force $R(t)$ during cutting in each cycle can be obtained as:

$$R(t) = \frac{F_s(t)}{\cos 45^o} \tag{4.9}$$

Then according to the force relationships shown in Figure 4.1, the transient principal force $F_p(t)$ and the transient thrust force $F_t(t)$ along the *x*- and *y*- axes, can be derived as follows:

$$F_p(t) = R(t)\cos(45^o - \varphi_t) \tag{4.10}$$

$$F_t(t) = R(t)\sin(45^o - \varphi_t) \tag{4.11}$$

In order to calculate the values of these two transient cutting force components using Equations (4.10) and (4.11), β_k and τ need to be determined from the experimental results of the orthogonal CC test. Under the CC condition, the kinetic-friction angle, β_k can be calculated from Equation (4.2) with given values of F_p and F_t, and the shear stress τ can be derived according to the conventional thin shear plane model (Merchant, 1945a):

$$\tau = \frac{R\cos(\varphi_c + \tan^{-1}(F_t / F_p))}{w(t_0 / \sin\varphi_c)}, \qquad \text{where } R = \sqrt{F_t^{\,2} + F_p^{\,2}} \tag{4.12}$$

where φ_c can be derived from the following equation (Merchant, 1945a):

$$\varphi_c = \tan^{-1}\frac{t_0\cos\gamma}{t_c - t_0\sin\gamma} \tag{4.13}$$

where t_c is the measured chip thickness.

With the values of β_k and τ calibrated through CC tests, the transient cutting force components for the EVC process can be subsequently calculated. Figure 4.5 shows a flow chart of the whole calculation procedures of the transient force components based on the proposed model.

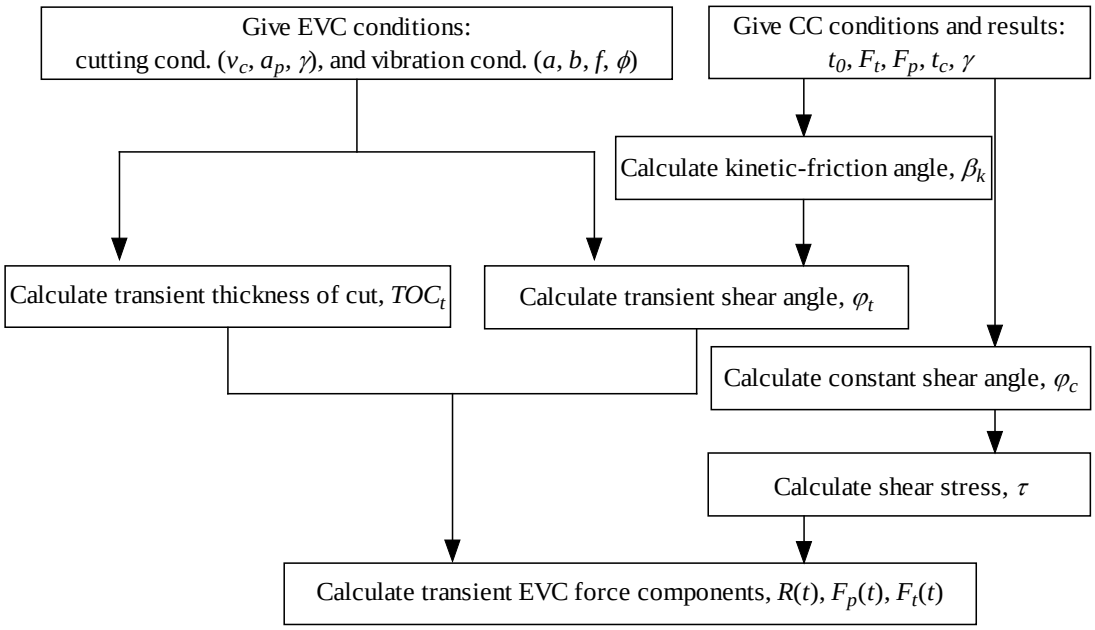

Figure 4.5. Flow chart of the calculation procedures for the analytical EVC force model.

4.2 Verification for the proposed model

In this section, the proposed analytical force model for the orthogonal EVC process is experimentally validated. Using the calibrated parameters, the proposed force model is employed to predict values of the transient cutting force components, and these values are compared with the experimental force values obtained from the EVC test.

4.2.1 Calibration for the parameters

An orthogonal CC test (i.e., without the tool vibration) is conducted to calibrate the two important parameters (τ and β_k). Table 4.1 shows detailed conditions for the orthogonal CC test, and the experimental set-up can be seen in Figure 3.8.

Table 4.1. Cutting and vibration conditions for the orthogonal CC test.

Uncut chip thickness, t_0 [μm]	15
Width of cut, w [μm]	400
Cutting speed, [mm/min]	0.188
Lubrication condition	Dry cutting

For the orthogonal CC test, Figure 4.6(a) shows the recorded values of the cutting force components, and Figure 4.6(b) shows the microscope photograph of the formed chip in the CC process. Based on the experimental results, the average thrust force F_t and the average principal force F_p were calculated to be 0.4 N and 6.6 N, respectively. The average thickness of the generated chip, t_c is measured to be about 41 μm. Therefore, by substituting the values of F_t, F_p, t_c, w and t_0 into Equations (4.2), (4.12) and (4.13), the constant shear angle φ_c is calculated to be 20^o, and the values of β_k and τ for the CC condition are found to be 3.46^o and 347 MPa, respectively.

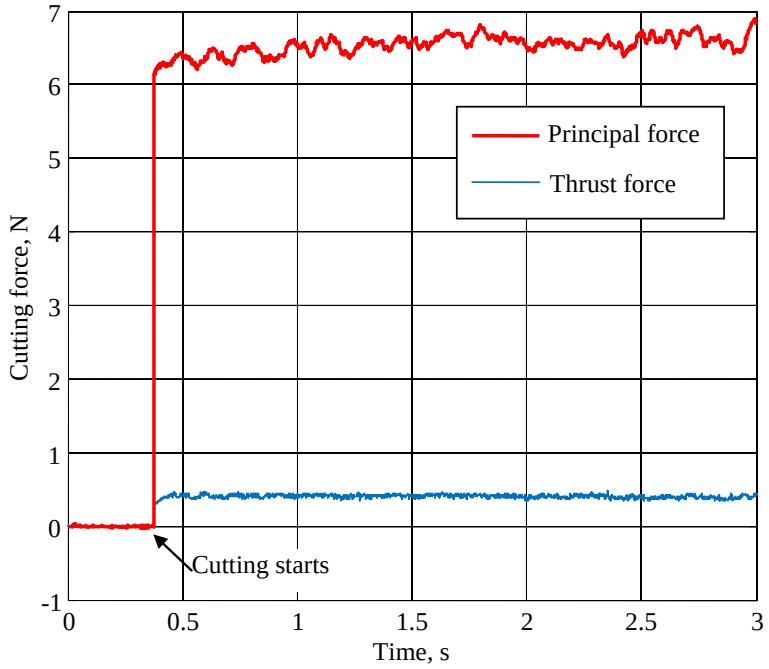

(a)

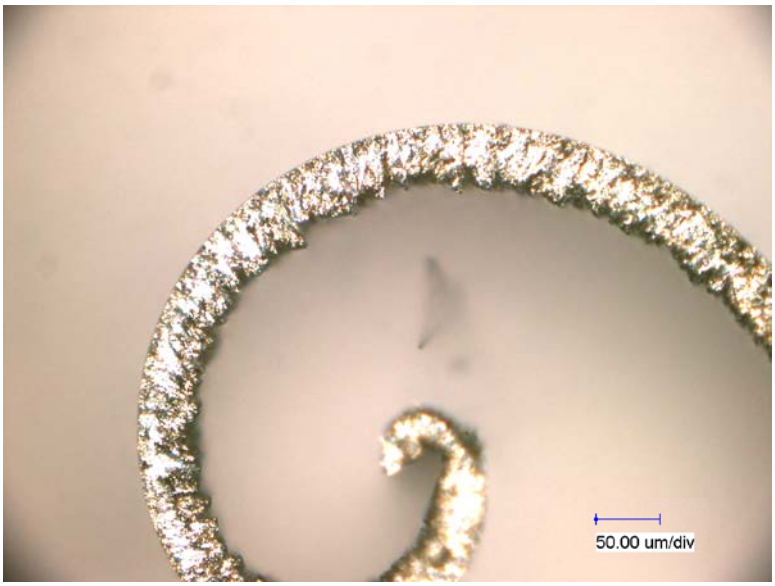

(b)

Figure 4.6. Experimental results for the CC process: (a) Cutting force components, (b) Microscope photograph (X450) of the formed chip.

4.2.2 Validation for the developed model

By following the calculation method shown in Figure 4.5, the transient cutting forces are calculated given the cutting and vibration conditions listed in Table 4.1 and the calibrated two parameters β_k and τ. As stated in Chapter 3, according to the existing studies (Nath et al., 2011; Shamoto et al., 2008), speed ratio is considered as one of the most essential parameters in the EVC method (Nath et al., 2011; Shamoto et al., 2008). Therefore, in the orthogonal EVC tests, different speed ratios are employed to study the applicability of the proposed model. The experimental transient cutting force values can be obtained from Chapter 3.

Figure 4.7 shows the comparison between the predicted and experimental maximum transient resultant forces, R_{max}, at the four different speed ratios. It can be seen that both the predicted and experimental values of R_{max} increase with the increment of speed ratio. The comparison results in Figure 4.7 shows that the predicted values of R_{max} correspond well with the experimental values, indicating that the effect of different speed ratios on transient cutting force can be effectively predicted by the proposed force model.

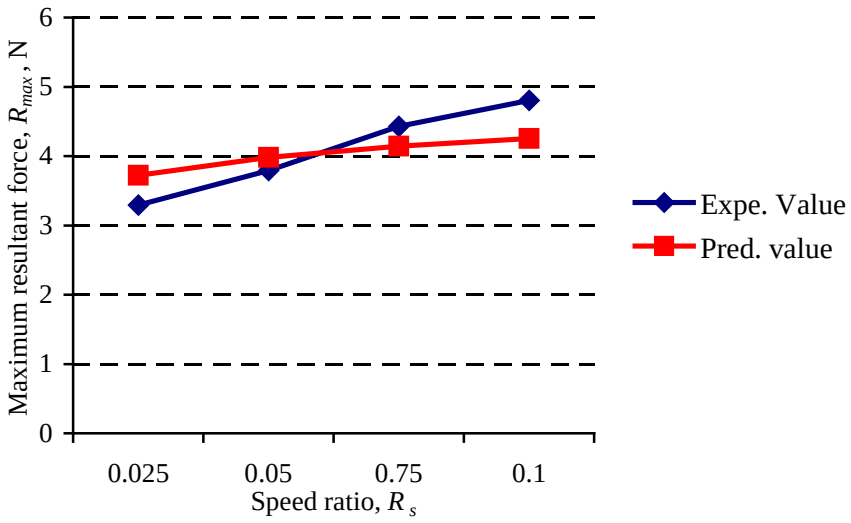

Figure 4.7. Experimental and predicted maximum transient resultant cutting force with different speed ratios.

As an example, Figure 4.8 shows the predicted transient principal and thrust force (i.e. $F_p(t)$ and $F_t(t)$) with the four speed ratios (0.025, 0.05, 0.075 and 0.1), and the retrieved experimental force values are superimposed in the same figure for comparison. It can be seen from Figure 4.8 that the transient principle force first increases due to the increasing TOC_t (see Figure 3.1), then decreases slightly due to both the increasing φ_t (see Figure 4.4) and the decreasing TOC_t, and finally drops to zero after the disengagement of tool and chip. For the predicted principal force, it can be noticed that its variation trend and zero-to-peak value correspond well with those of the experimental one.

It can also be noticed from Figure 4.8 that the transient thrust force first starts increasing from zero to a maximum positive value, but then gradually decreases to negative values, indicating that the tool is pulling the chip or work material upward

from the workpiece. Such unique phenomenon which is completely different from the CC process is caused by the friction reversal in each cutting cycle of the EVC process.

From Figure 4.8, it can also be observed that the predicted cutting-end point (the point where the principal or the thrust force becomes zero) does not agree with the experimental one, indicating that the tool still stays engaged with the work or chip material after passing over the theoretical cutting-end point. This kind of disaccord is considered to be caused by elastic recovery of either the work or the chip material at this stage. That means when the tool edge passes the theoretical cutting-end, the work or chip material will gradually rebound elastically with the receding movement of the tool, until its elastic energy is completely released and it is truly disengaged from the tool rake face.

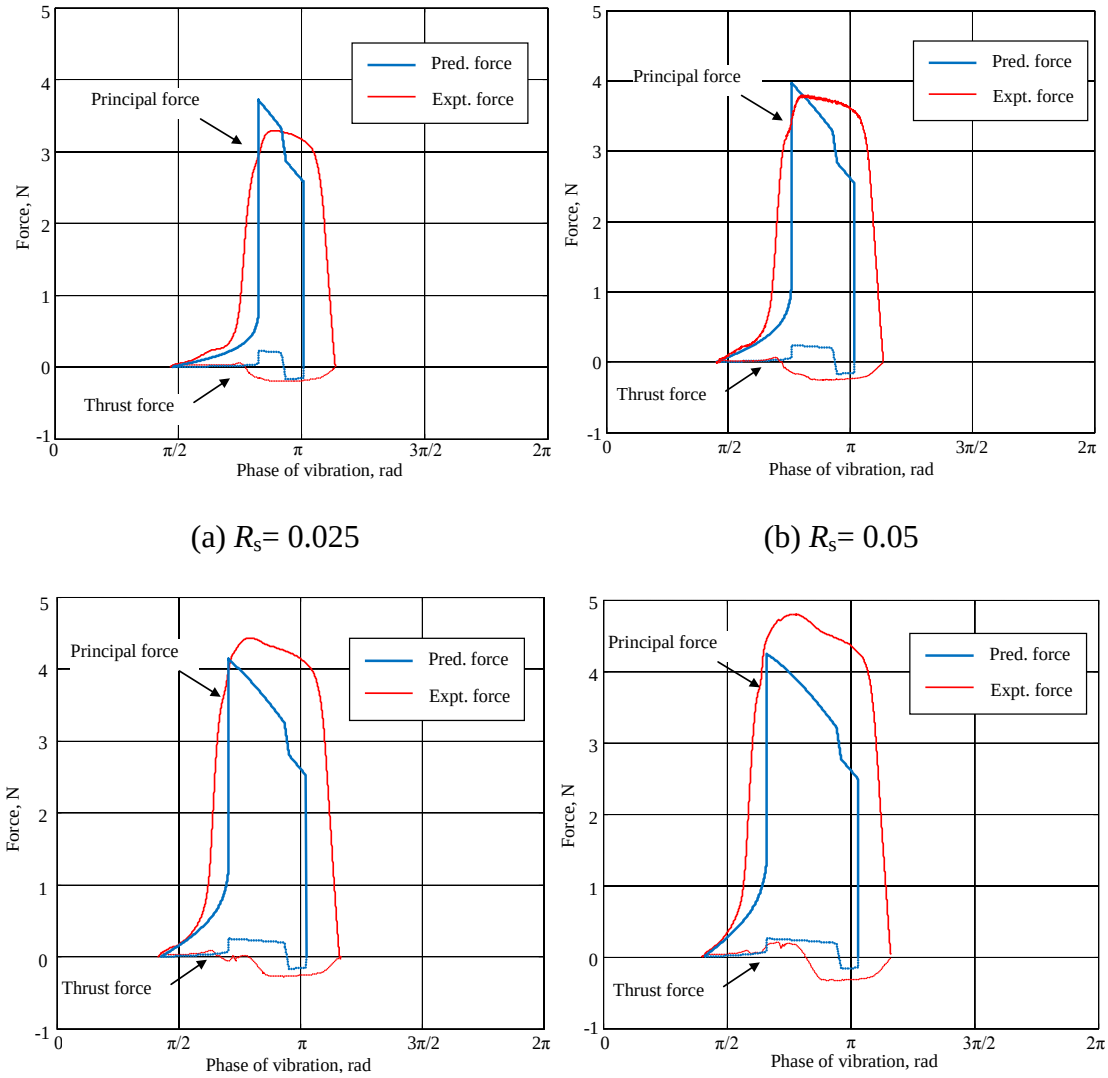

(a) R_s= 0.025 (b) R_s= 0.05

(c) R_s= 0.075 (d) R_s= 0.1

Figure 4.8. Experimental and predicted transient cutting force components for an EVC cycle.

4.3 Concluding Remarks

In this chapter, an analytical force model for orthogonal EVC process has been developed for in-depth understanding of the transient cutting mechanics and for accurate prediction of the transient cutting force components. Based on this study, the following conclusions can be drawn:

- By analyzing transition characteristic of friction reversal in the EVC process, static friction is considered to exist in the transition zone between the two kinetic-friction zones. Based on variation of the friction modes, each cutting cycle is divided into three consecutive zones: CC-like kinetic-friction zone, static-friction zone and reverse kinetic-friction zone.

- Transient shear angles for the three friction zones are derived by investigating the velocity relationship and employing the Lee and Shaffer's slip-line solution in the EVC process. Mathematical simulation shows that the static-friction zone plays an important role in the transient shear angle and the cutting force values in each cutting cycle.

- The predicted transient cutting force values are found to be in good agreement with the recorded experimental data in the orthogonal EVC tests conducted on 6061 aluminum alloy at four different speed ratios.

- The proposed analytical force model can express the EVC mechanism more finely, and assist to predict more accurate cutting force values, and is supposed to be helpful for researchers to proceed with further study on the EVC technique.

Chapter 5: Experimental and analytical studies of surface generation in EVC

As discussed in Chapter 2, it is already known that some of the characteristics of the EVC method are fundamentally different from the CC and CVC methods, which are considered to be main reasons for the superior performance of the EVC method. However, during the EVC process, vibration marks or cusps are formed on the machined surface profile along the nominal cutting direction. Such cusps, which are generated by the elliptical vibration trajectory and will increase the overall roughness of machined surface, are considered to be detrimental for achieving high-quality surface and a major disadvantage for EVC. In order to suppress the vibration marks and decrease the surface roughness, a very low nominal cutting speed needs to be employed to enhance the overlapping of the elliptical vibration locus, which can result in longer machining time and lower production efficiency.

Regarding the surface generation in the EVC process, Shamoto et al. proposed a method to predict the height of the vibration marks assuming a perfectly sharp tool edge, as described in Chapter 2. However, until now, very little research has been conducted to study the effects of machining and vibration parameters on surface generation. Furthermore, it is well known that the tool edge can never be perfectly sharp, and the tool edge radius usually ranges from tens of nanometers (e.g. SCD tool) to several microns (e.g. PCD tool, high-speed steel tool). As the vibration amplitudes of the EVC method are usually at micron-level, the effect of tool edge radius is

probably significant, especially for those non-SCD tools of which the edge radius is comparable to the vibration amplitudes.

Hence, in this chapter, in order to understand the surface generation process along nominal cutting direction, an experimental study comprising a series of grooving tests using a SCD tool with the EVC method is carried out firstly. The effects of nominal cutting speed on the surface generation at two different thrust-directional vibration amplitudes are investigated. Secondly, an analytical model for the surface generation along the nominal cutting direction is developed. Considering the geometrical relationship, the effect of tool edge radius on the surface generation is mathematically investigated. Finally, the proposed surface generation model is experimentally verified by conducting a series of grooving tests on soft and hard work materials using a PCD tool with the EVC method.

5.1 Experimental study using the SCD tool

5.1.1 Experimental setup

According to the theoretical analysis in Section 2.1.2, it can be noted that the theoretical roughness R_{th} is determined by the vibration parameters (a, b, ω and ϕ) and the nominal cutting speed (v_c). However, during a practical cutting test, the vibration parameters are preset before machining starts, and all these vibration parameters are usually kept constant during an individual machining test. Thus, in this study, the surface generation at different nominal cutting speeds is studied. Furthermore, as the thrust-directional amplitude b is directly proportional to R_{th} and plays an important factor (see Equation (2.17)), two different values of b are applied in the tests.

A series of grooving tests were conducted using an elliptical vibration device, which is attached to the tool-post of the 4-axis CNC ultraprecision machine. The vibrator vibrates at a frequency *f o*f 38.87 kHz, with a phase difference ϕ of 90^o. All the grooving test conditions under the EVC method are shown in Table 5.1. Six nominal cutting speeds ranging from 1 m/min to 6 m/min are applied, with the corresponding speed ratio ranging from 0.03 to 0.24. The workpiece is made of 6061 aluminum alloy, and a fresh SCD tool is set at the specific tool position of the vibrator with the nose radius of 0.6 mm and the rake, flank and approach angles of 0^o, 7^o and 30^o.

Table 5.1. Conditions of the grooving test

Vibration amplitude, [μm]	*a*	2					
	b	2			1		
Depth of cut, [μm]		5					
Nominal cutting speed, v_c, [m/min]		1	2	3	4	5	6
Speed ratio, R_s		0.03	0.07	0.10	0.13	0.17	0.24

5.1.2 Results and analysis

Figure 5.1 shows microscope photographs of the machined grooves at the six different nominal cutting speeds. It can be observed that, when the nominal cutting speed is less than or equal to 2 m/min, the vibration marks are insignificant and difficult to notice, and they become more and more obvious with the increase in the nominal cutting speed. The reason for such phenomenon lies in that the height of vibration marks gets increased with the increase in v_c, according to Equations (2.15) and (2.17).

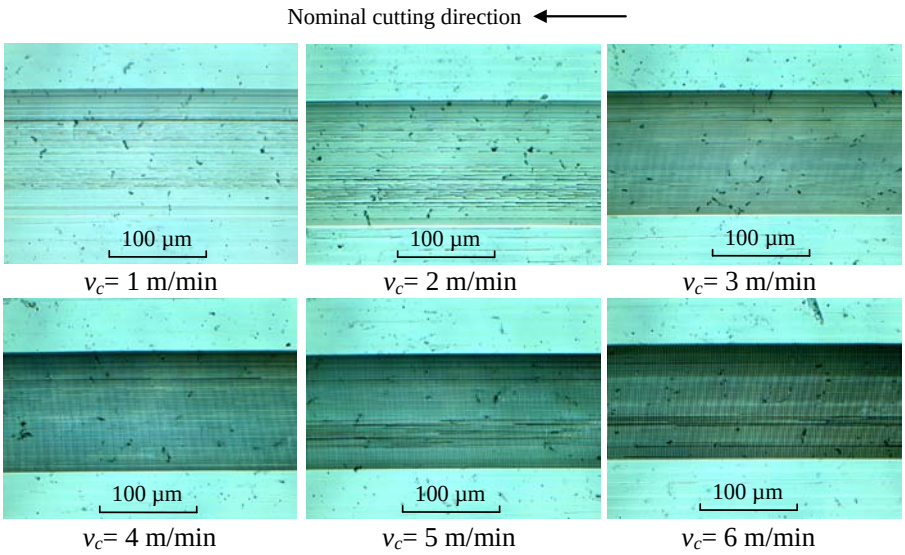

Figure 5.1. Microscope photographs (×1000) of the grooves with different nominal cutting speeds under the EVC method. Condition: b= 2 µm.

The contour image of the bottom surface of each groove is captured by a white light interferometer, and the experimental roughness (symbolized as R_{ex}) along the nominal cutting direction is accordingly measured and calculated. Figure 5.2 shows an example of the surface analysis by utilizing the white light interferometer. The value of R_{ex} is calculated by averaging the peak-to-valley depth of each vibration mark along the nominal cutting direction (see Figure 5.2(b)).

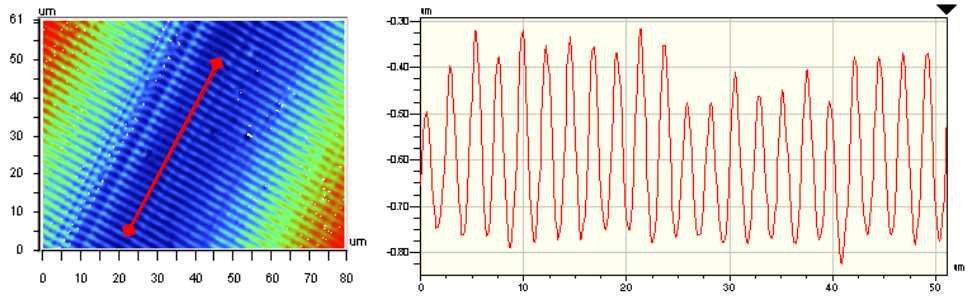

(a) (b)

Figure 5.2. Example of surface analysis by a white light interferometer. (a) Contour image of the groove bottom, (b) Surface profile along the nominal cutting direction. Conditions: v_c= 6 m/min, b= 2 μm.

With the known vibration and machining parameters (a, b, ω, ϕ, and v_c), the theoretical roughness value at the six different nominal cutting speeds can be calculated based on Equations (2.15) and (2.17). Figure 5.3 shows the comparison results between R_{ex} and R_{th} at the two different thrust-directional amplitudes. It should be noted that the vertical scale of Figure 5.3(a) is two times that of Figure 5.3(b), due to the proportional relationship between b and R_{th} (see Equation (2.17)). From Figure 5.3(a), it can be seen that R_{ex} starts to be detectable and becomes a significant value, as v_c is set larger than 2 m/min at 2 μm thrust-directional amplitude. In Figure 5.3(b), a similar critical v_c is found to be 3 m/min at 1 μm thrust-directional amplitude. As v_c is smaller than or equal to 2 m/min or 3 m/min, the value of R_{ex} is quite small, typically less than 10 nm. The reason for such phenomenon may lie in the non-zero edge radius of the SCD tool, which has not been considered in the roughness model stated earlier. Although an SCD tool usually has an edge radius of submicron level (ranging from tens to hundreds of nanometers), it is still relatively large when considering the feature generation of submicron or even nanometer level. Due to the

round tool edge, the round tool edge may punch the vibration mark left by the previous vibration cycle into the workpiece. Such action could lower the height of cusps, and eventually cause the experimental roughness to be smaller than the theoretical one, which is calculated based on an assumption of perfectly sharp tool edge. Based on this observation, it is suggested that, when applying the EVC method, the nominal cutting speed can be set lower than a critical v_c to avoid adverse effect of the vibration marks on the overall surface roughness of machined workpiece.

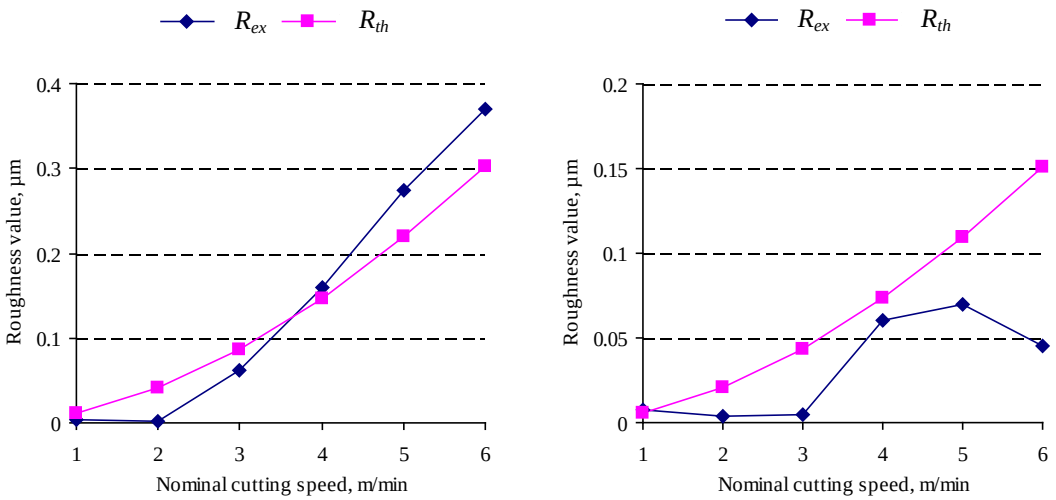

(a) (b)

Figure 5.3. Experimental and predicted roughness values along nominal cutting direction with different nominal cutting speeds. Conditions: (a) b= 2 µm, (b) b= 1 µm.

At the 1 µm thrust-directional amplitude (see Figure 5.3(b)), when v_c is larger than 3 m/min, the experimental roughness values are smaller than the theoretical ones, and the value of R_{ex} even decreases with the increase of v_c. The reason for this phenomenon may lie in the interface between the tool flank face and the generated

vibration marks, which has not been considered in the roughness model as stated in Section 2.1.2.

5.2 Development of the surface generation model considering tool edge radius

It is well known that, during precision or micro machining process, the surface generation mechanism is considered to be significantly affected by the tool microgeometry parameters (Liu et al., 2007) (e.g. the tool edge radius). During the EVC process, since the vibration amplitudes of the EVC method are usually at micron-level (Brehl and Dow, 2008), the tool edge dimension of most kinds of tools (except the SCD tool) is usually comparable to the vibration amplitudes and hence has significant effect on the surface generation mechanism. Therefore, the tool edge dimension must be considered while predicting the surface roughness for the EVC process.

The geometry of a cutting tool is defined by several tool parameters, such as nose radius, rake angle, clearance angle λ and edge radius r_e. In this study, the tool edge is assumed to be round, and the cross-section of the cutting tool can be schematically illustrated with a basic geometry as shown in Figure 5.4. The points T_o and T_b represent the center of the tool edge circle and the bottom point of tool edge, respectively.

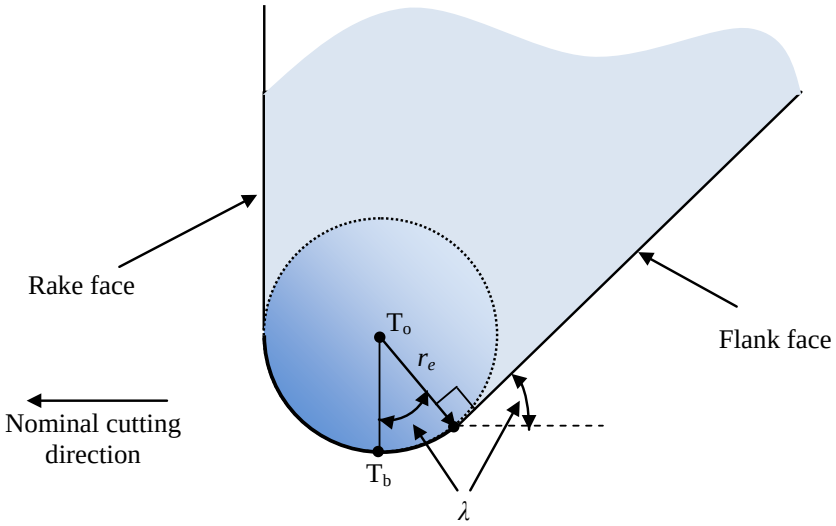

Figure 5.4. Schematic cross-section view of tool geometry.

For a tool with a round tool edge, the surface generation point T (i.e. the point where the tool edge contacts the finished surface profile) continuously varies along the round tool edge during each EVC cycle. Figure 5.5 shows the surface generation process using the round edge tool applying the EVC method. The dash line curve A-B-C in Figure 5.5 represents the vibration trajectory of the bottom point T_b of the round tool edge (see Figure 5.4). According to the nature of surface generation mechanism, it can be found that at any location where the machined surface is generated, the tool edge circle will be always tangent to the generated surface profile. It means that the finished surface profile is actually generated by an envelope line of the round tool edge, which eventually results in a solid curve A_e-B_e-C_e, as shown in Figure 5.5. The points A_e and C_e represent cross-over points for the two consecutive envelope lines of the round tool edge. The point B_e represents the bottom point of the theoretically machined surface considering the round tool edge and has the same coordinate value with the bottom point B of the elliptical vibration trajectory (see

Figure 2.3). Thus, from Figure 5.5, the theoretical roughness considering tool edge radius can be derived from the following equation:

$$R_{the} = y_{Ae} - y_b \tag{5.1}$$

where y_{Ae} and y_b are the y-axis coordinates of A_e (x_{Ae}, y_{Ae}) and B (x_b, y_b), respectively.

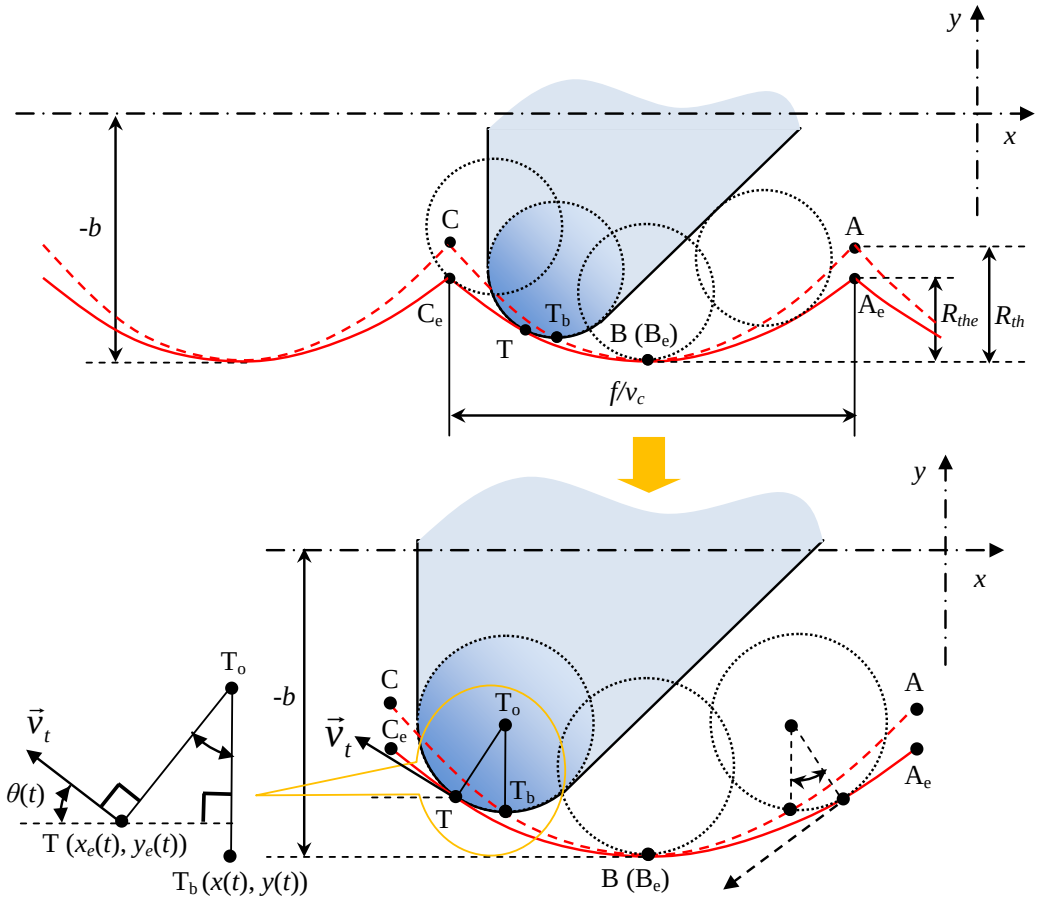

Figure 5.5. Illustration of the surface generation for the EVC process considering the round tool edge.

Based on the geometrical relationship in Figure 5.5, the point T_b on the cutting tool is set as reference coordinates. The tool velocity $\vec{v}_t$ is tangent to the round tool

edge, which is perpendicular to the radial line T_oT of the edge circle, as shown in Figure 5.5. Then, it can be derived that the angle $\angle TT_oT_b$ is equal to the transient tool velocity angle $\theta(t)$. Hence, the coordinates of the transient surface generation point T ($x_e(t), y_e(t)$) on the curve A_e-B_e-C_e can be calculated based on the relative position between T and T_b:

$$\begin{cases} x_e(t) = x(t) - r_e \sin\theta(t) \\ y_e(t) = y(t) + r_e(1-\cos\theta(t)) \end{cases}$$

$$\Rightarrow \begin{cases} x_e(t) = a\cos(\omega t) - v_c t - r_e \sin\theta(t) \\ y_e(t) = b\cos(\omega t + \phi) + r_e(1-\cos\theta(t)) \end{cases} \quad (5.2)$$

If t_{Ae} and t_{Ce} are used to represent the time instants when the surface generation point T passes the cross-over points A_e ($x_e(t_{Ae}), y_e(t_{Ae})$) and C_e ($x_e(t_{Ce}), y_e(t_{Ce})$), by substituting Equation (5.2) into Equation (5.1), the following equation can be derived:

$$R_{the} = y_e(t_{Ae}) - (-b)$$

$$\Rightarrow R_{the} = b\cos(\omega t_{Ae} + \phi) + r_e(1-\cos\theta(t_{Ae})) + b \quad (5.3)$$

It can be noticed from the Equation (5.3) that the theoretical roughness value can be determined, if the value of t_{Ae} is obtained. As the pitch of the regular wave is equal to the distance which is given by the total relative movement of the tool and the workpiece in the cutting direction from t_{Ae} to t_{Ce}, the following equation can be derived:

$$x_e(t_{Ae}) - x_e(t_{Ce}) = 2\pi v_c / \omega \quad (5.4)$$

In addition, it is also understood that the vertical positions of the crossover points A_e and C_e are equal. Hence,

$$y_e(t_{Ae}) - y_e(t_{Ce}) = 0 \tag{5.5}$$

By substituting Equation (5.2) into Equations (5.4) and (5.5), the following equation set can be derived:

$$\begin{cases} a\cos(\omega t_{Ae}) - v_c t_{Ae} - r_e \sin\theta(t_{Ae}) - a\cos(\omega t_{Ce}) - v_c t_{Ce} - r_e \sin\theta(t_{Ce}) = 2\pi v_c / \omega \\ b\cos(\omega t_{Ae} + \phi) + r_e(1 - \cos\theta(t_{Ae})) - b\cos(\omega t_{Ce} + \phi) + r_e(1 - \cos\theta(t_{Ce})) = 0 \end{cases} \tag{5.6}$$

In order to solve the above equation set, Equation (5.6) needs to be refined into an equation set with two variables t_{Ae} and t_{Ce}. According to Equations (2.10) and (2.11), $\sin\theta(t)$ and $\cos\theta(t)$ can be derived from the following equations:

$$\begin{cases} \sin\theta(t) = \dfrac{y'(t)}{\sqrt{x'(t)^2 + y'(t)^2}} \\ \cos\theta(t) = \dfrac{-x'(t)}{\sqrt{x'(t)^2 + y'(t)^2}} \end{cases}$$

$$\Rightarrow \begin{cases} \sin\theta(t) = \dfrac{-\omega b \sin(\omega t + \phi)}{\sqrt{(\omega a \sin(\omega t) + v_c)^2 + (\omega b \sin(\omega t + \phi))^2}} \\ \cos\theta(t) = \dfrac{\omega a \sin(\omega t) + v_c}{\sqrt{(\omega a \sin(\omega t) + v_c)^2 + (\omega b \sin(\omega t + \phi))^2}} \end{cases} \tag{5.7}$$

Finally, by substituting Equation (5.7) into Equation (5.6), a nonlinear equation set can be derived as follows:

$$\begin{cases} a(\cos\omega t_{Ae} - \cos\omega t_{Ce}) + v_c(t_{Ce} - t_{Ae} - \dfrac{2\pi}{\omega}) + r_e\omega b(\dfrac{-\sin(\omega t_{Ce} + \phi)}{\sqrt{(\omega a\sin(\omega t_{Ce}) + v_c)^2 + (\omega b\sin(\omega t_{Ce} + \phi))^2}} \\ + \dfrac{\sin(\omega t_{Ae} + \phi)}{\sqrt{(\omega a\sin(\omega t_{Ae}) + v_c)^2 + (\omega b\sin(\omega t_{Ae} + \phi))^2}}) = 0 \\ b(\cos(\omega t_{Ae} + \phi) - \cos(\omega t_{Ce} + \phi)) + r_e\omega a(\dfrac{\sin(\omega t_{Ce}) + v_c}{\sqrt{(\omega a\sin(\omega t_{Ce}) + v_c)^2 + (\omega b\sin(\omega t_{Ce} + \phi))^2}} \\ - \dfrac{\sin(\omega t_{Ae}) + v_c}{\sqrt{(\omega a\sin(\omega t_{Ae}) + v_c)^2 + (\omega b\sin(\omega t_{Ae} + \phi))^2}}) = 0 \end{cases}$$

(5.8)

Then, the values of t_{Ae} and t_{Ce} can be calculated by solving the above nonlinear equation set using the MATLAB software, and a flow chart of the proposed calculation method for predicting the surface roughness considering tool edge radius is shown in Figure 5.6.

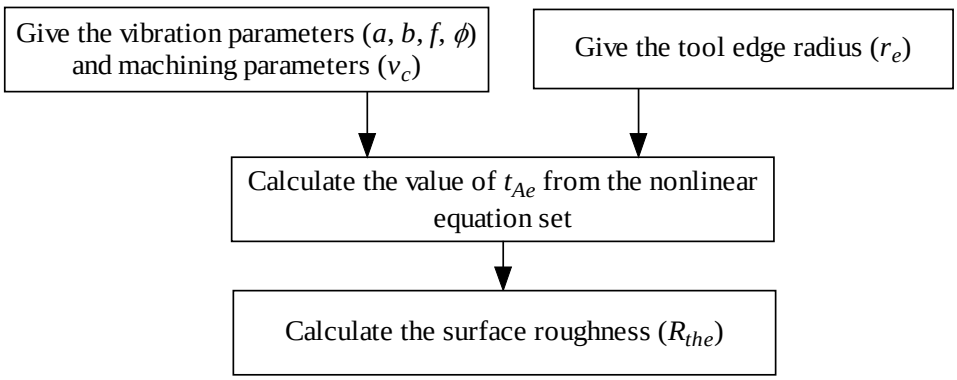

Figure 5.6. Flow chart for calculating the analytical surface considering tool edge radius.

In order to mathematically evaluate the effect of tool edge radius, simulation with three different edge radii (0, 1 and 3 μm) is conducted with 2 μm vibration amplitudes (i.e. a=b=2 μm) and 38.87 kHz vibration frequency. Figure 5.7(a) shows the finished surface profiles along the nominal cutting direction with three different edge radii. The relationship between the theoretical roughness R_{the} and the tool edge radius r_e is

shown in Figure 5.7(b). It can be observed that R_{the} decreases gradually with the increase of r_e. The theoretically rough finished surface profile is generated by the perfectly-sharp tool. It can also be foreseen that, without considering the effect of elastic recovery and material side flow, if the tool edge radius becomes infinitely large, the theoretical roughness R_{the} will approach to be zero.

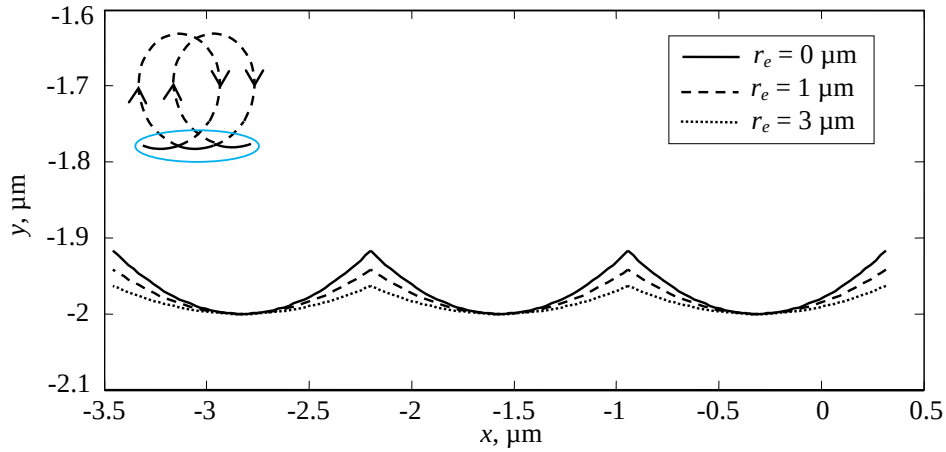

(a)

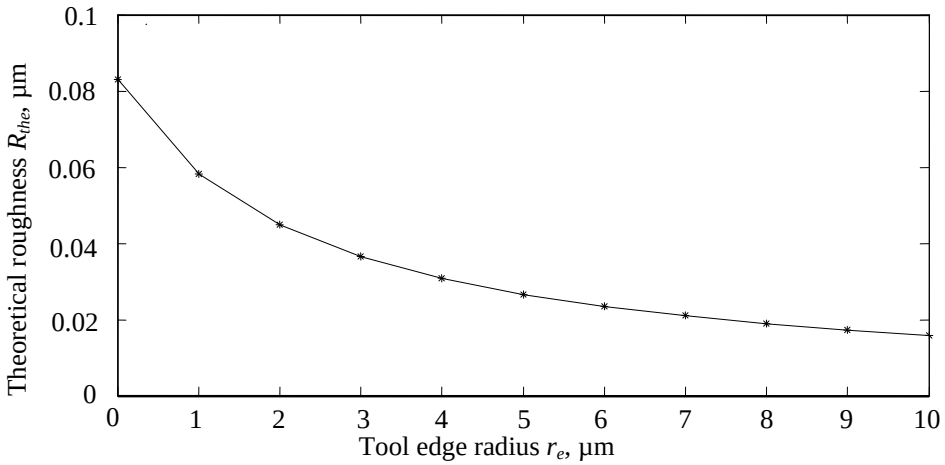

(b)

Figure 5.7. (a) Simulated surface profiles along the nominal cutting direction considering tool edge radius for the EVC process, (b) Theoretical roughness versus tool edge radius. Conditions: 3 m/min nominal cutting speed; circular vibration with 2 µm amplitude; 38.87 kHz vibration frequency.

5.3 Experimental verification

In order to experimentally validate the proposed analytical surface generation model considering the effect of tool edge radius for the EVC process, a series of grooving tests are conducted applying the ultrasonic EVC method.

5.3.1 Experimental design

A series of grooving tests are conducted by changing the nominal cutting speed between 3 and 6 m/min, keeping the vibration parameters (a, b, f, ϕ) and the tool edge radius (r_e) constant during the EVC process. An ultrasonic elliptical vibration device is used in the grooving tests and attached to the tool-post of a CNC ultraprecision machine (*Toshiba ULG-100H*[3]), as shown in Figure 5.8. Two work materials, 6061 aluminum alloy and hardened stainless steel (49 HRC), are used in this experiment. All the grooving test conditions with the EVC method are shown in Table 5.2.

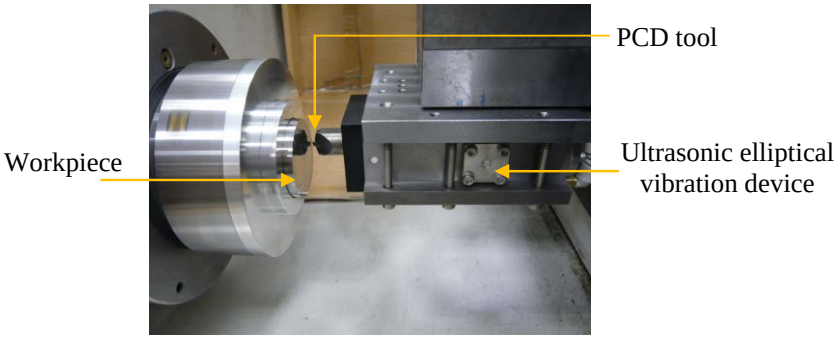

Figure 5.8. Experimental setup with the elliptical vibrator.

Table 5.2. Conditions of the grooving test using the EVC method.

Work material		Aluminum alloy, Hardened steel (49 HRC)			
Vibration amplitude, [μm]	*a*	2			
	b	2			
Phase shift, ϕ [deg]		90			
Vibration frequency, *f* [kHz]		38.87			
Depth of cut, a_p [μm]		5			
Nominal cutting speed, v_c [m/min]		3	4	5	6
Speed ratio, R_s		0.10	0.13	0.17	0.24

A triangular-type fresh PCD tool (0.6 mm nose radius) with the rake, relief and approach angles of 0^o, 11^o and 30^o, respectively, is set at the specific tool position of the vibrator (see Figure 5.8) for each set of the cutting conditions. The edge radius of the PCD tool is found to be about 3 μm by applying an indentation method. The indentation is conducted on a workpiece made of copper, which is then placed in an atomic force microscope (AFM) for measurement. Figure 5.9 shows the indentation profile formed by the PCD tool edge, and the edge radius measured from the AFM profile r_{em} is found to be about 4.5 μm. With the elastic error compensation coefficient f_{sb} calibrated as 1.5 (Li et al., 2003), the actual tool edge radius can be calculated to be about 3 μm from the following equation:

$$r_e = \frac{r_{em}}{f_{sb}} \tag{5.9}$$

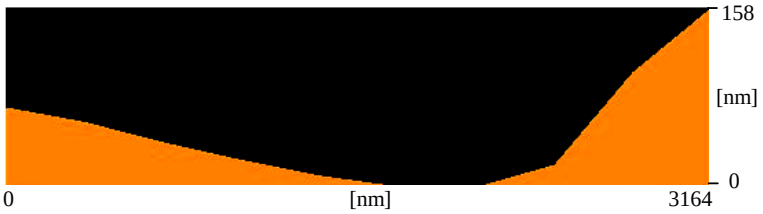

Figure 5.9. AFM analysis of the PCD tool edge indentation.

5.3.2 Experimental results

Figure 5.10(a) and (b) show the microscope photographs of the machined grooves at 6 m/min nominal cutting speed on the workpieces made of aluminum alloy and hardened steel.

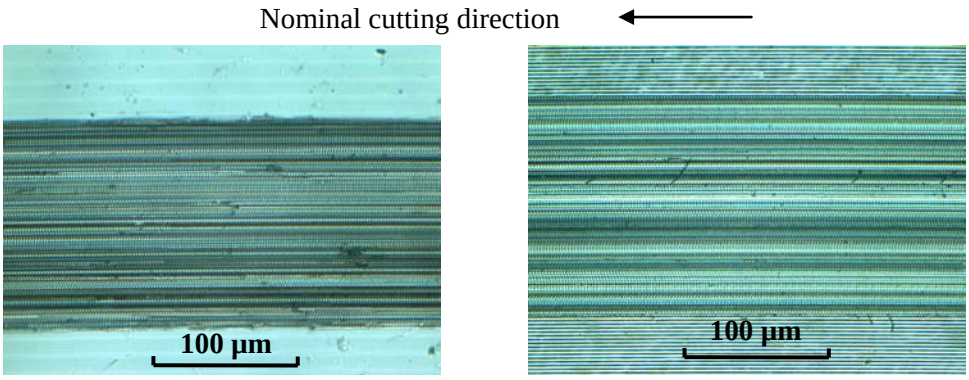

(a) (b)

Figure 5.10. Microscope photographs (×1000) of the machined grooves under the EVC method on the workpieces made of: (a) Aluminum alloy, (b) Hardened steel.

The experimental roughness R_{ex} under the test conditions is measured using a white light interferometer, and the value is calculated by averaging the peak-to-valley depth of each vibration mark along the nominal cutting direction. Figure 5.11 shows

the surface roughness measurement of the aluminum alloy groove using the white light interferometer at 6 m/min nominal cutting speed.

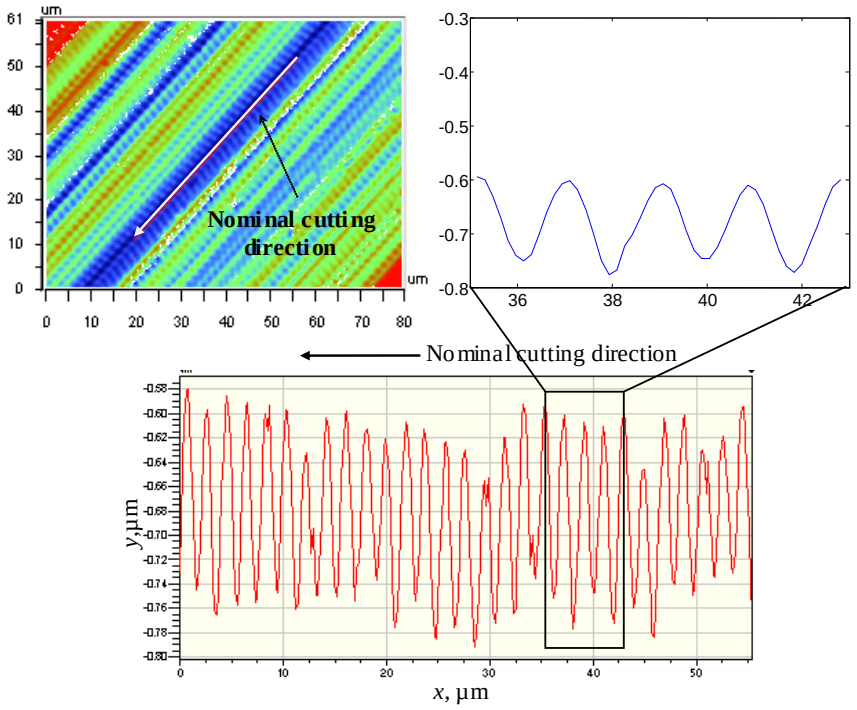

Figure 5.11. Surface roughness measurement using the white light interferometer. Condition: 6 m/min nominal cutting speed.

Given the vibration and machining parameters (a, b, f, ϕ and v_c), the theoretical roughness considering the edge radius can be calculated using Equations (5.3) and (5.8). Figure 5.12 shows a comparison between the predicted roughness along the nominal cutting direction and the experimentally measured roughness (R_{ex}) on the aluminum alloy and hardened steel workpieces. As shown in Figure 5.12, both the predicted and experimental roughness increases gradually with the increment of nominal cutting speed. It is because that, with the increase of cutting speed, the elliptical vibration locus becomes less overlapping along the nominal cutting direction, and the height of vibration marks will increase.

It can be seen from Figure 5.12 that R_{the} considering the edge radius (r_e=3 μm) corresponds well with the experimentally measured roughness R_{ex}, which demonstrates that the proposed surface generation model performs well in predicting the roughness along the nominal cutting direction in the EVC process. Meanwhile, it can also be seen that the predicted roughness R_{th} without considering the edge radius (r_e=0 μm) is significantly larger than R_{ex} of both materials at all the nominal cutting speeds. Such discrepancy is caused by the overlook of the round tool edge, which can lower the height of the vibration marks compared to a perfectly-sharp cutting tool.

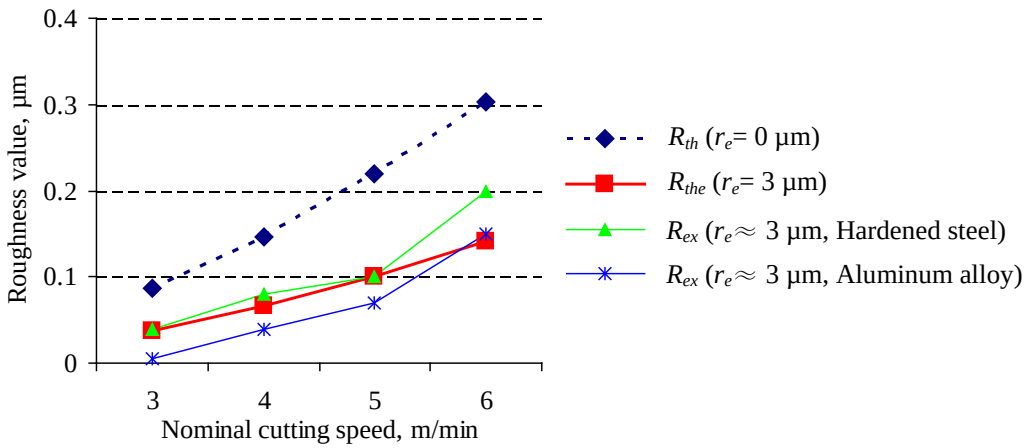

Figure 5.12. Experimental and predicted roughness along nominal cutting direction with different nominal cutting speeds.

It is known that, in conventional micromachining, minimum uncut chip thickness is important when predicting the surface roughness due to the size effect (Liu et al., 2007). However, in elliptical-vibration-assisted micromachining, periodic motion of the tool exists along the thrust direction in each EVC cycle (see Figure 2.2). Such unique movement will help the uncut material to realize plastic deformation and assist the chip to flow away from the workpiece surface. This fact will mitigate the effect of

minimum chip thickness and make it insignificant and negligible in the EVC process. Therefore, the pure geometrical model can evaluate the surface roughness well, even without considering the minimum chip thickness.

5.4 Concluding remarks

An experimental study comprising a series of grooving tests using an SCD tool is carried out to deeply understand the surface generation process along nominal cutting direction under the EVC method, and a comprehensive surface generation model for the EVC method has been developed for in-depth understanding of the effect of tool edge radius on predicting the surface roughness along nominal cutting direction. The following conclusions can be drawn based on this study:

- There exists a critical nominal cutting speed for different thrust amplitudes, below which the experimental roughness is quite small and the vibration marks are almost undetectable.

- Mathematical evaluation reveals that the tool edge radius should not be overlooked for more accurate roughness prediction along the nominal cutting direction. The simulation results show that the theoretical roughness decreases with the increase of the tool edge radius. It is because that the height of the vibration marks generated by a tool with a larger edge radius is smaller than that generated by a tool with a smaller edge radius.

- The predicted roughness along the nominal cutting direction based on the proposed model is found to be in significantly better agreement with the measured experimental roughness of both materials than the predicted values without considering tool edge radius.

Chapter 6: Ultrasonic EVC of hardened stainless steel using PCD tools

Hardened steel has been widely used in die and mold parts for producing mainly plastic lenses. Hence, direct machining of the hardened steel, which is cost-effective, to obtain high-quality surface is always a concern of industries. Instead of grinding and polishing, direct ultraprecision machining of this material would save considerable machining time and cost. However, steel becomes more brittle and less ductile after it is hardened, making the workpiece difficult to cut using the CC method. It is known that SCD tools have been widely used to cut non-ferrous materials to achieve high-quality mirror surface in ultraprecision engineering due to their high hardness, long tool life and low thermal conductivity. However, directly machining of steel using the CC method is impossible, due to the excessive tool wear caused by the strong chemical affinity between carbon and iron atoms.

As described in Chapter 2, Moriwaki et al. have justified the feasibility of achieving optical quality mirror surface by applying the CVC method using SCD tools (Moriwaki and Shamoto, 1991). EVC has been proved to be a promising method in terms of almost all cutting performances compared to the CC and CVC methods in cutting and grooving of hardened steel. Shamoto et al. have used SCD tools to machine hardened steel by applying the EVC method, and found extremely smaller cutting force and much longer tool life compared to the CC and CVC methods. As an inexpensive artificial diamond tool compared to SCD, PCD has been proved as a

promising and cost-effective tool material. Zhou et al. have applied the CVC method in cutting stainless steel using PCD tools and observed lower cutting forces and less tool wear compared to the CC method (2003). However, mirror quality surface is not achieved in their study, and the inexpensive PCD tools have not yet been applied on hardened steel using the EVC method.

The aim of this chapter is to justify the application feasibility of PCD tools using the EVC method to obtain mirror quality surface on hardened steel for die and mold applications. Face turning experiments on about 550 mm^2 area are conducted on a hardened steel workpiece (a typical Stavax with 49 HRC) under conventional machining parameters including nominal DOC, feed rate and nominal cutting speed. The effects of these parameters on output performances such as cutting force, tool flank wear, chip formation and surface roughness are investigated and analyzed. Later, based on understandings of these effects, a separate test of machining about 1257 mm^2 is carried out to observe the life of standard PCD tools and the quality of surface.

6.1 Experimental setup and procedures

Experimental setup of the EVC test is shown in Figure 6.1. These tests are conducted using an elliptical vibrator device, which is attached to the tool-post of a CNC ultraprecision machine. A triangular-type fresh PCD tool (grade DA150) with the rake, relief and approach angles of 0^o, 11^o and 30^o, respectively, is set at the specific tool position of the vibrator for each set of cutting conditions. The nose radius of the tools is chosen as 0.6 mm because the authors have previously demonstrated that this geometry performs better compared to other smaller and larger nose radii while machining sintered tungsten carbide using the EVC method (Nath et al., 2009b).

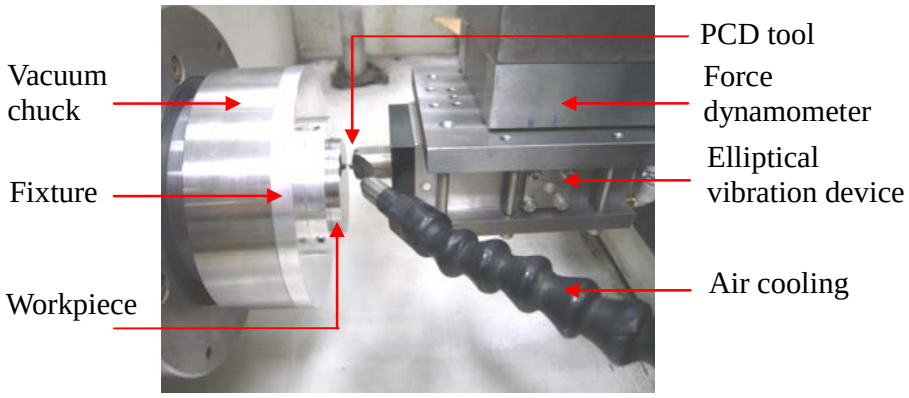

Figure 6.1. Experimental setup with the elliptical vibrator on the ultraprecision machine for the EVC test.

Table 6.1 Workpiece material composition

	Compositions [%]				
Types	C	Si	Cr	Mn	V
Stavax	0.38	0.9	13.6	0.5	0.3

In the experimental setup, a hardened steel workpiece made of typical Stavax with 49 HRC hardness (i.e. 490 HV), is held by the vacuum chuck attached on the air spindle of the CNC machine, as shown in Figure 6.1. The chemical composition of the workpiece material is shown in Table 6.1. In each face turning test, the tool is set to move towards the center of the workpiece from the outer diameter (OD, 40 mm) to the inner diameter (ID, 30 mm) for machining a surface area of about 550 mm^2. A schematic view of the machining area in the EVC test is illustrated in Figure 6.2. The vibrator vibrates at a frequency f of 38.87 kHz and a phase difference ϕ of 90^o, and the peak-to-peak amplitude of elliptical vibration is set at 4 µm in the tangential and the thrust directional directions (a= b = 2 µm). Hence, four different nominal DOCs

of 2, 4, 6 and 10 µm are chosen. During the face turning, the nominal cutting speed decreases while the tool moves towards the centre due to the traverse feed:

$$v_c=2\pi r n_r/60 \quad (6.1)$$

where n_r is the spindle rotational speed, r is the radial distance from the workpiece center. Earlier, Nath et al. have theoretically and experimentally demonstrated that a significantly reduced value of the maximum thickness of cut could be achieved when the speed ratio is set lower than the critical speed ratio of 0.12837 (Nath et al., 2011). Hence three different speed ratios, where two values are smaller and larger than 0.12837 and the other value is approximately equal to 0.12837, are chosen by varying the spindle speed. Then at a fixed nominal DOC and a fixed spindle speed, four different feed rates of 10, 7.5, 5 and 2.5 µm/rev are chosen to observe their effects on the cutting performance of hardened stainless steel using PCD tools. The corresponding cutting lengths at various feed rates ($L_c=\pi(D^2-d^2)/(4f_r)$, where D and d represent the outer and inner diameters, respectively) are also shown in Table 6.2. Finally, to evaluate the capability of commercial PCD tools for machining mirror quality surface on hardened steel using the EVC method, a face turning test with 10 µm nominal DOC, 2.5 µm/rev feed rate and 15 rpm spindle speed is conducted on the entire workpiece surface. All the EVC test conditions in this study, exclusive of the separate evaluation test condition, are shown in Table 6.2.

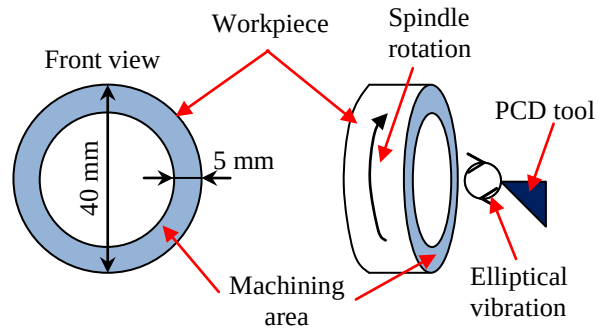

(a)

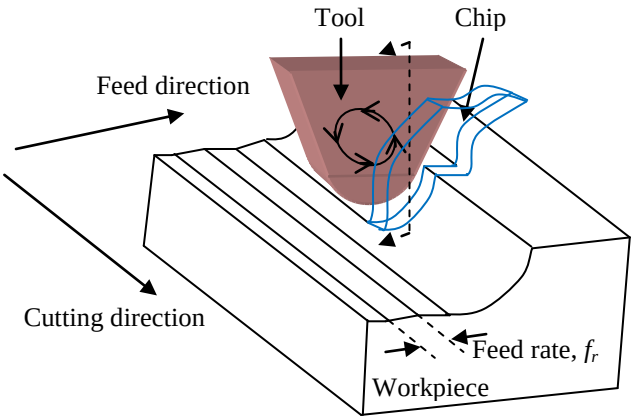

(b)

Figure 6.2. Schematic illustration of: (a) machining area, (b) 3D view of the turning process.

Table 6.2 The EVC test conditions used during face turning

DOC, [µm]		2, 4, 6, 10			
Feed rate, f_r [µm/rev]		2.5	5	7.5	10
Cutting length, L_c [m]		220	110	73	55
Cutting area, [mm^2]		550			
Spindle speed, n_r [rpm]		15	30	45	
Nominal cutting speed, [m/min]	$(v_c)_{max}$ at OD	1.885	3.634	5.655	
	$(v_c)_{min}$ at ID	1.414	2.827	4.241	
Speed ratio at OD, $(v_c)_{max}/(v_t)_{max}$		0.0643	0.1286	0.1930	
Coolant		Air			

In order to measure the cutting force components in the experimental tests, a 3-component mini-dynamometer which has a 1 mN resolution is attached to the elliptical vibrator, as shown in Figure 6.1. Amplified force signal is captured using a real-time recorder. Furthermore, a Nomarski microscope is used to capture all the photographs of the flank faces of PCD tools and the machined surfaces. The surface roughness is measured along the feed or traverse direction of the workpiece with a 4.5 mm scan length and a 0.25 mm cut-off value using a stylus profilometer (*Mitutoyo CS-5000*), of which the stylus tip radius is 5 μm. Finally, the chip formation are analyzed by a scanning electron microscope (SEM), while an atomic force microscope (AFM) and a white light interferometer (*Zygo NewView 5000*) are also employed to analyze the surface profile of the finished surface.

6.2 Results and analysis

6.2.1 Effects of cutting parameters on force components

Figure 6.3(a)-(c) sequentially shows the effects of three machining parameters on two major force components, namely, tangential force and thrust force. The value of feed force along the feed direction is relatively negligible compared to the other two force components, and hence is not included in Figure 6.3. It can be observed that the thrust force is always larger than the tangential force in all the cases. It may be due to two following reasons. The first reason is that the uncut chip thickness is very small in comparison with the edge radius (about 3 μm) of PCD tools. Such size of edge radius can cause highly negative effective rake angle, which eventually results in high ploughing force. The other reason is that the tool edge punches the vibration marks

into the workpiece at the start of each cutting cycle (see Figure 2.2). Such punching action can result in high pressure on the cutting tool in the thrust direction.

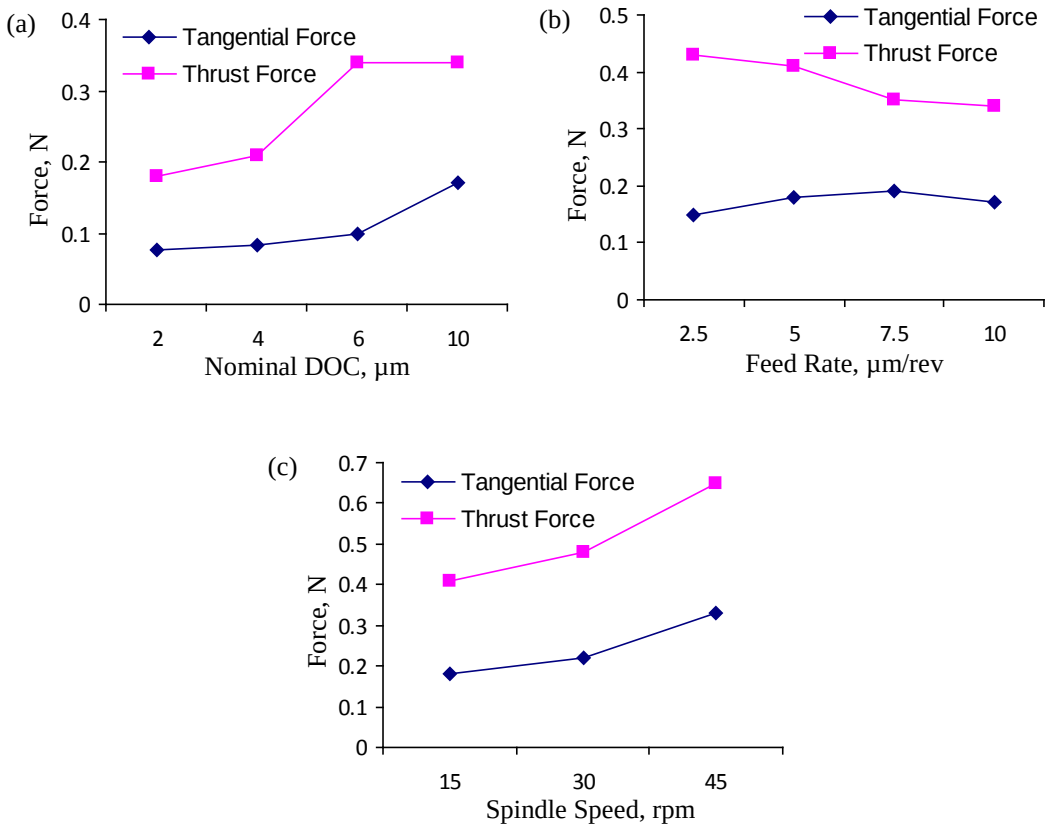

Figure 6.3. Effects of machining parameters on cutting force components: (a) nominal DOC (n_r = 15 rpm, f_r = 10 µm/rev), (b) feed rate (n_r = 15 rpm, DOC = 10 µm), (c) nominal cutting speed (f_r = 5 µm/rev, DOC = 10 µm).

Figure 6.3(a) shows that the tangential and the thrust force increases with the increase in nominal DOC in the EVC process, similar to the observation in the CC process, due to increased pressure on the tool rake face. In Figure 6.3(b), the tangential force increases slightly with the increase in feed rate, like the variation trend in the CC method. However, with the decrease in feed rate, the thrust force gradually increases instead, when the feed rate is below 10 µm/rev. Such phenomenon

is deemed to be caused by the decrease in uncut chip thickness induced by the decrement in feed rate. Due to the small uncut chip thickness, the highly negative effective rake angle, rather than the nominal rake angle tends to determine the resulting force at these smaller feed rates. Hence, more significant ploughing action can be caused by the highly negative effective rake angle which is induced by smaller uncut chip thickness, as demonstrated by previous researchers (Lucca et al., 1993). It can also be noticed in Figure 6.3(c) that both the tangential and the thrust force components decrease with the decrease in spindle speed (or nominal cutting speed). Such results correspond well with those found in the low-frequency EVC tests, as shown in Figure 3.9.

6.2.2 Effects of cutting parameters on tool wear

Tool wear has strong influence on surface finish and dimensional accuracy of a machined workpiece, and is also directly related to the machining cost and efficiency. The photographs of flank faces of the PCD tools, and their close-up views were captured by the Nomarski microscope. Figure 6.4 shows five selected photographs to observe the effects of different nominal rotational speeds (see Figure 6.4(a)-(c)), nominal DOCs (see Figure 6.4(c)-(d)) and feed rates (see Figure 6.4(d)-(e)). The cutting length which varies with different feed rates for the five conditions can be found in Table 6.2. It can be observed that the flank wear of almost all the used PCD tools against the machining parameters is insignificant (less than 8 μm), except the one with the higher spindle speed (45 rpm), as shown in Figure 6.4(a). Its flank wear width is found to be about 14 μm at 110 m cutting length. Figure 6.4(b)-(e) show the flank faces of two PCD tools under four different cutting conditions with two relatively lower spindle speeds (30 rpm and 15 rpm), and their tool flank wear is

much smaller than that in Figure 6.4(a). Hence it can be remarked that different machining parameters, except the nominal cutting speed, do not have strong influence on tool wear when machining hardened steel using PCD tools, and the PCD tool life will become shorter with the increase in nominal cutting speed or speed ratio. The main reason lies in that the higher speed ratio induces relatively larger portion where the tool is in contact with the workpiece in each cutting cycle. The higher the speed ratio, the more similar the EVC process is to the CC process, making the degree of tool wear suppression in EVC weakened.

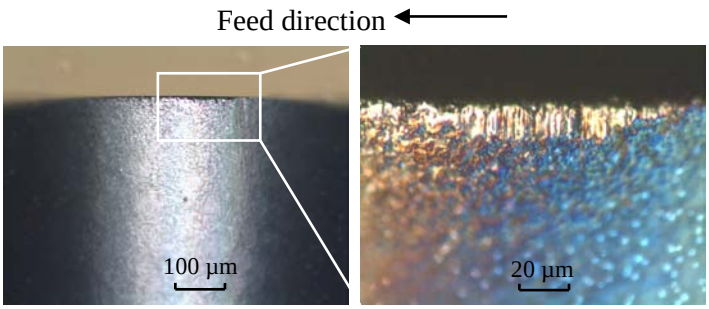

(a)

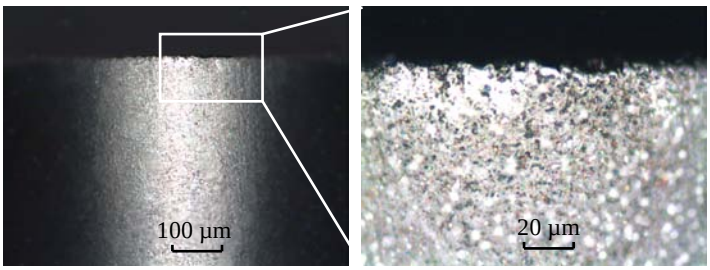

(b)

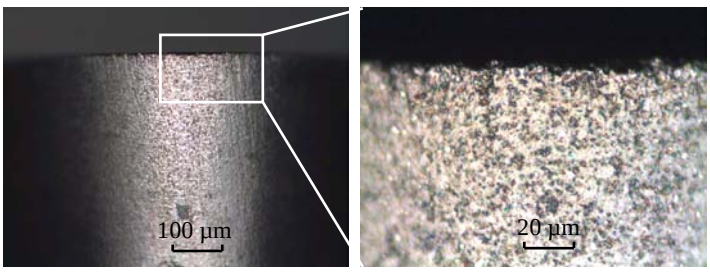

(c)

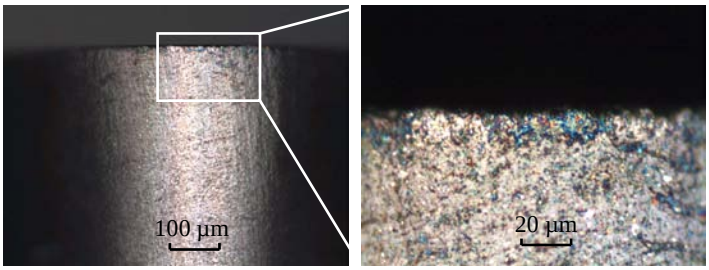

(d)

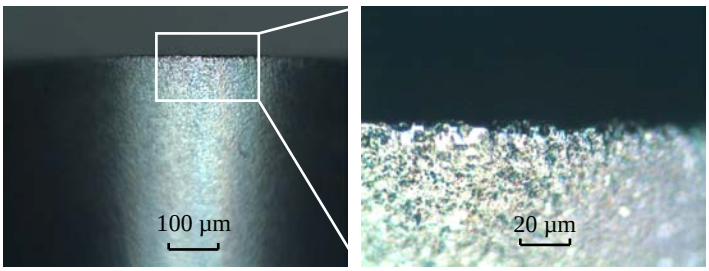

(e)

Figure 6.4. Microscope (100× and 500 ×) photographs of the flank wear of PCD tools: (a) DOC = 10 µm, f_r = 5 µm/rev, n_r = 45 rpm, L_c= 110 m, (b) DOC = 10 µm, f_r = 5 µm/rev, n_r = 30 rpm, L_c= 110 m, (c) DOC = 4 µm, f_r = 10 µm/rev, n_r = 15 rpm, L_c= 55 m, (d) DOC = 10 µm, f_r = 10 µm/rev, n_r = 15 rpm, L_c= 55 m, (e) DOC = 10 µm, f_r = 7.5 µm/rev, n_r = 15 rpm, L_c= 73 m.

6.2.3 Effects of cutting parameters on chip formation

The chips generated with the EVC method using PCD tools are collected and analyzed by using the SEM. Four photographs of these chips observed at various cutting conditions are shown in Figure 6.5. It can be seen that the chip thickness is observed to be constant in each cutting condition. Furthermore, the formed chips are found to be continuous in most of the cases (see Figure 6.5(b)-(d)), meaning that continuous chip formation process is achieved with the spindle speed of 15 rpm and 30 rpm, while the chips with the 45 rpm spindle speed are non-continuous. The reason for this phenomenon may lie in that the higher nominal cutting speed or speed ratio in

the EVC method results in the larger cutting force (see Figure 6.3(c)) and the faster tool wear (see Figure 6.4(a)), which can consequently induce less stable cutting process and hence more breakable chips.

It is also interesting to find from Figure 6.5(a)-(c) that the chip width increases with the increase in nominal cutting speed or speed ratio. Two reasons can be realized with this observation. One reason is that the chip formation process may be affected by the larger cutting force (see Figure 6.3(c)) resulting from the higher nominal cutting speed. The larger cutting force may cause more significant lateral side flow of material, which can consequently increase the width of chip. Another reason is that, as stated in Chapter 3, transient TOC is increased with the increment of speed ratio (see Figure 3.10), which may lead to a comparatively larger chip size.

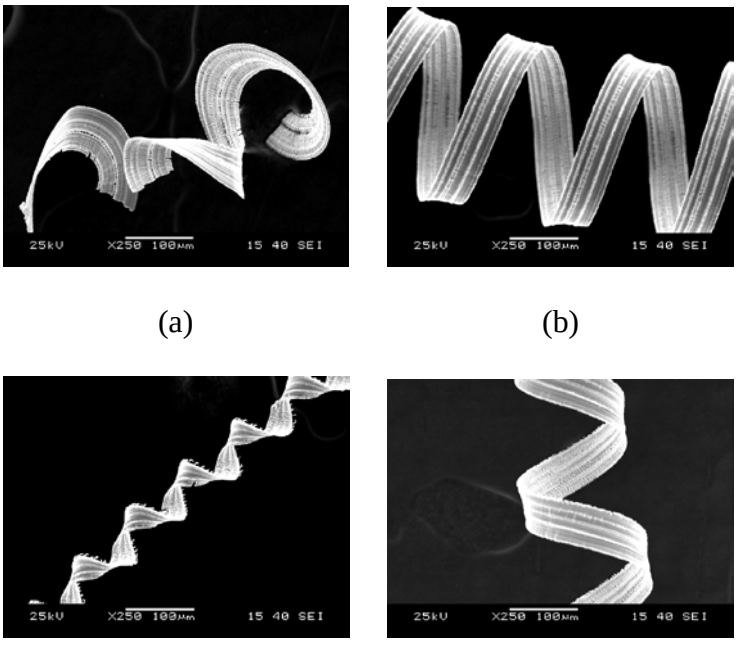

(a) (b)

(c) (d)

Figure 6.5. SEM (250×) photographs of the curled chips with four different cutting conditions in the EVC test (DOC=10 µm): (a) n_r = 45 rpm, f_r = 5 µm/rev, (b) n_r = 30 rpm, f_r = 5 µm/rev, (c) n_r = 15 rpm, f_r = 5 µm/rev, (d) n_r = 15 rpm, f_r = 7.5 µm/rev.

6.2.4 Effects of cutting parameters on surface roughness

The surface roughness has a very important role in the production of precision molds, and the fatigue and corrosion resistance of a mold can be significantly enhanced by improving the surface quality. In this experimental test, the surface profile is generated by feed marks along the feed direction due to the round tool nose, and vibration marks along the nominal cutting direction due to the elliptical vibration locus. The theoretical surface roughness caused by the feed marks is determined by the tool nose radius r_n and the feed rate f_r. As the total theoretical surface roughness of the machined surface with the EVC method is a superposition of the roughness caused by the vibration marks and the roughness caused by the feed marks, its value is determined not only by r_n and f_r, but also by the vibration parameters (a, b, ω and ϕ), the nominal cutting speed (v_c) and the tool edge radius (r_e).

Figure 6.6 shows effects of different nominal DOCs, feed rates and spindle speeds, on the average and maximum surface roughness values, R_a and R_z, respectively. In examining Figure 6.6(a), it is observed that both R_a and R_z at 6 μm nominal DOC are found to be lower than those at the higher nominal DOC of 10 μm. However, at the nominal DOCs of 4 and 2 μm, which are equal to and less than the peak-to-peak vibration amplitude, respectively, the surface roughness values are relatively larger than the nominal DOC of 6 μm. It may be because that a smaller nominal DOC leads to a smaller uncut chip thickness, which can cause more significant ploughing and rubbing actions between the round tool edge and the material. Such actions can consequently deteriorate the stable plastic deformation of material, which may eventually increase the surface roughness.

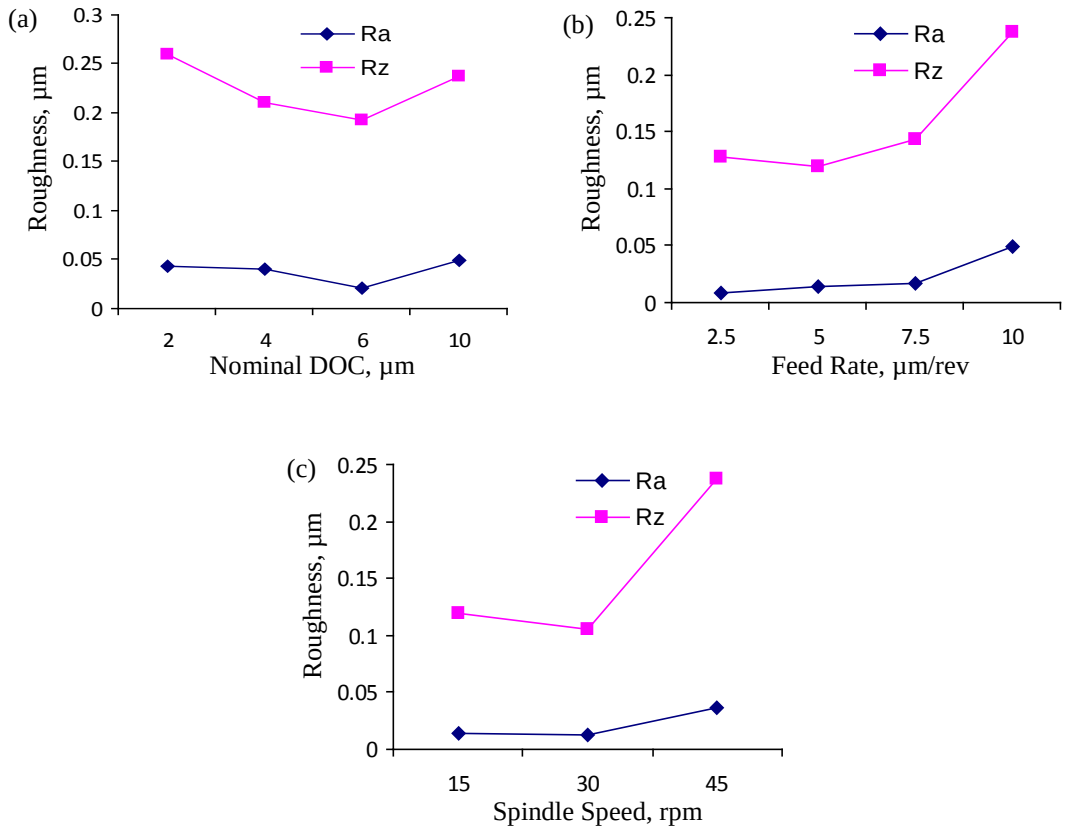

Figure 6.6. Effects of machining parameters on surface roughness values: (a) nominal DOC (n_r = 15 rpm, f_r = 10 µm/rev), (b) feed rate (n_r = 15 rpm, DOC = 10 µm), (c) spindle speed (f_r = 5 µm/rev, DOC = 10 µm).

In Figure 6.6(b), it is observed that R_a increases with the increase in feed rate, due to that a smaller feed rate leads to a smaller surface roughness caused by the feed marks. Though, Shamoto et al. have observed that the maximum surface roughness converges to a certain value as the feed rate is reduced to less than 10 µm/rev when applying the EVC method on hardened steel using SCD tools (Shamoto and Moriwaki, 1999). With ultraprecision machine tool used in the current test, the results in Figure 6.6(b) reveal that the surface finish can still be significantly improved using the PCD tools at the feed rates less than 10 µm/rev.

Figure 6.6(c) shows the surface roughness values versus three different spindle speeds. It can be observed that the surface roughness value at 45 rpm spindle speed is much higher than those values at the other two relatively lower spindle speeds. One reason for such phenomenon lie in the quick tool wear observed at a higher spindle speed. In the previous section, on the analysis of tool wear, it has been stated that the tool wear of PCD tools when machining hardened steel with the EVC method is highly affected by nominal cutting speed, and the experimental results have shown that the tool wear at 45 rpm spindle speed is much more significant than that at smaller spindle speeds (see Figure 6.4). Such faster tool wear may significantly increase the surface roughness value by inducing more ploughing mechanism in the cutting process. Another reason lies in the increased height of vibration marks with the increment of speed ratio, as shown in Figure 5.3 and Figure 5.12. Photographs of the machined surfaces obtained with these spindle speeds are also captured by the microscope, which are shown in Figure 6.7. It can be observed that with the increase in spindle speed or nominal cutting speed, the vibration marks along the nominal cutting direction are found to be more obvious.

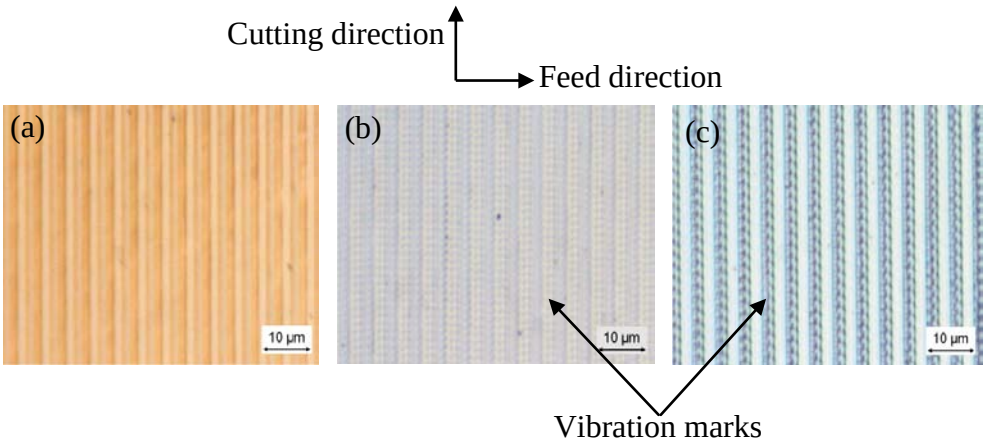

Figure 6.7. Microscope photographs (500×) of the machined surfaces at three different spindle speeds (DOC = 10 µm, f_r = 5 µm/rev): (a) n_r = 15 rpm, (b) n_r = 30 rpm, (c) n_r = 45 rpm.

Figure 6.8(a) shows AFM scan of a square area of the machined surface with 45 rpm spindle speed and Figure 6.8(b)-(c) highlight the surface profiles along the feed and the nominal cutting direction, respectively. As it can be observed from Figure 6.8(a) and (c), the vibration marks along the nominal cutting direction are obvious and hence responsible as an important part for the surface roughness. It can also be seen that the feature height in Figure 6.8(b) caused by the round nose is much larger than the cusp height in Figure 6.8(c) resulting from the vibration marks. It means that the feed marks contribute a larger part to the overall surface roughness of the machined surface compared with the vibration marks. Furthermore, small chips and protrusions are found to get adhered to the machined surface, which are difficult to clean up, as seen in Figure 6.8(a). It might be caused by the high cutting force values (see Figure 6.3(c)), the fastest tool wear (see Figure 6.4(a)) and the non-continuous chips (see Figure 6.5(a)) at the higher spindle speed (45 rpm) and accordingly the higher nominal cutting speed.

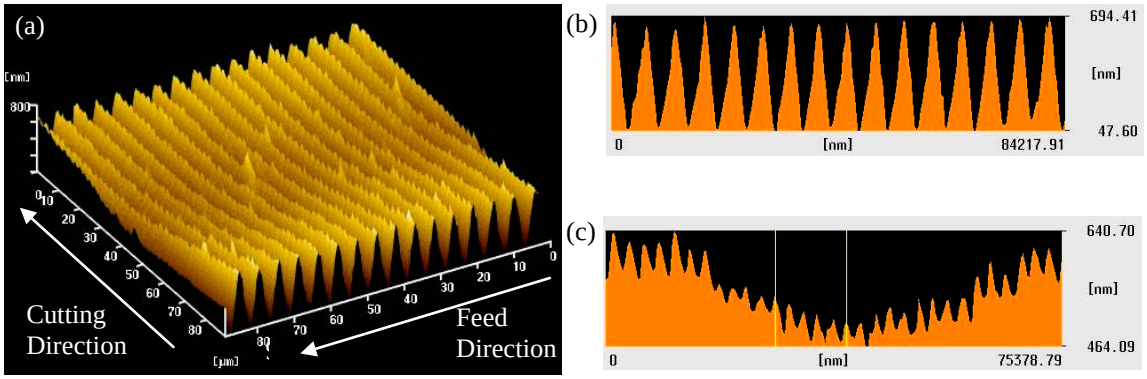

Figure 6.8. AFM scan of the machined surface in the EVC test (DOC = 10 μm, f_r = 5 μm/rev, n_r = 45 rpm): (a) overview surface profile (90 μm × 90 μm), (b) measured in the feed direction, (c) measured in the nominal cutting direction.

6.2.5 Evaluation test for obtaining mirror quality surface

Obtaining a mirror surface on hardened steel for die and using inexpensive PCD tools instead of SCD tools is the ultimate concern of this study. In order to evaluate the capability of PCD tools for this with the EVC method, an evaluation test is conducted on the entire workpiece face area (40 mm diameter, 1257 mm^2 area) with 10 μm nominal DOC, 2.5 μm/rev feed rate and 15 rpm spindle speed. Such cutting process with the combination of EVC and face turning results in a continually varying nominal cutting speed varies from a higher value at a larger radius to a smaller value towards the center of the workpiece. Figure 6.9 shows the picture of the machined workpiece surface which is reflecting the word “NUS” representing “National University of Singapore”. It can be observed that the inner circular zone (approximately 806 mm^2) can clearly reflect “NUS” and is considered as a mirror-like surface, while the outer annular surface is a little blurred and cannot give a clear reflection of “NUS”.

Figure 6.9. Machined surface on hardened stainless steel using a PCD tool with the EVC technology (DOC = 10 μm, f_r = 2.5 μm/rev, n_r = 15 rpm).

The average surface roughness of the machined surface R_a measured by the stylus profilometer is about 8 nm. The surface roughness at different radial locations is also measured by the Zygo white light interferometer, as shown in Figure 6.10. The results show that the whole machined surface can be apparently divided into two zones, the inner circular zone and the outer annular zone, in terms of surface roughness values. For the outer annular zone, where the radial distance is larger than 16 mm, the mean value of measured R_a was found to be about 30 nm. However, when the radial distance is less than 16 mm, R_a starts showing little variation with the change of radial distance, and the R_a value in the inner circular area (about 804 mm^2, obtained from $\pi \times 16^2$) is measured to be about 11 nm. The reason for this phenomenon may line in that the variation of tool-workpiece stiffness when the tool edge gets worn progressively. When the fresh tool with a very sharp tool edge is used to machine the workpiece, the contact area between tool edge and workpiece is too small to resist chatter vibration, resulting in higher surface roughness and worse surface quality.

After the tool edge is worn a little, the strength of the tool edge becomes higher, and the contact area between tool edge and workpiece is larger. Then, chatter vibration will be suppressed and better and stable surface quality can be obtained in a long period until the tool is significantly worn.

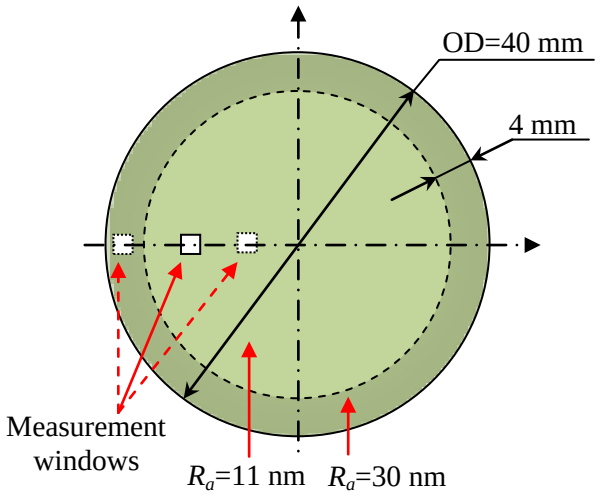

Figure 6.10. Measurement results of surface roughness for the machinined surface.

Figure 6.11 shows the photographs of the tool flank face captured by the microscope. It can be seen that the tool flank wear width is still not significant after machining such hardened stainless steel for a surface area of 1257 mm^2 with a cutting length of 533.3 m. Such machining area is considered enough for die and molding applications in the manufacturing industry. Therefore, it can be said that the PCD tool with the EVC technology is capable for long-distance machining to achieve mirror-like surface on hardened steel, if the cutting parameters are carefully controlled.

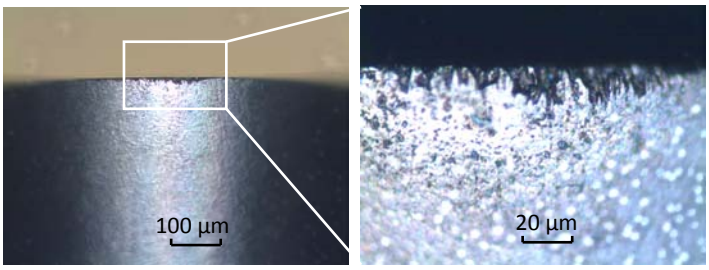

Figure 6.11. Microscope photographs (100× and 500 ×) of the worn PCD tool after the evaluation EVC test on the hardened steel (DOC = 10 µm, f_r = 2.5 µm/rev, n_r = 15 rpm).

6.3 Concluding remarks

In this chapter, an experimental study on machining a hardened stainless steel (Stavax, 49 HRC) using commercial PCD tools under the EVC method is carried out to understand the effects of conventional machining parameters on different output performance such as cutting force, tool flank wear, chip formation, and surface roughness. Then, a separate test of machining about 1257 mm^2 surface area on the hardened steel is also carried out to investigate the capability of PCD tools for obtaining mirror quality surface, as a demand of mold manufacturing industries. Based on the experimental findings, conclusions can be compiled as follows:

- The two cutting force components (tangential and thrust force) increase with the increment in nominal cutting speed. It is deemed to be caused by the decrement of shear angle and the increment in transient TOC that are both induced by the decrease in speed ratio.
- With the EVC method, the PCD tools used in cutting the hardened steel are able to achieve better surface roughness at the nominal DOC of 6 µm as compared to both the other higher and lower nominal DOCs.

- The tool wear at lower spindle speeds (30 rpm and 15 rpm), after cutting the 550 mm^2 surface area with the EVC method, is insignificant, while the tool wear at the higher spindle speed (45 rpm) is found to be much larger (14 μm tool flank width).
- The higher spindle speed (45 rpm) results in more breakable chips than the other tests with lower spindle speeds, most of which produce continuous chips with constant chip thickness. The chip width increases with the increment of nominal cutting speed.
- The experimental results show that nominal cutting speed (or spindle speed) has strong influence on the surface roughness under the EVC method. The surface roughness decreases with the decrement of feed rate and nominal cutting speed.
- The results of the separate evaluation test show that, for fabrication of die and mold parts from hardened steels, mirror-like surface can be obtained by applying the EVC method using the inexpensive PCD tools instead of the expensive SCD tools.

Chapter 7: Tool wear suppression mechanism for machining steel using diamond with the VAM method

As stated in Chapters 2 and 6, by employing VAM (i.e. CVC and EVC), diamond tools can be used to cut steel sustainably, with significantly improved tool life compared to CC (Moriwaki and Shamoto, 1991; Shamoto et al., 1999a). For the reason of the reduced tool wear in VAM, most researchers attributed it to the experimentally measured reduced cutting force, which they believe will lead to smaller heat generation and reduced temperature in the VAM process (Brehl and Dow, 2008; Zhou et al., 2003). Such explanation seems to be reasonable because an increased temperature usually leads to a higher chemical reaction rate and hence a higher wear rate of diamond tools. However, in 2005, Mitrofanov et al. (Mitrofanov et al., 2005b) found that the tool tip temperature in VAM is 15% higher than in CC by monitoring the cutting process of machining Inconel 718 using carbide tools with the infrared thermography. This experimental result is surprising and adverse to the other researchers' traditional speculation that VAM is supposed to produce smaller heat generation and lower tool/workpiece temperature. Unfortunately, researchers did not provide theoretical explanation and quantitative analysis for the observed phenomenon, and no follow-up studies have been found to further verify and explain their experimental results. Therefore, researchers are still confused about the extent of

cutting energy consumption and tool/workpiece temperature in VAM, let alone their role in slowing the tool wear. Moreover, as no theoretical and systematic explanations have been made on the tool wear suppression of diamond in VAM of steel by previous researchers, the inherent reasons are still unclear and needs in-depth studies on this issue.

In this chapter, firstly, cutting energy consumption for VAM is quantitatively modeled and calculated by investigating the transient cutting force and the corresponding tool motion position. Secondly, workpiece temperatures are measured in CC and VAM of steel by using a contacting thermocouple, and the obtained results are compared and explained carefully. Finally, experimental tests are conducted to investigate and compare the tool wear condition of PCD tools in CC and VAM of carbon steel. Based on the comparison results and previous researchers' relevant studies, two main reasons, instead of the speculated reduced temperature, are proposed and discussed for the reduced wear rate of diamond tools in VAM of steel.

7.1 Modeling of cutting energy consumption in VAM

Cutting energy is defined as the work done by the cutting tool in order to remove workpiece materials, and is mainly spent in elastic and plastic deformation of materials, and the friction on the tool rake and flank faces. Such mechanical energy will be converted irreversibly into heat, which is eventually dissipated into the ambient environments (e.g. tool, workpiece, air, etc.) and then leads to a higher tool/workpiece temperature. It can be said that, under otherwise identical conditions, the cutting energy is in direct proportion to the tool/workpiece temperature. Hence, in the following part of this section, the cutting energy consumption in VAM is modeled and calculated based on the transient cutting force for each cutting cycle.

In order to obtain the transient cutting force in VAM, a series of low-frequency orthogonal CVC and EVC (i.e. 1D and 2D VAM) tests with four different speed ratios (0.025, 0.05, 0.075 and 0.1) are conducted on 6061 aluminum alloy workpiece. The vibration loci can be generated according to Equations (2.1) and (2.9), and the procedure for generating the vibration motion can be found in Chapter 3. The transient cutting force for CC and EVC can be obtained from Chapters 3 and 4, and the orthogonal CVC tests are conducted under the same cutting and vibration conditions with the EVC tests as shown Table 3.1, except that the thrust amplitude b is set zero.

Figure 7.1 shows the maximum resultant force R_{max} against different speed ratios for the three cutting methods (CC, CVC and EVC). As found by previous researchers, it can be seen from Figure 7.1 that the maximum resultant force in VAM is smaller than that in CC, and EVC produces even smaller force compared to CVC. In both the CVC and EVC processes, the value of R_{max} will decrease with the decrement of the speed ratio R_s. Such phenomenon may be caused by the reduced value of transient thickness of cut and the increased value of transient shear angle in each cutting cycle. As an example, the recorded transient cutting force components (principal and thrust force) for the three cutting methods (CC, CVC and EVC) at the cutting speed of 0.188 mm/min (i.e. R_s=0.1) are shown in Figure 7.2(a)-(c).

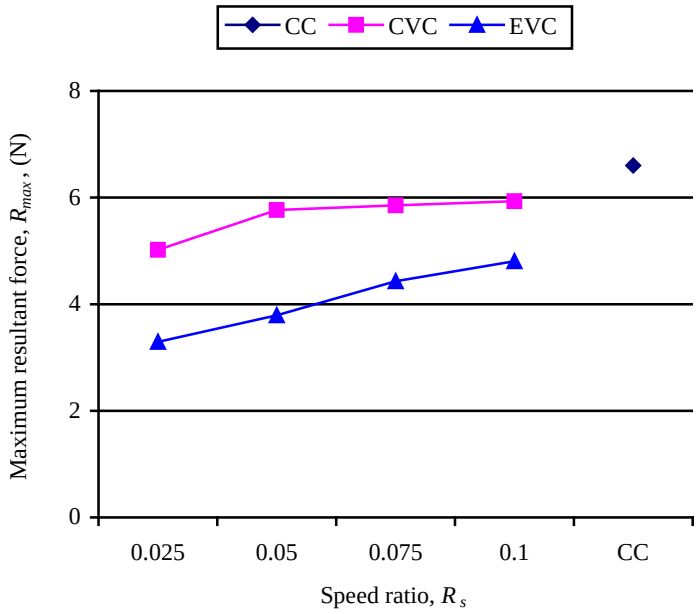

Figure 7.1. Maximum resultant cutting force in the CC and VAM processes.

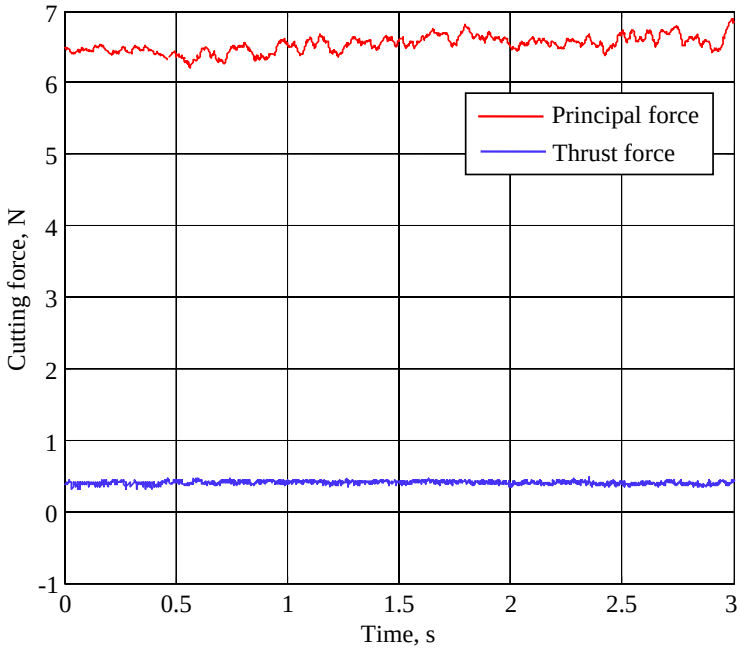

(a)

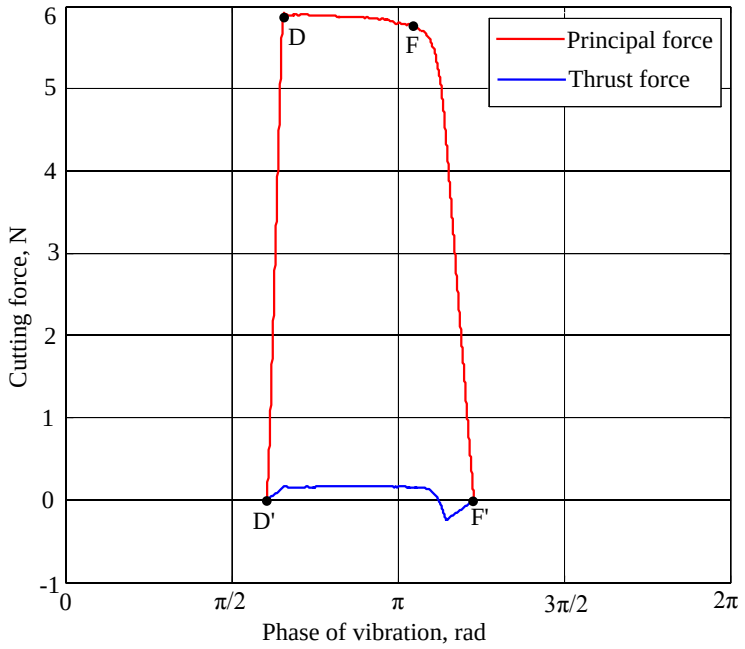

(b)

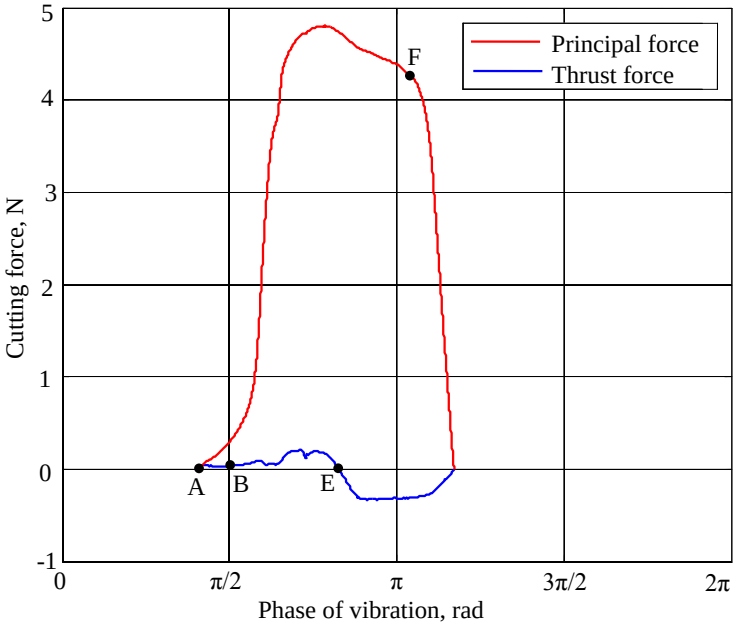

(c)

Figure 7.2. Experimental transient cutting force components in: (a) CC, (b) CVC, (c) EVC.

In the CC process (see Figure 7.2(a)), the principal force F_p is stable and can be assumed to be constant, and the thrust force does not do work due to no relative movement along the thrust direction. Hence, given a cutting distance of L_c, the total work done by the cutting tool (i.e. cutting energy consumption) can be calculated as follows:

$$W_{CC} = L_c F_p \tag{7.1}$$

Figure 7.2(b) shows the transient cutting force components in the CVC process, where the points G and H correspond with the theoretical cutting-start and cutting-end points, as shown in Figure 2.1. It can be seen that, before the tool edge arrives at point G, the tool rake face has already contacted with the workpiece material. During the elastic deformation process from the actual tool/workpiece engagement point G' to point G, material stress is progressively increased and elastic energy is accumulated. Then the workpiece material from point G to point H will be removed from the workpiece by the cutting tool through plastic deformation. After that, the material will experience an unloading and elastic recovery process, during which the material stress will be released gradually until the elastic energy is fully dissipated at the actual tool/workpiece disengagement point H'. Figure 7.3 schematically shows the CVC process considering elastic deformation and recovery in a cutting cycle.

In the CVC process, the transient principal force F_p(t) varies over time in each cutting cycle, while in the CC process, the transient thrust force F_t(t) does not do work due to no thrust directional relative movement. Hence, it is not applicable to use Equation (7.1) to calculate the cutting energy consumption in CVC. In such case, it is necessary to divide the tool motion locus into small steps, and the work done by the tool in a cutting cycle can be calculated as the sum over these small steps. Meanwhile,

as the number of cutting cycles experienced for a given cutting distance of L_c can be calculated as $L_c f / v_c$, the cutting energy consumption in CVC can be given by the following equation:

$$W_{CVC} = L_c \frac{f}{v_c} \int_0^{t_H} F_p(t)\left|x'(t)\right| dt \qquad (7.2)$$

where $\int_0^{t_H} F_p(t)\left|x'(t)\right| dt$ represents the work done by the cutting tool in a cutting cycle. The value of t_H and $x'(t)$ can be derived from Equations (2.3) and (2.7) in Chapter 2. The upper limit of the integration is set as t_H, due to the fact that, after passing point H, the tool will recede from the workpiece and stop doing positive work. In fact, in the period from point H to point H', the elastic energy accumulated in the workpiece material is dissipated gradually into the ambience, and no cutting energy is consumed by the tool.

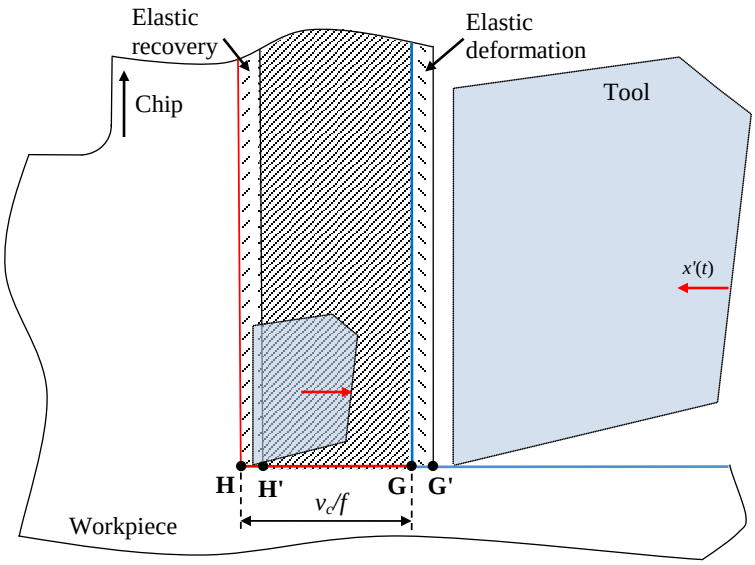

Figure 7.3. Schematic illustration of the CVC process considering elastic deformation and recovery.

Figure 7.2(c) shows the transient cutting force components in the EVC process. The points A, B, E and F correspond with the relevant points in Figure 2.2(a). Like the CVC process, in EVC, elastic deformation and recovery will also happen due to the periodical vibration along the nominal cutting direction. However, the work in EVC is not only done by the principal force, but also by the thrust force, due to the existence of relative movement along the thrust direction (see Figure 2.2(a)). Furthermore, as the transient thrust force is not reversed in direction until arriving at point E, its direction should be opposite to the thrust directional tool velocity during the interval from point B to point E, where the transient thrust force does not do positive work. Therefore, based on analyses of the motion locus and the variation of transient cutting force, the cutting energy consumption in EVC can be calculated as follows:

$$W_{EVC} = L_c \frac{f}{v_c}\left[\int_0^{t_F} F_p(t)\left|x'(t)\right|dt + \int_0^{t_B} F_t(t)\left|y'(t)\right|dt + \int_{t_E}^{2\pi} \left|F_t(t)\right|y'(t)dt\right] \qquad (7.3)$$

where $\int_0^{t_F} F_p(t)\left|x'(t)\right|dt$ is the work done by the transient principal force, and $\int_0^{t_B} F_t(t)\left|y'(t)\right|dt + \int_{t_E}^{2\pi} \left|F_t(t)\right|y'(t)dt$ represents the work done by the transient thrust force. $x'(t)$ and $y'(t)$ represent the transient tool velocities along the *x*- and *y*- axes (see Equation (2.10)), and t_B, t_E and t_F represent the time when the tool passes the points B, E and F, respectively. The values of t_B and t_F can be calculated from Equations (2.16) and (2.13), and the value of t_E can be found directly from the experimental value of transient thrust force (see Figure 7.2(c)).

Based on the obtained values of transient cutting force, the cutting energy consumption for the three cutting methods by the cutting tool can be calculated by

using Equations (7.1), (7.2) and (7.3). Figure 7.4 shows the calculated values of cutting energy against 4 different speed ratios for a cutting distance of 1m. It can be seen that the VAM methods produce a cutting energy which is not smaller than the CC method, which can be expressed as follows:

$$W_{CVC}, W_{EVC} \geq W_{CC} \tag{7.4}$$

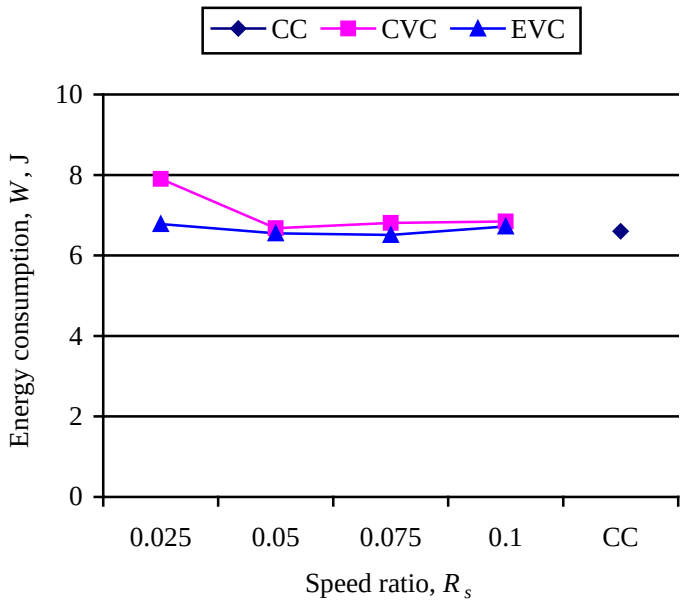

Figure 7.4. Calculated cutting energy consumption in the CC and VAM processes.

It is interesting to find that the results obtained from theoretical work are adverse to previous researchers' traditional opinion that VAM leads to reduced cutting energy and heat generation due to the reduced cutting force compared to CC (see Figure 7.1) (Brehl and Dow, 2008; Shamoto et al., 1999b; Zhou et al., 2003). It is because that the requisite accumulation of elastic energy and the additional work done by the thrust force were not considered by them, and, in fact, such two factors two factors should play an important role in calculating the energy consumption.

From Figure 7.1, it can be observed that a smaller speed ratio leads to a smaller cutting force. However, the value of cutting energy consumption for VAM varies in a different way, which should be caused by the increased number of cutting cycles (i.e. $L_c f / v_c$) for a unit of cutting length resulted from a smaller speed ratio. In that case, the material needs to experience more times of elastic deformation and hence accumulate more elastic energy during the VAM process.

According to the directly proportional relationship between cutting energy consumption and tool/workpiece temperature, it is highly possible that VAM may also produce a workpiece temperature which is not smaller than CC. Therefore, in order to verify the above theoretical proposal experimentally, the workpiece temperatures in CC and VAM are measured in the next section.

7.2 Measurement of the workpiece temperature

The workpiece temperatures in the CC, CVC and EVC processes are measured by a contacting thermocouple, which is placed close to the machined area. Figure 7.5(a) and (b) show the schematic and physical illustration of the experimental setup, where the workpiece is kept fixed on the vacuum chuck, and the cutting tool is moved by driving the Y-axis of the ultraprecision machine tool. Three fresh PCD tools are used to groove 6 times uninterruptedly on a workpiece made of carbon steel for the three cutting methods, and the nominal depth of cut for every grooving is set at 10 μm. Due to the gradually increasing groove width, the volume of removed material becomes larger and larger with the increase of groove number (see Figure 7.5(a)). The machined grooves are located 0.1 mm away from the center hole of the workpiece, where the thermocouple junction is fixed. Meanwhile, a temperature data logger is connected with the thermocouple to measure the junction temperature, which is then

recorded in the computer. In the VAM process, the vibration of tool tip is generated by several piezoelectric actuators stacked in a metal block. The vibrator vibrates at a frequency of 38.87 kHz with a phase difference of 90^{o}, and the tangential and thrust vibration amplitudes (i.e. *a* and *b*) can be set by adjusting the controller of the VAM device. Table 7.1 lists the detailed cutting and vibration conditions for measuring the workpiece temperature.

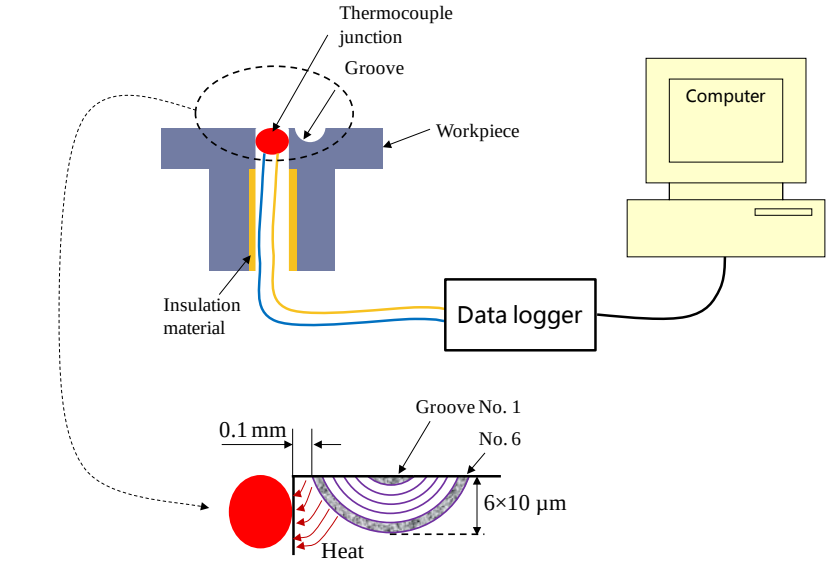

(a)

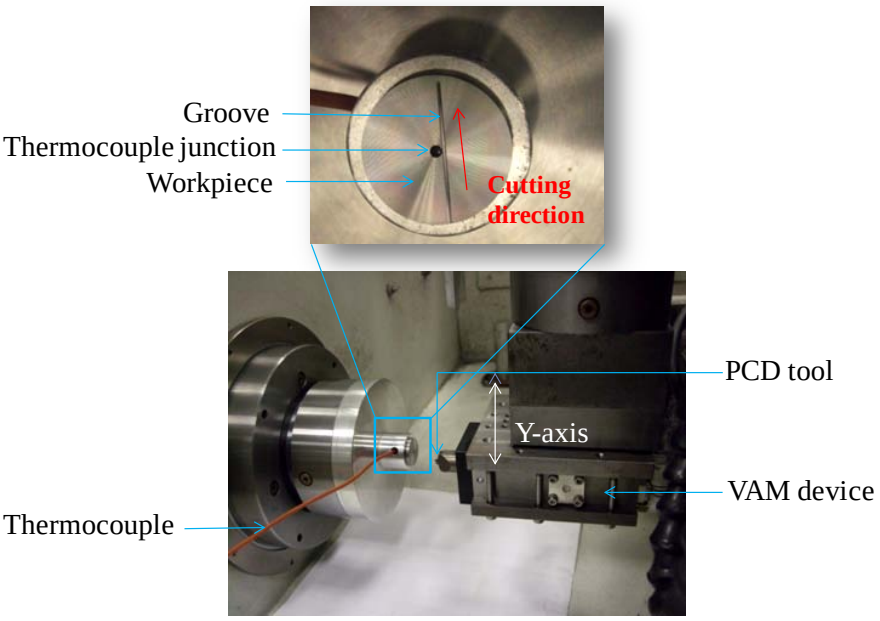

(b)

Figure 7.5. Illustration of the experimental setup for measuring the workpiece temperature: (a) schematic view, (b) physical view.

Table 7.1. Conditions for measurement of the workpiece temperature.

Workpiece material	Carbon steel (ASSAB 760)		
Tool	PCD tool (0.6 nose radius)		
Lubrication condition	Dry cutting		
Nominal depth of cut, [μm]	6×10		
Nominal cutting speed, v_c [mm/min]	450		
Vibration amplitudes, [μm]	a=0, b=0 (CC)	a=2, b=0 (CVC)	a=2, b=2 (EVC)

Figure 7.6 shows results for the temperature variation measured in the experimental tests. During the machining process, mechanical work is done by the cutting tool as the workpiece material is removed. Meanwhile, the consumed cutting energy is eventually converted into heat, which will be partially dissipated into the workpiece material and raise the workpiece temperature. The workpiece temperature will rise to a peak value once the tool passes the thermocouple junction. Then, due to the dissipation of heat into the ambient environment, the workpiece temperature will fall gradually. From Figure 7.6, it can be observed that the peak values of temperature rise for both CVC and EVC are not smaller than that for CC, as expressed in the following equation:

$$\Delta T_{CVC}, \Delta T_{EVC} \geq \Delta T_{CC} \tag{7.5}$$

Hence, it is reasonable to expect that, for the same material removal rate, more heat is transmitted from the tool/workpiece interface to the thermocouple junction, due to more consumed cutting energy in the VAM process compared to CC. Such experimental findings, together with the results obtained by Mitrofanov et al. (Mitrofanov et al., 2005b), can verify that the proposed theory in the previous section is reasonable and reliable.

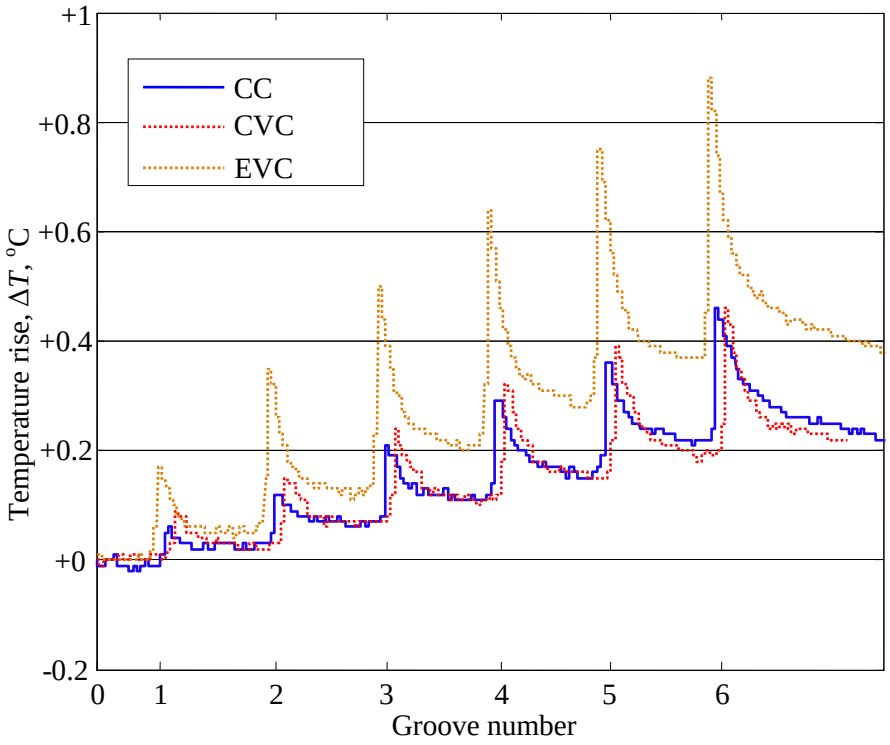

Figure 7.6. Temperature variation of the workpiece under different cutting methods.

Furthermore, from Figure 7.6, it is interesting to observe that the EVC produces much larger temperature rise compared to the CVC, which does not comply well with the theoretical analysis on cutting energy consumption (see Figure 7.4). The main reason for this phenomenon may lie in that the edge radius of the PCD tool used in grooving workpiece is significantly larger than that of the SCD tool used in obtaining the transient cutting force. Due to the micron-level edge radius of the PCD tool, when the tool edge moves from the cutting-start point A to the bottom point B (see Figure 2.2(a)), the tool edge will punch some material into the workpiece surface, and then induce a much larger transient thrust force than expected. Hence, more cutting energy will be consumed, and the workpiece temperature can be raised higher due to the increased heat generation.

In the previous two sections, the theoretical analysis and the experimental investigation have demonstrated that VAM do not produce smaller cutting energy and lower tool/workpiece temperature compared to CC. Furthermore, it has been found that the wear rate of diamond tool in machining steel is not affected as the workpiece temperature is artificially heated to 220 ^{o}C from 20 ^{o}C (Thornton and Wilks, 1979), which implies that the graphitization rate is not thermally activated in such temperature interval. Considering the extremely low cutting speed in VAM (Brehl and Dow, 2008; Zhang et al., 2011), even based on a conservative estimate (Thornton and Wilks, 1979), the flash temperature in the tool/workpiece interface should be less than 220 ^{o}C. Hence, it can be concluded that the reduced wear rate of diamond tools in machining steel using VAM should not be caused by the reduced temperature claimed by previous researchers.

7.3 Tool wear suppression mechanism in VAM

7.3.1 Experimental investigation

Before proposing reasons for the tool wear suppression mechanism in VAM, the tool wear conditions for the CC, CVC and EVC methods are experimentally investigated when machining steel using PCD tools. In the cutting tests, face turning is conducted on a circular flat surface with a diameter of 18 mm by using a fresh PCD tool, which is mounted on the VAM device, as shown Figure 7.7. The cutting tool is fed from the outer edge of the workpiece to the center, and the cutting distance is calculated to be about 102 m. Meanwhile, the wear conditions of the three PCD tools with the three cutting methods (CC, CVC and EVC) are experimentally investigated by using a microscope (*OLYMPUS STM 6*) to capture photographs of the tool flank

faces. Table 7.2 shows the detailed cutting and vibration conditions for the experimental tests.

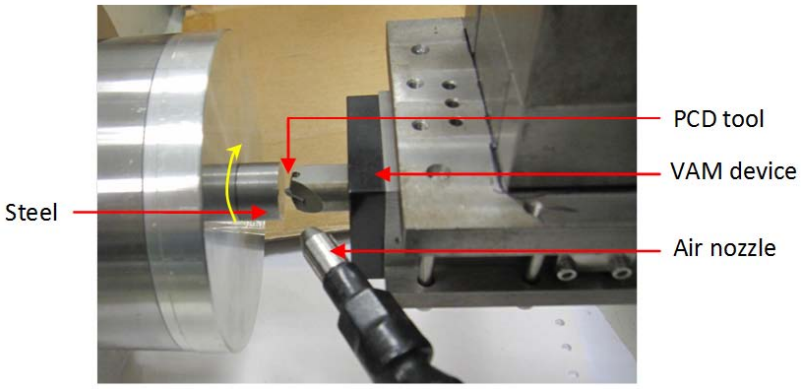

Figure 7.7. Experimental setup for machining steel using PCD tools.

Table 7.2. Conditions for machining steel using PCD tools with CC and VAM methods.

Workpiece material	Carbon steel (ASSAB 760)		
Tool	PCD tool (0.6 nose radius)		
Lubrication condition	Air cooling		
Depth of cut, [μm]	10		
Feed rate, [μm/rev]	2.5		
Rotational speed, [rpm]	20		
Nominal cutting speed, [mm/min]	$0 \sim 1.131\times10^{3}$		
Vibration amplitudes, [μm]	a=0, b=0 (CC)	a=2, b=0 (CVC)	a=2, b=2 (EVC)

Figure 7.8 shows the microscope photographs of the tool flank faces for the three PCD tools after the face turning tests. It can be observed that the VAM methods produce significantly smaller tool wear compared to the CC method. For CVC (see Figure 7.8(b)), only slight tool flank wear exists around the tool edge, while for EVC (see Figure 7.8(c)), the tool wear is hardly able to detect. Such comparison results also correspond well with previous researchers' experimental studies on tool wear in machining steel using diamond tools (Moriwaki and Shamoto, 1991; Shamoto and

Moriwaki, 1999; Zhou et al., 2003). Since it has been verified that the claimed reduced temperature does not contribute as a reason for such phenomenon, it is necessary to find other reasonable explanations for the reduced wear rate. Hence, in the following part of this section, based on previous researchers' studies and the experimental results in this study, two reasons are proposed for the reduced wear rate of diamond in VAM of steel.

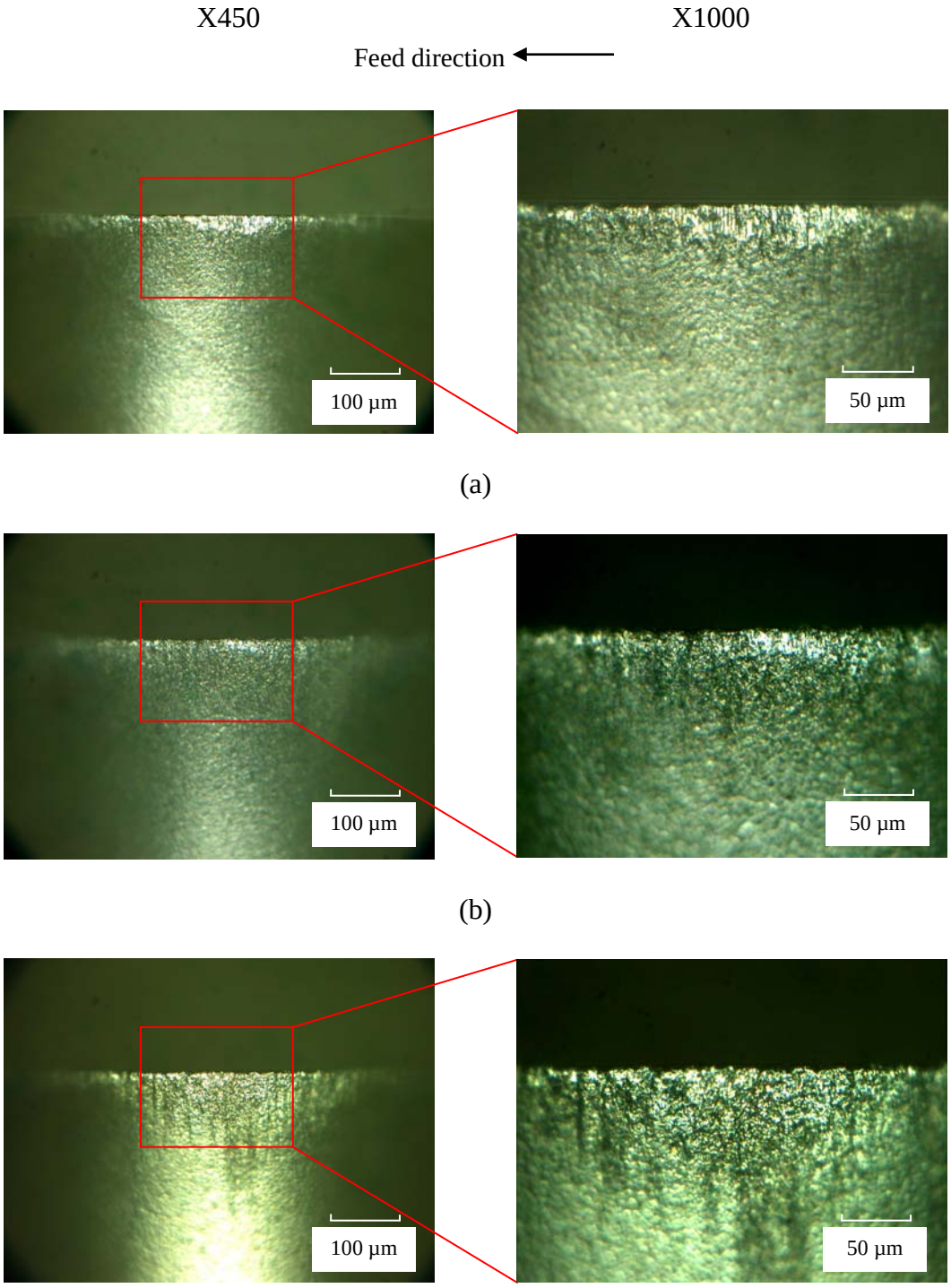

Figure 7.8. Microscope photographs of the tool flank faces in the three machining processes: (a) CC, (b) CVC, (c) EVC.

7.3.2 Contamination of the tool-workpiece interface

In order to understand the inherent reason for the high chemical wear rate of diamond in machining steel, Thornton and Wilks conducted an extensive number of experiments to investigate the effects of air pressure, cutting speed and temperature on the tool wear condition of diamond in machining steel (Thornton and Wilks, 1979). Based on the obtained experimental results, they have concluded that the quick wear of diamond tool should be caused by the freshly machined steel surfaces generated during machining, which have an enhanced chemical activity and strong chemical affinity with diamond. Table 7.3 shows the wear rates of diamond tools in machining mild steel at a cutting speed of 0.16 m/s under different atmosphere. The wear rate is defined as the ratio between the area of wear flat on tool flank face and the machined area of metal material, which is quoted in the unit of 10^{-6} (mm^2mm^{-2}). It can be seen from Table 7.3 that the wear rates in near-vacuum condition (10^{-4} atm) are significantly larger than those in Argon with normal pressure (1 atm). As Argon is inert and forms no confirmed stable compounds under most conditions, Thornton and Wilks attributed the reduced tool wear in Argon to the contamination of tool/workpiece interface by the gaseous atmosphere, which can penetrate into the interface and block off the chemical reaction and the catalyzed graphitization of diamond.

Table 7.3. Wear rates of diamond tools for turning mild steel using CC method (10^{-6} mm^2mm^{-2}) (Thornton and Wilks, 1979).

Diamond Tool	10^{-4} atm	1 atm (Argon)	1 atm (Air)
DS11R	14	2	0
DS13R	12	5	3
DS14R	8	0	0

In the VAM process, the tool rake face contacts and separates from the workpiece material regularly, and the tool/workpiece interface is exposed to the ambient atmosphere periodically, as shown in Figure 7.9(a), while in the CC process, the tool edge is pressed into contact with the freshly machined steel surface, and the wear flat on the tool flank face is almost sealed off from the surrounding atmosphere by the presence of freshly machined surface, as shown in Figure 7.9(b). Only limited gaseous atmosphere can penetrate into the tool/workpiece interface to block the chemical reaction in CC, but the intermittent cutting process in VAM will allow much more air to penetrate into the tool/workpiece interface, and strongly enhance the extent of contamination. Hence, the chemical reaction between diamond tool and the freshly machined steel surface can be blocked off more effectively compared to CC.

Compared to CVC, in EVC process, both the rake face and the flank face will separate from the workpiece periodically (see Figure 2.2). Such characteristics will allow more gaseous atmosphere to penetrate into the tool/workpiece interface, which may further enhance the degree of contamination and block off the graphitization. Moreover, the contacting time between the tool flank face and the workpiece is reduced in EVC, which can decrease the chemical reaction time and hence the tool wear rate.

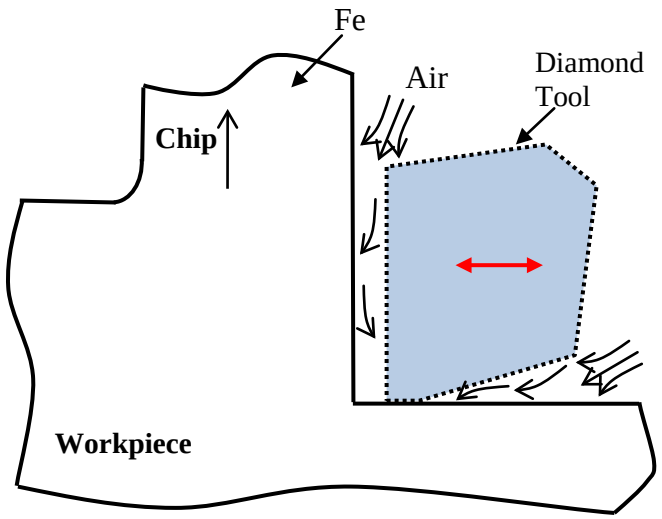

(a)

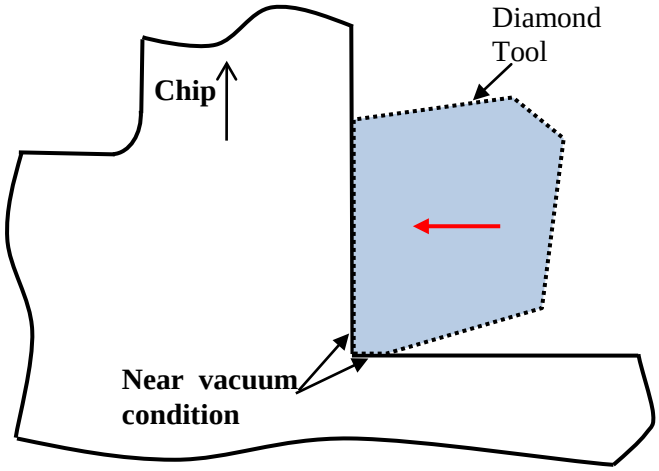

(b)

Figure 7.9. Illustration of the CC and VAM processes considering the contamination of tool/workpiece interface.

7.3.3 Generation of iron oxide on the freshly machined surface

From Table 7.3, it can also been observed that the wear rates in the air are smaller than those in Argon with the same atmospheric pressure (1 atm), which has not been explained by the researchers (Thornton and Wilks, 1979). Considering the difference

between air and Argon, this phenomenon is probably caused by the existence of active oxygen in the air, which may react with the freshly machined steel surface to form a very thin (in nanoscale) layer of iron oxide (Fe_xO) (Komanduri and Shaw, 1976). However, it is the free iron atoms that act as a metal catalyst in both graphitization and diamond nucleation. The iron oxide, which is relatively inert, does not act as a metal catalyst in the transformation between diamond and graphite. Moreover, the physical layer of iron oxide will even block the chemical reaction between free iron and carbon atoms (Qin et al., 2006), and hence suppress the graphitization.

Figure 7.10 shows a schematic view of the VAM process considering the generation of iron oxide. In CC process, as the tool/workpiece interface is not exposed to the air atmosphere periodically (see Figure 7.9(b)), the generation of iron oxide on the freshly cut surface is limited, while in VAM process, the air with oxygen will penetrate into the tool/workpiece interface and react with the freshly machined steel surface to form a thin layer of iron oxide. Due to the inertness of the iron oxide (Qin et al., 2006), the graphitization process of diamond will be blocked until the tool edge breaks the oxide layer (see Figure 7.10(b)).

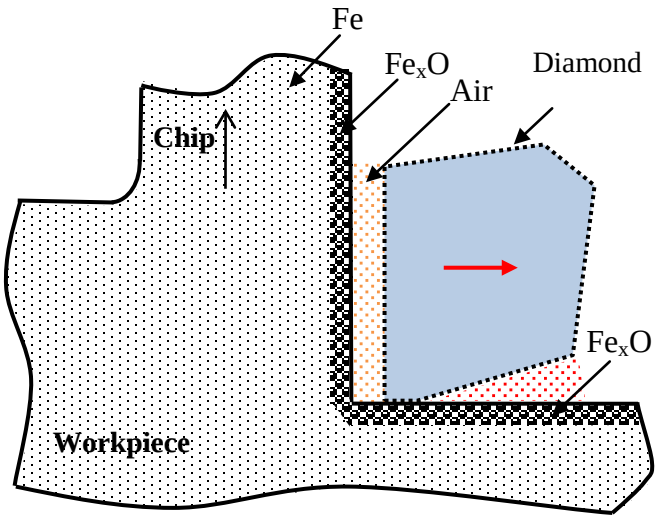

(a)

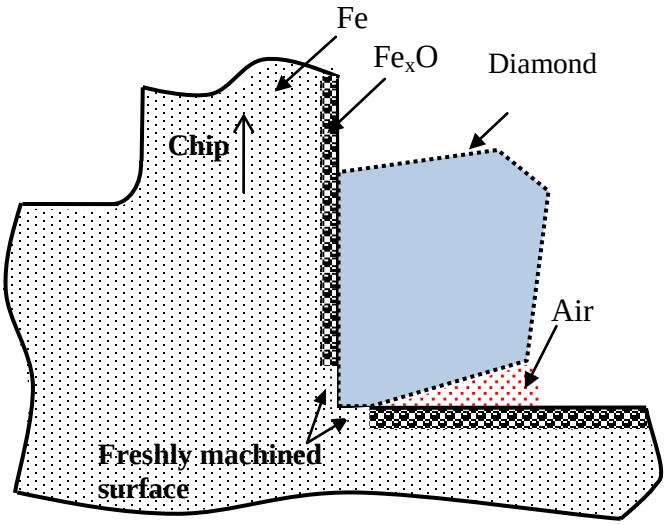

(b)

Figure 7.10. Illustration of the VAM process considering the generation of iron oxide: (a) before tool/workpiece engagement, (b) after tool/workpiece engagement.

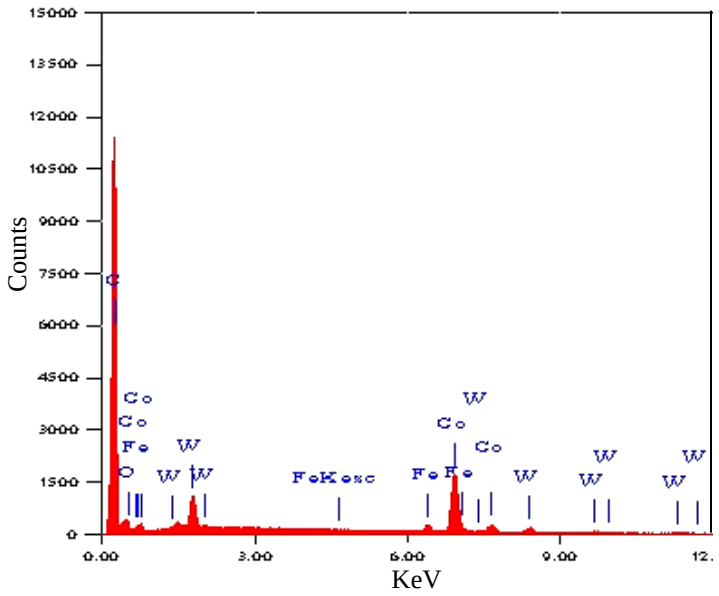

(a)

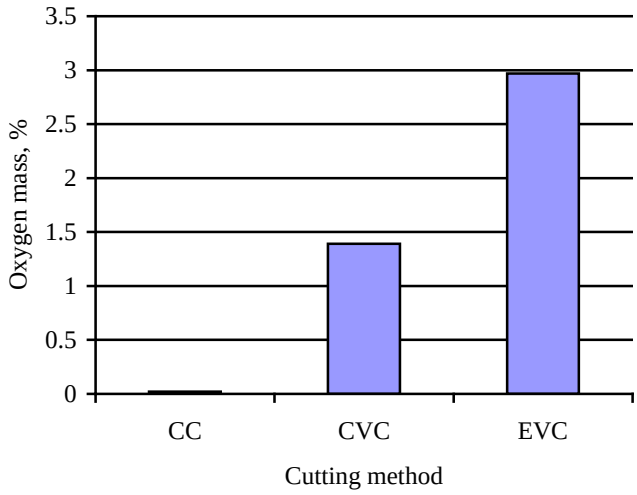

(b)

Figure 7.11. EDS analysis of the tool flank faces for the used PCD tools: (a) EDS spectrums for the tool used in EVC, (b) Comparison of oxygen mass for the three cutting methods.

Energy-dispersive X-ray spectroscopy (EDS) analysis is also conducted on the worn area on the tool flank faces of the three used PCD tools (see Figure 7.8) after machining steel, and the mass of oxygen is analyzed during the analysis. Figure 7.11 shows results of the EDS analysis for the used PCD tools. It can be seen that the mass of oxygen is almost zero for the CC process, and the VAM methods produces much higher oxygen mass. It can be speculated that the oxygen exists as a form of iron oxide, and such iron oxide on the tool flank face is accumulated gradually when the tool edge is cutting or rubbing on the workpiece material. Hence, it is reasonable to conclude that little iron oxide is generated during the CC process, and much more iron oxide is formed in the VAM process. Such observation complies well with the above proposed reason that VAM can strengthen the generation of iron oxide to block the chemical reaction between the diamond and the freshly cut steel surface.

7.4 Concluding remarks

In this chapter, in order to strengthen the understanding of tool wear mechanism of diamond in machining steel using VAM methods, both theoretical and experimental investigation has been conducted. Based on the results, conclusions can be compiled as follows:

- Based on the obtained transient cutting force in VAM, the cutting energy consumption is theoretically modeled, and the results show that VAM does not produce smaller cutting energy or heat generation compared to CC.

- It is found that the workpiece temperature in VAM is not smaller than that in the CC process, corresponding with the theoretical work about the cutting energy consumption.

- Both 1D and 2D VAM do not produce lower cutting energy or lower workpiece temperature than CC. Hence, the reduced tool wear of diamond in machining steel with VAM is not caused by the speculatively lower tool/workpiece temperature and heat generation which is claimed by the prevailing theory.

- CC produces significantly larger tool wear than VAM, and EVC produces the smallest tool wear among the three methods.

- Based on the understandings of previous researchers' studies on the chemical wear of diamond tool, two main reasons are proposed for the significantly reduced wear rate of diamond in VAM of steel: i) contamination of the tool/workpiece interface, and ii) generation of iron oxide.

Chapter 8: Main conclusions and recommendations

8.1 Main contributions

In this study, cutting force, surface generation and tool wear mechanism for the EVC method are studied experimentally and analytically. The main contributions of this study are summarized as follows:

1. **Experimental investigation and modeling of transient cutting force in the EVC process**

- In order to investigate the transient cutting force in EVC, a novel method is proposed to realize the low-frequency EVC motion by conducting G-code programming and axis motion control of an ultraprecision machine tool. The effects of three essential cutting and vibration parameters (speed ratio, tangential and thrust amplitude) are experimentally investigated and explained through analyzing the transient TOC and the friction reversal time. Mathematical evaluation of the transient TOC reveals that its value varies significantly in each EVC cycle and hence is necessary to be considered in the force model.
- An analytical force model for orthogonal EVC process is developed for in-depth understanding of the transient cutting mechanism and for accurate prediction of the transient cutting force components. Based on the variation of friction modes, each cutting cycle is divided into three consecutive zones: CC-like kinetic-friction zone, static-friction zone and reverse kinetic-friction zone. A calculation method

of the transient shear angles for the three zones is derived by investigating the transient tool/chip velocities and employing Lee and Shaffer's slip-line solution.

- The predicted transient force values based on the proposed analytical force model are found to be in good agreement with the experimental results of the orthogonal EVC tests. Hence, the proposed model can finely express the EVC mechanism and assist to predict more accurate cutting force values compared to the earlier model.

2. **Modeling the effect of tool edge radius on surface generation in the EVC process.**

- An experimental study comprising a series of grooving tests using an SCD tool is firstly carried out to clearly understand the surface generation along nominal cutting direction in the EVC process, and the experimental roughness values are compared with the theoretical ones based on previous researchers' calculation method.
- Based on the geometrical analysis for EVC surface generation process, effects of the round tool edge on material removal mechanism are investigated, and a comprehensive calculation method for determining the theoretical surface roughness considering the edge radius is developed. Simulation results based on the proposed model show that the theoretical roughness decreases with the increment of tool edge radius.
- According to experimental results of a series of grooving tests using a PCD tool with the EVC method, it is shown that the proposed model could predict much more accurate surface roughness than the prevailing model, in which the tool edge

radius is not considered. This analytical surface generation model should be helpful for the performance evaluation and further application of the EVC method.

3. **Experimental study on hardened steel using PCD tools with the EVC method.**

- An experimental study on machining hardened stainless steel (Stavax, 49 HRC) using commercial PCD tools under the ultrasonic EVC method is carried out to understand the effects of conventional machining parameters on different output parameters such as cutting force, tool flank wear, chip formation, and surface roughness.
- The experimental results also show that nominal cutting speed has strong influence on the surface roughness with the ultrasonic EVC method. It is also found that the wear of the PCD tools at lower spindle speeds is insignificant and not easy to detect, and the tool wear at the higher spindle speed is much larger.
- A separate test of machining about 1257 mm^2 surface area on the hardened steel is carried out to realize the capability of PCD tools for obtaining mirror quality surface, as a demand for die and mold manufacturing industries. The results of the separate evaluation test show that, for the fabrication of die and mold parts from hardened steels, mirror-like surface can be obtained using inexpensive PCD tools instead of highly-expensive SCD tools. This study may help industry increase the efficiency and lower the manufacturing cost with the EVC method.

4. **In-depth study on the tool wear suppression mechanism for machining steel using diamond with the VAM method.**

- Based on the obtained transient cutting force in VAM, cutting energy consumption in the VAM process is theoretically modeled, and workpiece

temperatures in the CC and VAM processes are experimentally measured by a contacting thermocouple.

- Both the theoretical and experimental comparison results lead to a fact that VAM does not produce smaller cutting energy and heat generation compared to CC. It can be concluded that the reduced tool wear of diamond in VAM of steel is not caused by the reduced heat generation and tool/workpiece temperature claimed by previous researchers.
- Finally, two main reasons are proposed for the significantly reduced wear rate of diamond in VAM of steel: i) contamination of the tool/workpiece interface, and ii) generation of iron oxide. This study could provide better understandings of diamond tool wear mechanism and hence is useful for researchers to develop other new effective methods to suppress the fast chemical wear rate.

8.2 Recommendations for future work

1. Although the proposed analytical force model has provided a quick method to calculate the transient cutting force, it still can be further improved. For example, the elastic deformation of workpiece or chip material in a vibration cutting cycle can be considered to understand the material deformation process. More important, the shear stress is assumed to be constant in the proposed model, but its actual value may change with the variation of cutting parameters. Furthermore, in order to apply the force model in predicting the cutting force in VAM of brittle materials, more factors need to be considered, such as tool edge radius and specific cutting energy.

2. The surface profile generated by elliptical-vibration assisted turning includes feed marks along the feed direction and the vibration marks along the nominal cutting direction. In this study, the proposed surface generation model only predicts the roughness along the nominal cutting direction. In order to better understand micro structures of the whole surface profile and predict its surface roughness values, a more comprehensive model needs to develop to provide more guidance and broaden the application of EVC method.

3. Researchers have already demonstrated that diamond tools with the (1 1 0) plane as the rake face perform better than the conventional diamond tools with the (1 0 0) plane as the rake face, in terms of tool wear and surface roughness. It is suggested that these specialized tools can be applied in ultrasonic vibration cutting of hard and brittle materials (such as hardened steel tungsten carbide, glass and ceramics) to further suppress the tool wear.

4. Although the two reasonable reasons are proposed for diamond tool wear suppression mechanism in VAM of steel in this study, they still need to be proven by further experimental and theoretical investigation. Moreover, based on the proposed theory, other novel methods can be proposed to effectively suppress the chemical wear of diamond tools in machining steel. For example, to prevent the chemical reaction between diamond and active iron atoms, iron oxide can be generated on the steel surface by chemical treatment before cutting with diamond tools; air cooling with more oxygen than normal air can be applied to assist to

accelerate the generation of iron oxide to further suppress iron-catalyzed diamond tool wear.

References

Ahmed, N., Mitrofanov, A.V., Babitsky, V.I., Silberschmidt, V.V., 2006. Analysis of material response to ultrasonic vibration loading in turning Inconel 718. Mater. Sci. Eng., A 424, 318-325.

Ahmed, N., Mitrofanov, A.V., Babitsky, V.I., Silberschmidt, V.V., 2007a. 3D finite element analysis of ultrasonically assisted turning. Comput. Mater. Sci. 39, 149-154.

Ahmed, N., Mitrofanov, A.V., Babitsky, V.I., Silberschmidt, V.V., 2007b. Analysis of forces in ultrasonically assisted turning. J. Sound Vib. 308, 845-854.

Ahn, J.H., Lim, H.S., Son, S.M., 1999. Improvement of micro-machining accuracy by two-dimensional vibration cutting, ASPE, pp. 150-153.

Amini, S., Shamoto, E., Suzuki, N., Nategh, M.J., 2010. FE analysis of one-directional and elliptical vibration cutting processes. Int. J. Aut. Technol. 4, 252-258.

Astashev, V.K., Babitsky, V.I., 1998. Ultrasonic cutting as a nonlinear (vibro-impact) process. Ultrason. 36, 89-96.

Babitsky, V.I., Astashev, V.K., Kalashnikov, A.N., 2004a. Autoresonant control of nonlinear mode in ultrasonic transducer for machining applications. Ultrason. 42, 29-35.

Babitsky, V.I., Mitrofanov, A.V., Silberschmidt, V.V., 2004b. Ultrasonically assisted turning of aviation materials: Simulations and experimental study. Ultrason. 42, 81-86.

Brehl, D.E., Dow, T.A., 2008. Review of vibration-assisted machining. Precis. Eng. 32, 153-172.

Brinksmeier, E., Glabe, R., 1999. Elliptical vibration cutting of steel with diamond tools, ASPE, USA, pp. 163-166.

Casstevens, J.M., 1983. Diamond turning of steel in carbon-saturated atmospheres. Precis. Eng. 5, 9-15.

Evans, C., Bryan, J.B., 1991. Cryogenic diamond turning of stainless steel. CIRP Ann. 40, 571-575.

Ikawa, N., Tanaka, T., 1971. Thermal aspects of wear of diamond grain in grinding. CIRP Ann. 19, 153-157.

Isaev, A., Anokhin, V., 1961. Ultrasonic vibration of a metal cutting tool. Vest Mashinos 41.

Komanduri, R., Shaw, M.C., 1976. On the diffusion wear of diamond in grinding pure iron. Philosophical Magazine 34, 195-204.

Kumabe, J., Fuchizawa, K., Soutome, T., Nishimoto, Y., 1989. Ultrasonic superposition vibration cutting of ceramics. Precis. Eng. 11, 71-77.

Kumbabe, J., 1979. Vibratory cutting. Jikkyou Publishing Co., tokyo.

Lee, E.H., Shaffer, B.W., 1951. The theory of plasticity applied to a problem of machining. J. Appl. Mech. 18, 405-413.

Li, X., Zhang, D., 2006. Ultrasonic elliptical vibration transducer driven by single actuator and its application in precision cutting. J. Mater. Process. Technol. 180, 91-95.

Li, X.P., Rahman, M., Liu, K., Neo, K.S., Chan, C.C., 2003. Nano-precision measurement of diamond tool edge radius for wafer fabrication. J. Mater. Process. Technol. 140, 358-362.

Liang, Y., Li, D., Bai, Q., Wang, S., Chen, M., 2006. Molecular Dynamics Simulation of Elliptical Vibration Cutting, Nano/Micro Engineered and Molecular Systems, 2006. NEMS '06. 1st IEEE International Conference on, pp. 635-638.

Liu, K., Li, X., Liang, S.Y., 2004. Nanometer-Scale Ductile Cutting of Tungsten Carbide. J. Manuf. Process. 6, 187-195.

Liu, K., Li, X.P., 2001. Ductile cutting of tungsten carbide. J. Mater. Process. Technol. 113, 348-354.

Liu, X., DeVor, R.E., Kapoor, S.G., 2007. Model-based analysis of the surface generation in microendmilling - Part I: Model development. ASME J. Manuf. Sci. Eng. 129, 453-460.

Lucca, D.A., Seo, Y.W., Komanduri, R., 1993. Effect of tool edge geometry on energy dissipation in ultraprecision machining. CIRP Ann. 42, 83-86.

Ma, C., Ma, J., Shamoto, E., Moriwaki, T., 2011. Analysis of regenerative chatter suppression with adding the ultrasonic elliptical vibration on the cutting tool. Precis. Eng. 35, 329-338.

Ma, C., Shamoto, E., Moriwaki, T., Wang, L., 2004. Study of machining accuracy in ultrasonic elliptical vibration cutting. Int. J. Mach. Tools Manuf. 44, 1305-1310.

Ma, C., Shamoto, E., Moriwaki, T., Zhang, Y., Wang, L., 2005. Suppression of burrs in turning with ultrasonic elliptical vibration cutting. Int. J. Mach. Tools Manuf. 45, 1295-1300.

Merchant, M.E., 1945a. Mechanics of the metal cutting process. I. Orthogonal cutting and a type 2 chip. J. Appl. Phys. 16, 267-275.

Merchant, M.E., 1945b. Mechanics of the metal cutting process. II. Plasticity conditions in orthogonal cutting. J. Appl. Phys. 16, 318-324.

Mitrofanov, A.V., Ahmed, N., Babitsky, V.I., Silberschmidt, V.V., 2005a. Effect of lubrication and cutting parameters on ultrasonically assisted turning of Inconel 718. J. Mater. Process. Technol. 162-163, 649-654.

Mitrofanov, A.V., Babitsky, V.I., Silberschmidt, V.V., 2004. Finite element analysis of ultrasonically assisted turning of Inconel 718. J. Mater. Process. Technol. 153-154, 233-239.

Mitrofanov, A.V., Babitsky, V.I., Silberschmidt, V.V., 2005b. Thermomechanical finite element simulations of ultrasonically assisted turning. Comput. Mater. Sci. 32, 463-471.

Moriwaki, T., Shamoto, E., 1991. Ultraprecision Diamond Turning of Stainless Steel by Applying Ultrasonic Vibration. CIRP Ann. 40, 559-562.

Moriwaki, T., Shamoto, E., 1995. Ultrasonic elliptical vibration cutting. CIRP Ann. 44, 31-34.

Moriwaki, T., Shamoto, E., Inoue, K., 1992. Ultraprecision ductile cutting of glass by applying ultrasonic vibration. CIRP Ann. 41, 141-144.

Nath, C., 2008. A study on ultrasonic vibration cutting of difficult-to-cut materials, Mechanical Department. National University of Singapore, Singapore.

Nath, C., Rahman, M., 2008. Effect of machining parameters in ultrasonic vibration cutting. Int. J. Mach. Tools Manuf. 48, 965-974.

Nath, C., Rahman, M., Andrew, S.S., 2007. A study on ultrasonic vibration cutting of low alloy steel. J. Mater. Process. Technol. 192-193, 159-165.

Nath, C., Rahman, M., Neo, K.S., 2009a. Machinability study of tungsten carbide using PCD tools under ultrasonic elliptical vibration cutting. Int. J. Mach. Tools Manuf. 49, 1089-1095.

Nath, C., Rahman, M., Neo, K.S., 2009b. A study on the effect of tool nose radius in ultrasonic elliptical vibration cutting of tungsten carbide. J. Mater. Process. Technol. 209, 5830-5836.

Nath, C., Rahman, M., Neo, K.S., 2009c. A study on ultrasonic elliptical vibration cutting of tungsten carbide. J. Mater. Process. Technol. 209, 4459-4464.

Nath, C., Rahman, M., Neo, K.S., 2011. Modeling of the effect of machining parameters on maximum thickness of cut in ultrasonic elliptical vibration cutting. ASME J. Manuf. Sci. Eng. 133, 011007.

Oxley, P.L.B., 1989. The mechanics of machining: an analytical approach to assessing machinability. E. Horwood.

Paul, E., Evans, C.J., Mangamelli, A., McGlauflin, M.L., Polvani, R.S., 1996. Chemical aspects of tool wear in single point diamond turning. Precis. Eng. 18, 4-19.

Qin, J.M., Ma, H.A., Chen, L.X., Tian, Y., Zang, C.Y., Ren, G.Z., Guan, Q.F., Jia, X., 2006. The effect of an iron powder catalyst clad with a Fe2O3 layer on the nucleation of diamonds. Diam. Relat. Mater. 15, 1369-1373.

Shamoto, E., Ma, C., Moriwaki, T., 1999a. Ultraprecision ductile cutting of glass by applying ultrasonic elliptical vibration cutting, 1st International Conference of the European Society for Precision Engineering and Nanotechnology, pp. 408-411.

Shamoto, E., Morimoto, Y., Moriwaki, T., 1999b. Elliptical vibration cutting (2nd report, study on effects of vibration conditions). Journal of JSPE 65, 411-417.

Shamoto, E., Moriwaki, T., 1993. Fundamental study on elliptical vibration cutting, American Society for Precision Engineering (ASPE) Annual Meeting, pp. 162-165.

Shamoto, E., Moriwaki, T., 1994. Study on elliptical vibration cutting. CIRP Ann. 43, 35-38.

Shamoto, E., Moriwaki, T., 1999. Ultraprecision diamond cutting of hardened steel by applying elliptical vibration cutting. CIRP Ann. 48, 441-444.

Shamoto, E., Suzuki, N., Hino, R., 2008. Analysis of 3D elliptical vibration cutting with thin shear plane model. CIRP Ann. 57, 57-60.

Shamoto, E., Suzuki, N., Moriwaki, T., Naoi, Y., 2002. Development of ultrasonic elliptical vibration controller for elliptical vibration cutting. CIRP Ann. 51, 327-330.

Shimada, S., Tanaka, H., Higuchi, M., Yamaguchi, T., Honda, S., Obata, K., 2004. Thermo-chemical wear mechanism of diamond tool in machining of ferrous metals. CIRP Ann. 53, 57-60.

Skelton, R.C., 1969. Effect of ultrasonic vibration on the turning process. Int. J. Mach. Tool Des. Res. 9, 363-374.

Suzuki, N., Haritani, M., Yang, J., Hino, R., Shamoto, E., 2007a. Elliptical vibration cutting of tungsten alloy molds for optical glass parts. CIRP Ann. 56, 127-130.

Suzuki, N., Hino, R., Shamoto, E., 2007b. Development of 3 DOF Ultrasonic Elliptical Vibration System for Elliptical Vibration Cutting, 2007 ASPE annual meeting.

Suzuki, N., Masuda, S., Haritani, M., Shamoto, E., 2004. Ultraprecision micromachining of brittle materials by applying ultrasonic elliptical vibration cutting, International Symposium on Micro-NanoMechatronics and Human Science, Nagoya, Japan, pp. 133- 138.

Suzuki, N., Nakamura, A., Shamoto, E., Harada, K., Matsuo, M., Osada, M., 2003. Ultraprecision micromachining of hardened steel by applying ultrasonic elliptical vibration cutting, International Symposium on Micromechatronics and Human Science. IEEE, Piscataway, NJ, USA, pp. 221-226.

Thornton, A.G., Wilks, J., 1978. Clean surface reactions between diamond and steel. Nature 274, 792-793.

Thornton, A.G., Wilks, J., 1979. Tool wear and solid state reactions during machining. Wear 53, 165-187.

Weber, H., Herberger, J., Pilz, R., 1984. Turning of Machinable Glass Ceramics with an Ultrasonically Vibrated Tool. CIRP Ann. 33, 85-87.

Xiao, M., Karube, S., Soutome, T., Sato, K., 2002. Analysis of chatter suppression in vibration cutting. Int. J. Mach. Tools Manuf. 42, 1677-1685.

Zhang, X., Senthil Kumar, A., Rahman, M., Nath, C., Liu, K., 2011. Experimental study on ultrasonic elliptical vibration cutting of hardened steel using PCD tools. J. Mater. Process. Technol. 211, 1701-1709.

Zhou, M., Eow, Y.T., Ngoi, B.K., Lim, E.N., 2003. Vibration-assisted precision machining of steel with PCD tools. Mater. Manuf. Process. 18, 825-834.

Zhou, M., Ngoi, B.K.A., Yusoff, M.N., Wang, X.J., 2006. Tool wear and surface finish in diamond cutting of optical glass. J. Mater. Process. Technol. 174, 29-33.

Zhou, M., Wang, X.J., Ngoi, B.K.A., Gan, J.G.K., 2002. Brittle-ductile transition in the diamond cutting of glasses with the aid of ultrasonic vibration. J. Mater. Process. Technol. 121, 243-251.

Publication list

Journal papers

[1] X. Zhang, A. Senthil Kumar, M. Rahman, C. Nath, K. Liu. Experimental study on ultrasonic elliptical vibration cutting of hardened steel using PCD tools, J. Mater. Process. Technol., 211 (2011) 1701-1709.

[2] X. Zhang, A. Senthil Kumar, M. Rahman. A study on surface generation along nominal cutting direction in elliptical vibration cutting, Adv. Mater. Res., 314-316 (2011) 1851-1856.

[3] X. Zhang, A. Senthil Kumar, M. Rahman, K. Liu. Modeling of the effect of tool edge radius on surface generation in elliptical vibration cutting, Int. J. Adv. Manuf. Technol., (2012).

[4] X. Zhang, A. Senthil Kumar, M. Rahman, C. Nath, K. Liu. An analytical force model for orthogonal elliptical vibration cutting technique, J. Manuf. Process. 14(2012) 378-387.

[5] M. Arif, X. Zhang, M. Rahman, A. Senthil Kumar. A predictive model of the critical undeformed chip thickness for ductile–brittle transition in nano-machining of brittle materials, Int. J. Mach. Tools Manuf. 64(2013) 114-122.

Conference papers

[1] X. Zhang, C. Nath, A. Senthil Kumar, M. Rahman, K. Liu. A study on ultrasonic elliptical vibration cutting of hardened steel using PCD tools, in: ASME International Manufacturing Science and Engineering Conference, Erie, PA, USA, 2010.

[2] X. Zhang, A. Senthil Kumar, M. Rahman. Modeling cutting force in elliptical vibration cutting considering the transient characteristics, in: 15th International Conference on Machine Design and Production, Pamukkale, Denizli, Turkey, 2012.

[3] X. Zhang, A. Senthil Kumar, M. Rahman. Effects of cutting and vibration conditions on the transient cutting force in elliptical vibration cutting, in the First International Conference on Intelligent Robotics, Automation and Manufacturing, Kuala Lumpur, Malaysia, 2012.